FUNCTIONAL NANOMATERIALS VIA COLLOIDAL ASSISTED FABRICATION

BY

XINDI YU

DISSERTATION

Submitted in partial fulfillment of the requirements
for the degree of Doctor of Philosophy in Materials Science and Engineering
in the Graduate College of the
University of Illinois at Urbana-Champaign, 2010

Urbana, Illinois

Doctoral Committee:

Professor Paul Braun, Chair
Professor Pierre Wiltzius
Professor John Rogers
Assistant Professor Nicholas X. Fang

ABSTRACT

Spherical colloidal nanoparticles have been popular building blocks for larger scale super structures due to their easy synthesis, unique while simple shape and relatively well understood interactions. Despite concentrated and lasting efforts in the scientific community to explore design phases of colloidal super structures and their applications, these little spheres continue to inspire the imaginations of people and creates new opportunities. In this document, a few research topics related to colloidal particles are presented. Their applications range from narrow band thermal emitters, extremely sensitive surface plasmon sensors to nanoparticles with unique geometries that might have important biological applications. Other than the scientific discoveries which will be described in details in the following chapters, the main purpose, I believe, is to fuel the inspirations of the readers. And I have the faith that the best is yet to come with these little spheres.

To my parents

ACKNOWLEDGEMENTS

A PhD program is best described as a journey. Along the way, there are many people I want to thank. So, let me start with my advisor Professor Paul Braun. To a large extent, the reason for the very existence of my journey at Illinois is because Paul's trust in me and his belief that a student should work on what he is interested in. And during the years I stayed here, he gave me lots of support and inspirations, without which finishing the whole program would not be possible.

I would also like to thank the members of the group: our team members. Thanks go especially to Dr. Yun-Ju (Alex) Lee, who guided me for my first half year here and taught me to keep being optimistic at all times; also to Dr. Huigang Zhang for his collaboration on quite a few projects which were both enjoyable and fruitful; to Dr. Jyh-Tsung Lee, Dr. Masao Miyake, Dr. Joe Geddes and Dr. Florencio García Santamaría for their insightful guidance; to Abby Juhl for showing me what one can do with courage; and finally to the rest of the members in the group for their support along the journey in various ways.

I have also learned a lot from my collaborators, in this campus, at Stanford University and at Fudan University. Their names will appear in the following chapters. And I will not forget to mention the undergrads who have worked with me, especially Felix Hotoma, John Oliverio and Josh Agar, who contributed greatly and made my research work more enjoyable.

Lots of the work would not have been possible without the huge collection of instruments and facilities available at Material Research Lab and Beckman Institute with a group of great staff members running them. Various funding sources have generously supported my study and research here, including: U.S. Department of Energy (DOE), Division of Materials Sciences, under award No. DEFG0291ER45439 and DEFG02-07ER46471, through the Frederick Seitz Materials Research Laboratory at the University of Illinois at Urbana-Champaign (UIUC), the U.S. Army Research laboratory and the U.S. Army Research Office under contract/grant number DAAD19-03-1-0227 and the Air Force Office of Scientific Research MURI FA9550-08-1-0407.

Of course there are my friends, local and far away, who made my life in this small town a lot more colorful and given me tremendous amount of support at crucial moments.

Finally, I would like to thank my parents, who have always respected my choices and consistently motivate me to challenge myself. Without them, my life could have been completely different.

TABLE OF CONTENTS

Chapter 1 Introduction ……………………………………………………………………1

- 1.1 Opal……………………………………………………………………………1
- 1.2 Synthesis of Opal Films ……………………………………………………1
- 1.3 Three Dimensional Fabrication with Opal Template …………………………4
- 1.4 Two Dimensional Fabrication with Opal Template …………………………5
- 1.5 Surface Plasmon ……………………………………………………………6
- 1.6 Figures …………………………………………………………………………7
- 1.7 Reference ……………………………………………………………………15

Chapter 2 Variable Porosity Metallic Inverse Opals for Narrow Band Thermal Emission Applications ……………………………………………………………………17

- 2.1 Introduction …………………………………………………………………17
- 2.2 Nickel Inverse Opal Preparation ……………………………………………18
  - 2.2.1 Conductive Substrate Preparation ………………………………………18
  - 2.2.2 Colloidal Crystal Growth on Conductive Substrate ………………………18
  - 2.2.3 Electrodeposition through Template ……………………………………19
- 2.3 Optical Property of Nickel Inverse Opal as Prepared …………………………20
- 2.4 Tuning Filling Fraction of Nickel by Electropolishing ………………………20
- 2.5 Evolution of Optical Properties as Metal Filling Fraction Changes ……………21
- 2.6 Thermal Emission Property of Nickel Inverse Opal …………………………22
- 2.7 Thermal Stability of Nickel Inverse Opal ……………………………………23
- 2.8 Conclusion …………………………………………………………………24
- 2.9 Experimental …………………………………………………………………25
- 2.10 Figures ………………………………………………………………………26
- 2.11 Reference ……………………………………………………………………33

Chapter 3 Other Structural Designs for Narrow Band Thermal Emission Systems 35

3.1 Introduction 35

3.2 Spherical Cavities with Cylindrical Interconnections (3D system).........................36

3.2.1 Structural Design 36

3.2.2 Fabrication..36

3.2.3 Structural Parameters 37

3.3 Square Array of Inverse Pyramids (2D System)..37

3.3.1 Structural Design 37

3.3.2 Fabrication..38

3.3.3 Optical Property...38

3.4 Monolayer of Spherical Cavities 40

3.4.1 Structural Design 40

3.4.2 Fabrication..40

3.4.3 Optical Property...41

3.5 Conclusion 43

3.6 Figures 43

3.7 Reference 52

Chapter 4 High Quality Factor Metallodielectric Hybrid Plasmonic-Photonic Crystals 53

4.1 Introduction 53

4.2 Sample Fabrication 54

4.3 Optical Property 54

4.4 Propagation Length of Resonance Modes Extrapolated From Q Factor 55

4.5 Optical Study with Computer Simulation 56

4.6 Detailed Analysis of Optical Spectrum 58

4.7 Optical Response vs. Structure Evolution 59

4.8 Optical Sensitivity of the Sensor 60
    4.8.1 Traditional Figure of Merit (FOM) 60
    4.8.2 Improved Figure of Merit 61
    4.8.3 Detection Limit of the Sensor 62
4.9 Sensing Application 63
4.10 Conclusion 64
4.11 Experimental 65
4.12 Tables 67
4.13 Figures 70
4.14 Reference 77
Chapter 5 Template Assisted Three-Dimensional Nanolithography via Geometrically Irreversible Processing 79
5.1 Introduction 79
5.2 Concept 80
5.3 Ring Particle Fabrication 80
5.4 Geometry of the Ring Particles 81
5.5 Optics of Metallodielectric Photonic Crystal 82
5.6 Conclusion 84
5.7 Experimental 84
    5.7.1 Colloidal Film Formation 84
    5.7.2 Tungsten Ring Particle Synthesis 85
    5.7.3 Alumina Ring Particle Synthesis 85
5.8 Tables 86
5.9 Figures 86
5.10 Reference 96

Chapter 6 Special Shaped Nanoparticles for Biological Applications ……..……….……….98

6.1 Introduction ………………………………………………………..……..…………..98

6.2 Metallic Nanoparticle with High Local Mean Curvature …………..……….………….100

6.3 Gold Nanoparticles with Negative Gaussian Curvature ………………………………...102

6.4 Ring Shaped Particles ………………………………………………………….………104

6.5 Conclusion ……………………………………………………………………..………106

6.6 Figures ……………………………………...………………………….………………107

6.7 Reference …………….………………………………………………..………………114

Chapter 7 Conclusion and Future Work ……..……………………………………………..…115

7.1 Patterned 3D Metallic Porous Structure ……………….………………………………115

7.2 Ring Particle Based Structures ……………………………………………..…………..117

7.3 Ring Particle and Spherical Particle Co-Assembly ……….……………………..……..118

7.4 Figures ……………………………………………………………………………………120

7.5 Reference ……………..…………………………………….……………………………123

Author's Biography …………………………………………………………….……………...124

CHAPTER 1
INTRODUCTION

1.1 Opal

Opals, at least in their highly crystalline form, have been recognized as precious gem stones for centuries (Fig. 1.1). Australia, being the largest producer of natural opal, names it their national gem stone.

The iridescent color of the gemstone has attracted many attempts to explain its origin and lead to various kinds of misbelieves [1]. Advances in physics and instrumentation in the 20th century finally provided the scientific explanation to the long lasting mystery: all colors come from coherent scattering of light by silica particles 100~400 nm in diameter arranged in a close packed crystalline form (Fig. 1.2) [2]. Materials like those with structural periodicity on the order of optical wavelength were later given the name of “photonic crystals” or “photonic band gap materials” and their optical properties can be explained by band structure theories that were developed first in solid state physics [3, 4] (Fig 1.3).

1.2 Synthesis of Opal Films

Knowing the secret of natural opals, synthetic opals have been fabricated both for scientific and commercial purposes. In scientific community, most of the attention has been drawn to make thin opal films with high crystallinity. Attempts such as slow sedimentation [5], evaporation deposition [6] or dip coating [7], spin coating [8] and even crystallization under microgravity [9] have all been tried with some approaches achieving great success, and others not so much. The building blocks: spherical colloidal particles, are not limited to silica spheres, and are extended to polymer colloids such as polystyrene (PS) [10], Poly(methyl methacrylate) (PMMA) [11] and even to metallic nanoparticles [12].

The two most promising assembly approaches are evaporation deposition/dip coating and spin coating (Fig. 1.4). In the former case, colloids are first well dispersed in a solution, which wets a near vertically positioned substrate. A meniscus forms at the liquid/substrate/air interface. As the substrate moves relative to the liquid surface, no matter whether the liquids surface drops because of the evaporation of the solvent or the mechanical motion pulls the substrate away from liquid, meniscus moves down the substrate. During the process, evaporation drives particles into the meniscus and deposits them on the substrate. Capillary force plays the biggest role here and forces the particles into a close packed form with their close packed plane parallel to the crystal air interface. Face centered cubic (FCC), hexagonal close packed (HCP) structures and their mixture (random close packed) all appear during the process [13]. However FCC tends to be the preferred structure [14].

Spin coating is a process that colloids are first stabilized in a solvent at a relative high concentration (>30%) [8]. And after applying the solution on a substrate, the substrate is spinning at high speed of a few thousand RPM [8]. During the process, solution moves away from the spin center due to centrifugal force and the friction among the colloids assists the alignment of these particles. At the same time, solvent quickly evaporates and the mobility of colloidal particles drops dramatically as their filling fraction increases. Eventually they are locked into the place. There are issues, however, with these synthetic opal films: they are usually full of cracks (Fig. 1.5), and have realatively limited long-range order. Crack formation is in particular a problem for polymer based colloidal systems. The reason has to do with the drying process they go through during the final stage. For polymer particles, in order to be stable in aqueous solution, their surface layer contains hydrophilic polymeric segments. In wet state, these charged segments are in a good solvent environment and form a fluffy layer. However, when they dry, they collapse in to a dense shell. The space left behind needs to be compensated by the displacement of spheres. And the positions of all the colloids have been locked in space in millimeter to centimeter scale. As a result, colloids displace to form domains of well packed crystal and leave cracks between these domains. In the case of silica particles, typical Stöber synthesis gives porous silica particles with porosity on the order of 20% [15, 16]. During the drying process, the pores collapse under capillary force, making the particles smaller. And the same displacement explanation applies here, too. To remove these cracks, in the case of silica particles, they are precalcinated at elevated temperature to remove all the pores. The result are opal films extending over 100 µm without cracks even after post assembly heat treatment (Fig 1.6) [16].

What if one needs a crack free opal film over a silicon wafer size? One possible solution is to get rid of the drying process all together. The idea is to stabilize colloids in a monomer solution with photoinitiator added. After spin coating, the monomer, with high boiling point, is not completely evaporated. Then, a strong UV radiation polymerizes the monomer and locks the particles in place. The polymer can then be removed by dry etching or simply burning in air [17]. (Fig 1.7) As in everything else, this approach also has its issues. First of all, the crystals formed that way are not really close packed. Particles are not in contact in any horizontal planes. In other words, these crystals have less symmetry than the ones formed by evaporation deposition. Secondly, because the monomer is not evaporated, the motion of the colloidal crystal never really freezes. As a result, after spin coating stops, colloidal particles start to remove away from their original positions. The polymerizing photo chemistry needs to be extremely fast while stable during the pre-exposure sample preparation. Keep in mind that diffusion distance is proportional to the square root of t. The first a few seconds means a lot. As a result, there is always some small displacement of these particles. In other words, the crystal is not perfectly ordered (Fig. 1.8).

1.3 Three Dimensional Fabrication with Opal Template

Ironically, the “fascinating in looking” opal film “as is” has little use for optics, because it does not have a complete photonic band gap (cPBG) [18]. However, the inverse structure, the so called “inverse opal” does possess a cPBG when there exists a refractive index contrast greater than ~3 [19].

There are multiple approaches to make an inverse opal with a synthetic opal (or colloidal crystal) as a template. Chemical vapor deposition (CVD)/atomic layer deposition (ALD), nanoparticles infilling, sol-gel infilling and electrodeposition are the most popular ones. CVD/ALD approach has been enormously successful in filling colloidal crystal with dielectric materials, such as silicon [4, 20], germanium [21], zinc oxide [22], titania [23] and even diamond [24]. However, the material does not really fill the whole inverse space of an opal due to their conformal growth pattern and the geometry of the inverse opal. The result is a less attractive photonic property [25].

Nanoparticle infilling is versatile. Any kind of particles, as long as they are stable in the solution that is compatible with the colloidal template, can fill the space of inverse opal [26, 27]. However, because the resulting structure is made of particle aggregates, the average refractive index is also lower than the bulk form [28].

Sol-gel infilling can be applied to both dielectric materials [29] and metals [30]. However, sol-gel methods usually need to deal with material shrinkage during drying, reaction and heat treatment. As a result, multiple coating steps are usually required and crack formation is common [31].

Electrodeposition is a unique approach with its virtues. First, material fills all the interstitial space and doesn’t leave any pores. Secondly, because electrodeposition starts from the substrate, the thickness of the inverse opal can be controlled by plating charge, which is independent from the thickness of colloidal template to start with. Thirdly, it is very easy to form layered composite inverse opal or embed a layer of functional defect into the inverse opal by simply switch to a different plating solution. However the problem is that electroplating only works with materials that are electrically conductive. As a result, this approach has been limited to metals [32], semiconductors [33] and conductive polymers [34] (Fig. 1.9).

1.4 Two Dimensional Fabrication with Opal Template

A consistent task for nanofabrication is to generate patterns on substrates. That pattern can then be translated into functional structures such as microelectronic circuitries. Large area nanopatterning has been heavily relying on photolithography. And it turns out that colloidal crystal monolayer or thin multilayer can also be used to generate 2D patterns on a substrate over a large scale.

A crystalline colloidal monolayer is basically a layer of spheres arranged in a triangular pattern. Looking from above, part of the substrate is visible through the interstitials in the shape of sharp tipped triangles. Using the colloidal monolayer as the mask, directional deposition or etching methods lead to transferring of the triangular pattern onto the substrate with feature area roughly 5% that of the colloidal particles (Fig. 1.10) [35]. And at different sample tilting angle, the triangular interstitials project onto the substrate as different shapes. As a result, multiple patterning with good registration can be achieved (Fig 1.11) [36].

For colloidal bi-layer, the interstitials of the first layer partially overlap with those of the second layer. Using the combined interstitial as the template, patterns with different shapes and spatial arrangements can be fabricated (Fig. 1.12) [35]. Combining colloidal deposition techniques and directional deposition and etching, new surface patterns and colloidal particles have been fabricated (Fig. 1.13) [37].

The most popular application for patterns generated that way is for plasmonics, where metallic nanostructures support local surface plasmon resonances [35, 38]. Taking advantage of the giant field enhancement of these structures, scientists have been able to able to detect and analyze very small quantities of molecules [39].

1.5 Surface Plasmon

Surface plasmon (SP), also called surface plasmon polariton or surface plasmon resonance, is a unique mode of coordinated oscillation between electromagnetic field and free electrons [40], which is bounded at metal/dielectric interface [41]. The most well known examples are the reddish color of gold colloidal particles, which is caused by strong absorption of green light due to localized surface plasmon resonance (Fig 1.14) [42].

The simplest form of SP is one that is confined to the near vicinity of a flat metal/dielectric interface, which can propagate for hundreds of micrometers or even millimeters [41]. However, because of the involvement of free electrons, SP modes have higher momentum than pure electromagnetic (EM) wave of the same frequency [40]. As a result, coupling of EM wave to SP requires mechanisms that involve momentum compensation, which include scattering [43], diffraction [44] and frustrated total internal reflection [45] (Fig. 1.15). For any specific frequency below a certain limit [40], the momentum of SP mode is highly dependent on the dielectric constant of the dielectric environment. As a result, SP has been a very powerful tool for surface based sensing [46].

1.6 Figures

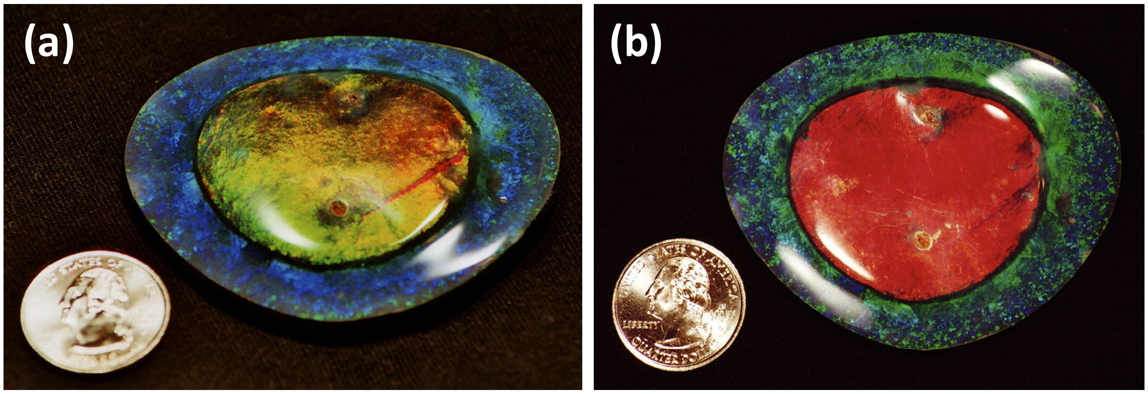

Figure 1.1 A famous gemstone opal named "flame queen" viewed from different angles. Images adopted from Wikipedia.com.

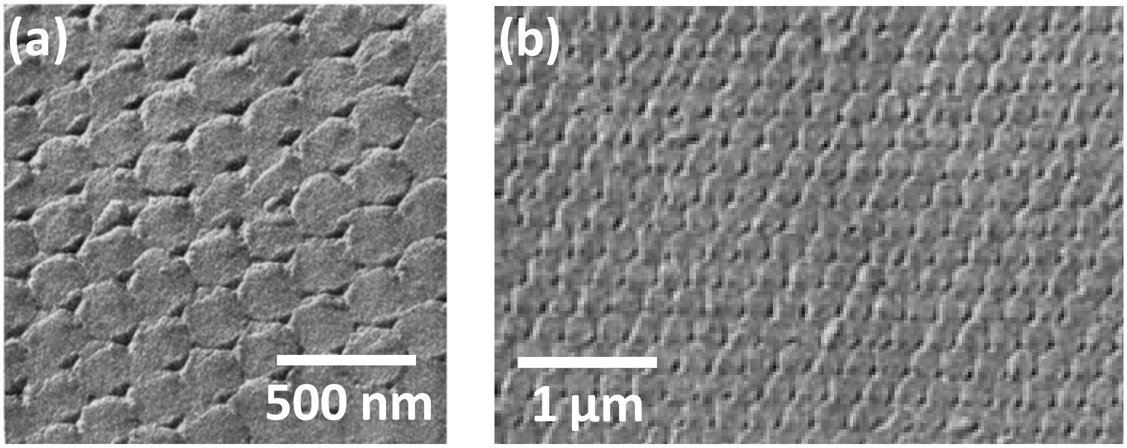

Figure 1.2 SEM images of natural precious opal, adopted from reference 2.

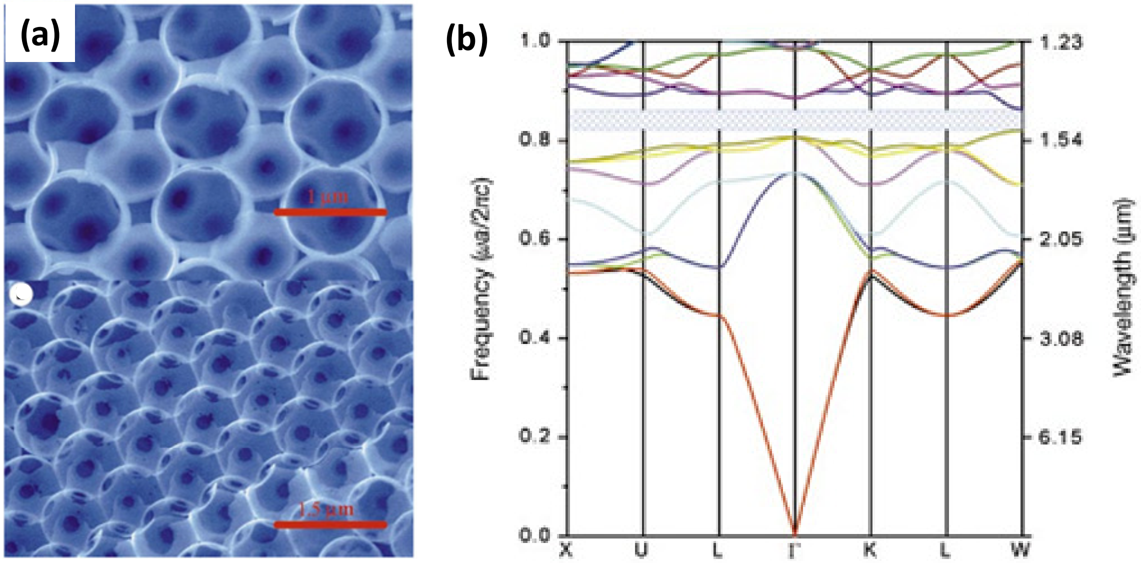

Figure 1.3 (a) Cross-section SEM images of silicon inverse opal and (b) its opal band structure showing a complete band gap.

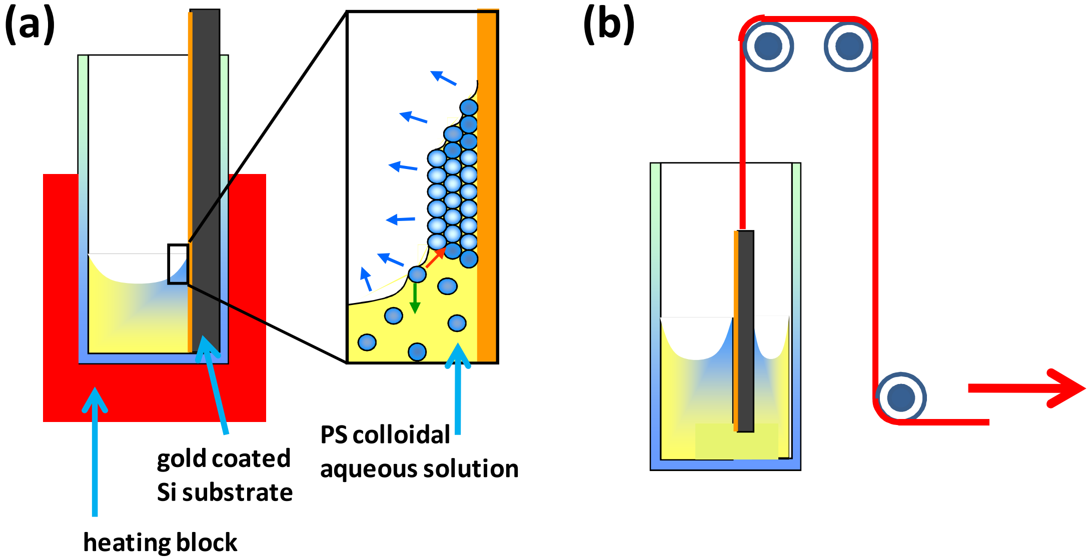

Figure 1.4 Schematics for (a) evaporation deposition and (b) dip coating.

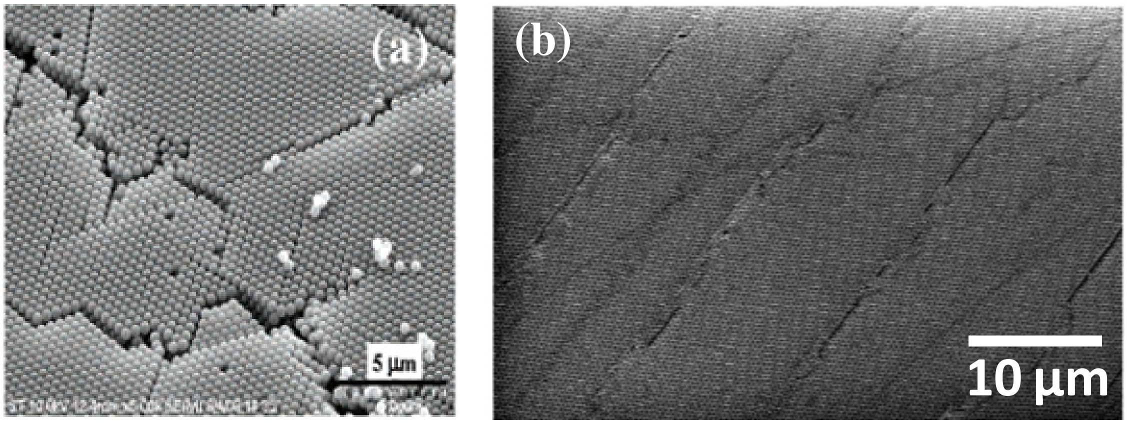

Figure 1.5 Crack formation on evaporation deposition/dip coated synthetic opal. Images taken from reference [47](a) for polystyrene opal and [6] (b) for silica opal.

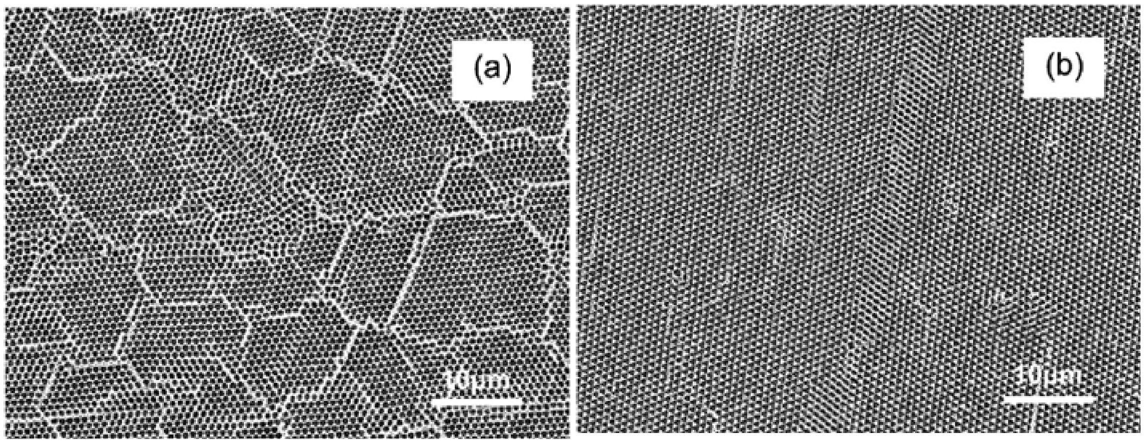

Figure 1.6 Silicon replica of silica opal made from uncalcinated (a) and calcinated (b) silica particles. Figure adopted from reference [16].

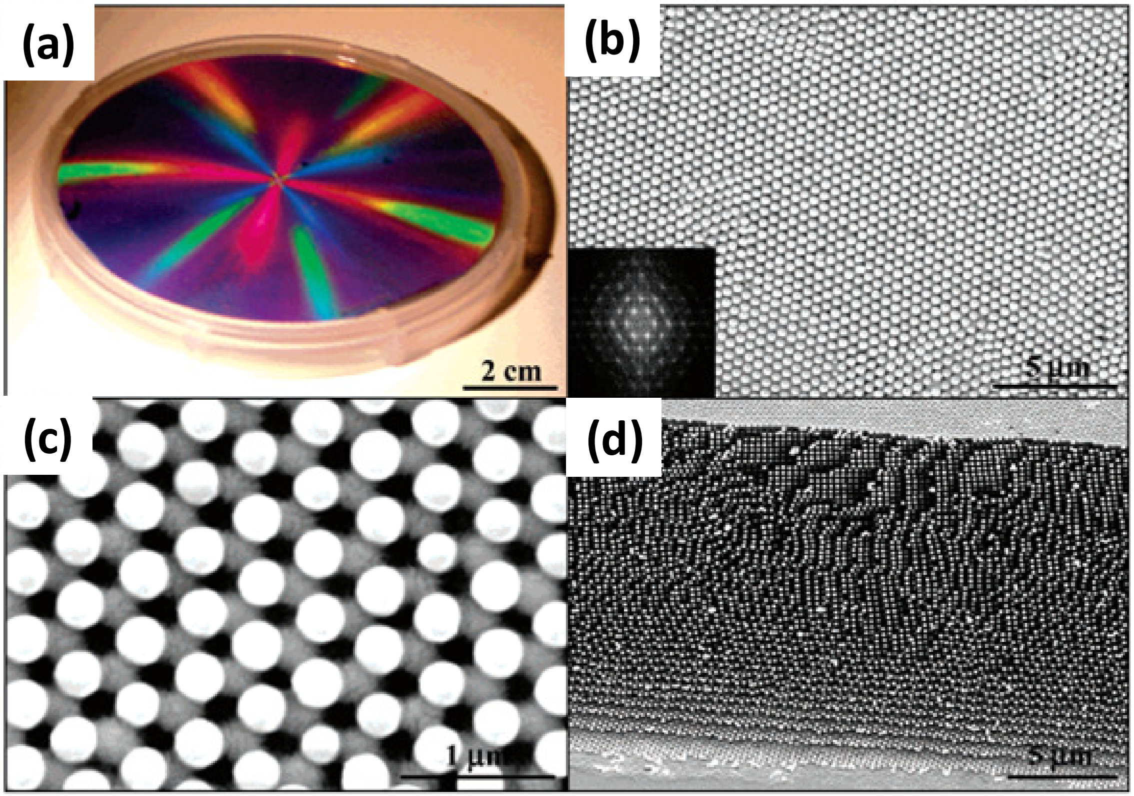

Figure 1.7 Colloidal crystal film formed by spin coating and polymerization. (a) optical image of opal film formed on a 4 inch wafer. (b) Top view SEM image of the formed opal film, showing fairly good crystallinity. (c) Zoom in SEM image showing a non close packed crystalline structure. (d) Cross-section SEM of colloidal crystal film. Images adopted from reference [17].

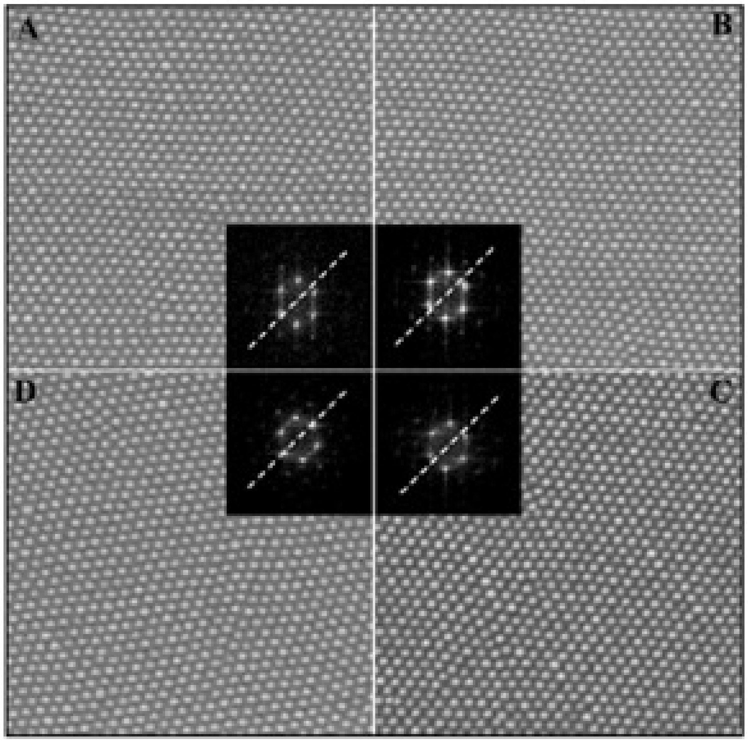

Figure 1.8 SEM image of colloidal crystal formed by spin coating and polymerization. Four images are taken at different location on the wafer. Colloidal particles deviate from their lattice spot and form wiggling lines. Images adopted from reference [17].

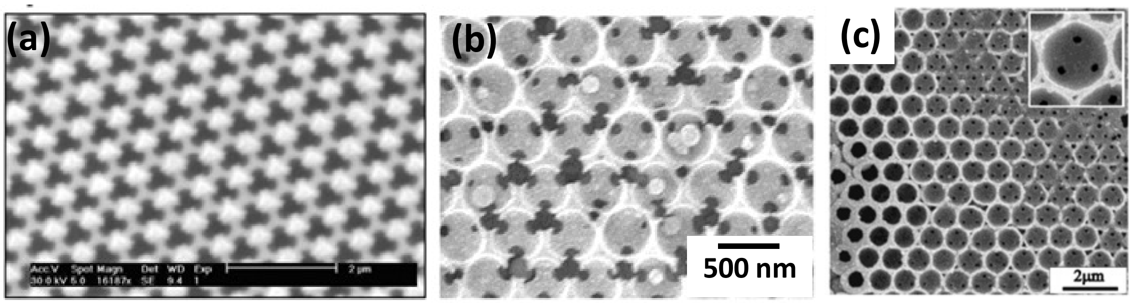

Figure 1.9 SEM images of electrodeposited inverse opal made of (a) platinum [32], (b) GaAs [33] and (c) poly(pyrrole) [34].

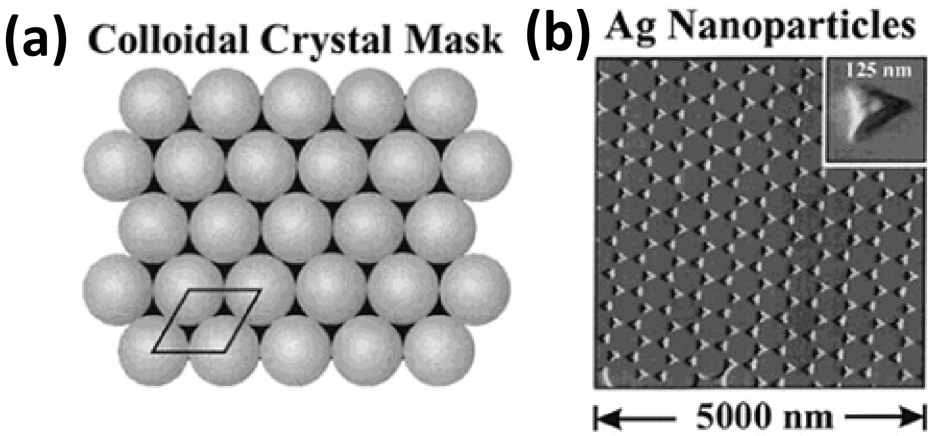

Figure 1.10 Colloidal monolayer mask and silver nanoparticle array formed by directionally depositing silver through the mask. Figures adopted from reference [35].

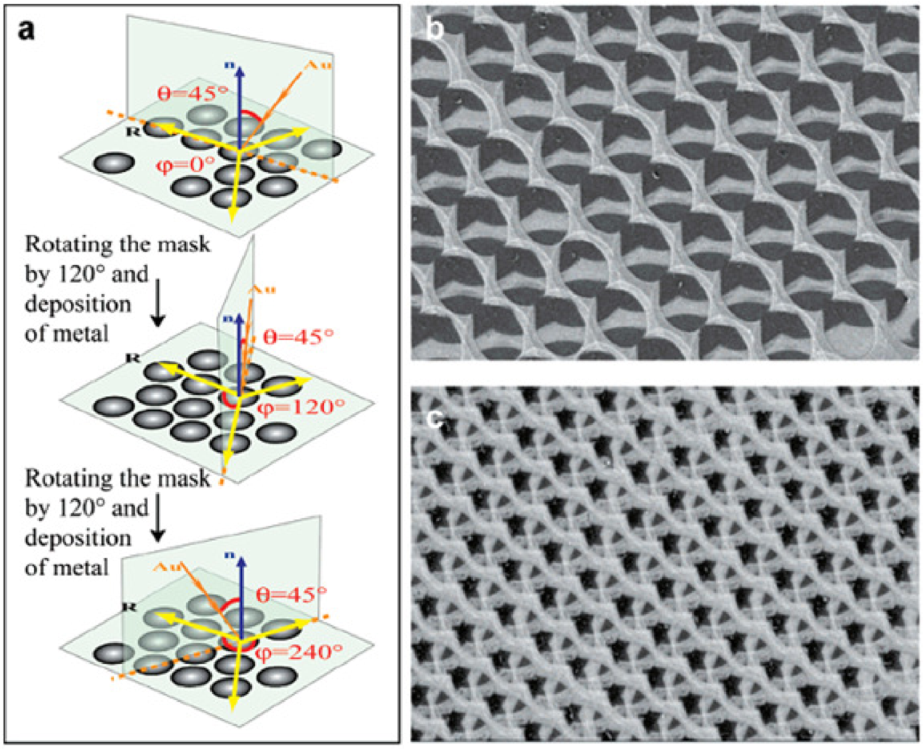

Figure 1.11 Advanced colloidal lithography by sequential deposition at various angles. The deposited patterns achieve good registration and uniformity. Image is adopted from reference [36].

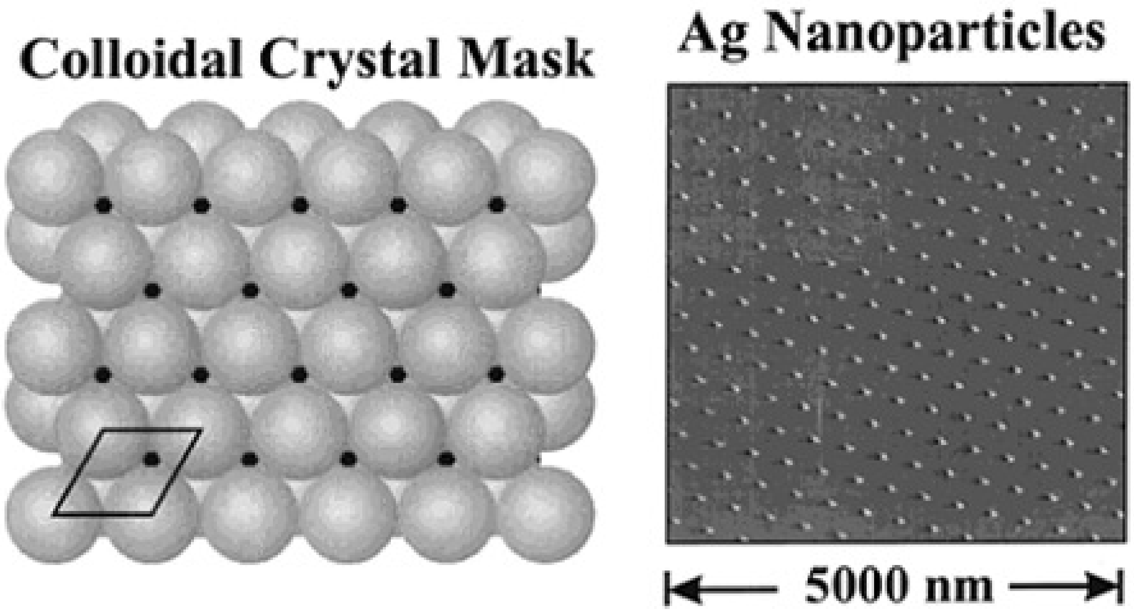

Figure 1.12 Colloidal lithography using colloidal double layer as the mask. Images adopted from reference [35].

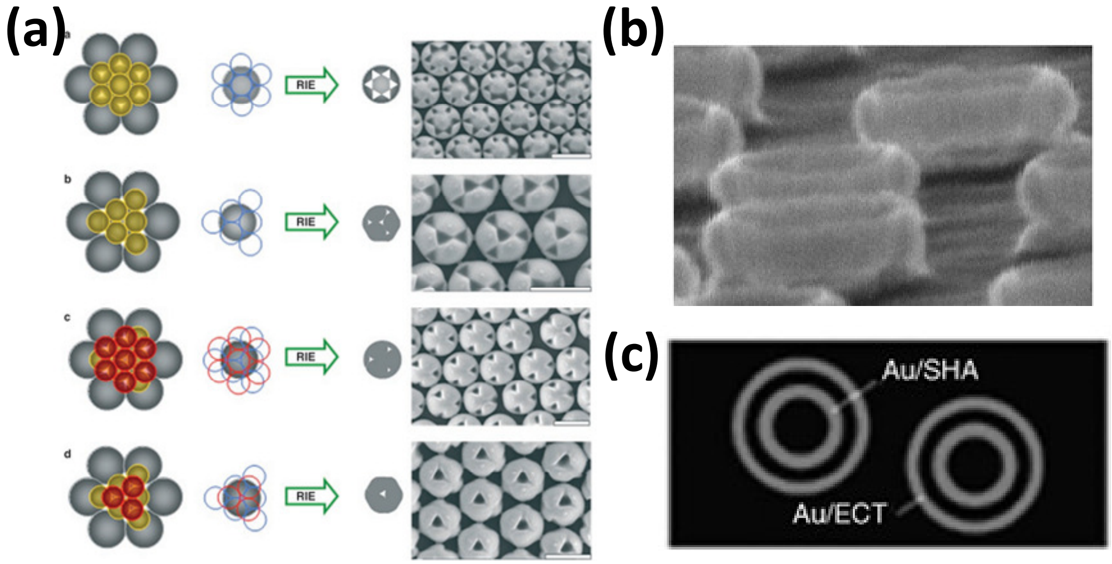

Figure 1.13 (a) Textured colloidal particles formed via colloidal lithography using layered template made of particles of different sizes. (b) single and (c) double metal ring particle made by surface modified etching using colloidal template as mask. Images adopted from reference [37].

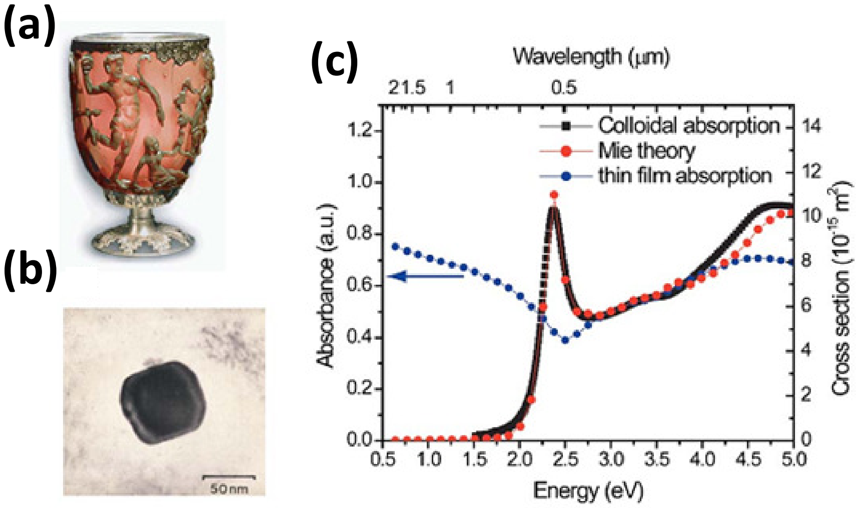

Figure 1.14 (a)The Lycurgus glass cup, demonstrating the bright red color of gold nanocrystals in transmitted light. (b) SEM image of a typical nanocrystal embedded in the glass. (c) Calculated absorption spectrum of a thin gold film (blue dots) and of 30-nm Au nanoparticles in water (red dots) using classical electromagnetic theory. A measured absorption spectrum of an aqueous solution of 30-nm Au colloids (black dots) shows good agreement with the theory. Image adopted from Reference [40].

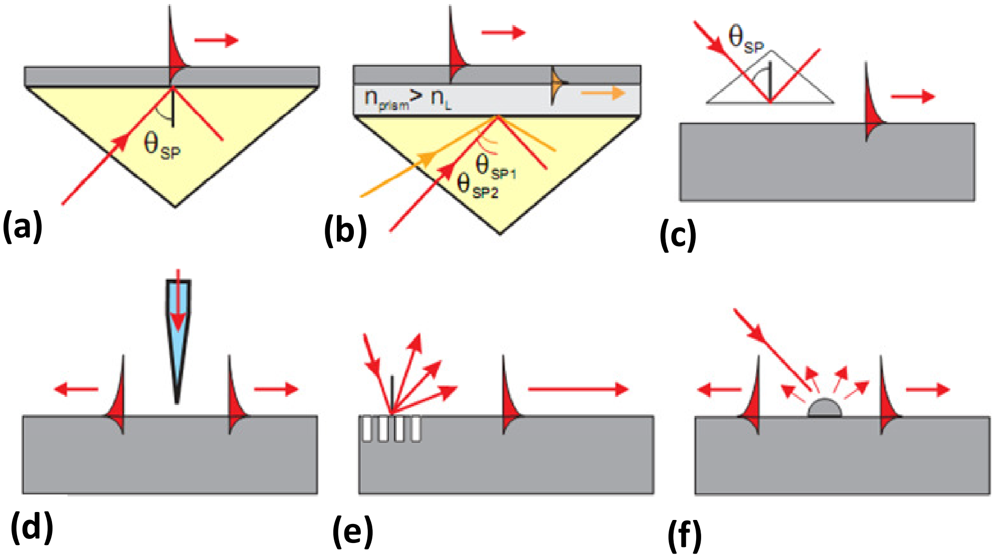

Figure 1.15 SPP excitation configurations: (a) Kretschmann geometry, (b) two-layer Kretschmann geometry, (c) Otto geometry, (d) excitation with a SNOM probe, (e) diffraction on a grating, and (f) diffraction on surface features. Figure adopted from reference [40].

1.7 Reference

1. Eckert, A. W., *The World of Opals*. John Wiley & Sons, Inc.: New York, NY, 1997.
2. Sanders, J. V. *Nature* **1964,** 204, (496), 1151-&.
3. Prather, D. W.; Shi, S. Y.; Murakowski, J.; Schneider, G. J.; Sharkawy, A.; Chen, C. H.; Miao, B. L. *Ieee Journal of Selected Topics in Quantum Electronics* **2006,** 12, (6), 1416-1437.
4. Blanco, A.; Chomski, E.; Grabtchak, S.; Ibisate, M.; John, S.; Leonard, S. W.; Lopez, C.; Meseguer, F.; Miguez, H.; Mondia, J. P.; Ozin, G. A.; Toader, O.; van Driel, H. M. *Nature* **2000,** 405, (6785), 437-440.
5. Davis, K. E.; Russel, W. B.; Glantschnig, W. J. *Journal of the Chemical Society-Faraday Transactions* **1991,** 87, (3), 411-424.
6. Wong, S.; Kitaev, V.; Ozin, G. A. *Journal of the American Chemical Society* **2003,** 125, (50), 15589-15598.
7. Jiang, P.; Bertone, J. F.; Hwang, K. S.; Colvin, V. L. *Chemistry of Materials* **1999,** 11, (8), 2132-2140.
8. Mihi, A.; Ocana, M.; Miguez, H. *Advanced Materials* **2006,** 18, (17), 2244-+.
9. Cheng, Z. D.; Chaikin, P. M.; Zhu, J. X.; Russel, W. B.; Meyer, W. V. *Physical Review Letters* **2002,** 88, (1).
10. Bamnolker, H.; Margel, S. *Journal of Polymer Science Part a-Polymer Chemistry* **1996,** 34, (10), 1857-1871.
11. Shen, S.; Sudol, E. D.; Elaasser, M. S. *Journal of Polymer Science Part a-Polymer Chemistry* **1993,** 31, (6), 1393-1402.
12. Wang, Y. L.; Ibisate, M.; Li, Z. Y.; Xia, Y. N. *Advanced Materials* **2006,** 18, (4), 471-+.
13. Checoury, X.; Enoch, S.; Lopez, C.; Blanco, A. *Applied Physics Letters* **2007,** 90, (16).
14. Elliot, M. S.; Bristol, B. T. F.; Poon, W. C. K. *Physica A* **1997,** 235, (1-2), 216-223.
15. Garcia-Santamaria, F.; Miguez, H.; Ibisate, M.; Meseguer, F.; Lopez, C. *Langmuir* **2002,** 18, (5), 1942-1944.
16. Chabanov, A. A.; Jun, Y.; Norris, D. J. *Applied Physics Letters* **2004,** 84, (18), 3573-3575.
17. Jiang, P.; McFarland, M. J. *Journal of the American Chemical Society* **2004,** 126, (42), 13778-13786.
18. Pavarini, E.; Andreani, L. C.; Soci, C.; Galli, M.; Marabelli, F.; Comoretto, D. *Physical Review B* **2005,** 72, (4), 9.
19. Busch, K.; John, S. *Physical Review E* **1998,** 58, (3), 3896-3908.
20. Vlasov, Y. A.; Bo, X. Z.; Sturm, J. C.; Norris, D. J. *Nature* **2001,** 414, (6861), 289-293.
21. Miguez, H.; Chomski, E.; Garcia-Santamaria, F.; Ibisate, M.; John, S.; Lopez, C.; Meseguer, F.; Mondia, J. P.; Ozin, G. A.; Toader, O.; van Driel, H. M. *Advanced Materials* **2001,** 13, (21), 1634-+.
22. Juarez, B. H.; Garcia, P. D.; Golmayo, D.; Blanco, A.; Lopez, C. *Advanced Materials* **2005,** 17, (22), 2761-+.

23. King, J. S.; Heineman, D.; Graugnard, E.; Summers, C. J. *Applied Surface Science* **2005,** 244, (1-4), 511-516.
24. Zakhidov, A. A.; Baughman, R. H.; Iqbal, Z.; Cui, C. X.; Khayrullin, I.; Dantas, S. O.; Marti, I.; Ralchenko, V. G. *Science* **1998,** 282, (5390), 897-901.
25. Gaillot, D.; Yamashita, T.; Summers, C. J. *Physical Review B* **2005,** 72, (20), 10.
26. Velev, O. D.; Tessier, P. M.; Lenhoff, A. M.; Kaler, E. W. *Nature* **1999,** 401, (6753), 548-548.
27. Vlasov, Y. A.; Yao, N.; Norris, D. J. *Advanced Materials* **1999,** 11, (2), 165-169.
28. Shimmin, R. G.; Vajtai, R.; Siegel, R. W.; Braun, P. V. *Chemistry of Materials* **2007,** 19, (8), 2102-2107.
29. Zhang, X. B.; Guo, C. C.; Li, Z. Z.; Shen, G. L.; Yu, R. Q. *Analytical Chemistry* **2002,** 74, (4), 821-825.
30. Denny, N. R.; Han, S. E.; Norris, D. J.; Stein, A. *Chemistry of Materials* **2007,** 19, 4563-4569.
31. Jiang, P.; Bertone, J. F.; Colvin, V. L. *Science* **2001,** 291, (5503), 453-457.
32. Bartlett, P. N.; Baumberg, J. J.; Coyle, S.; Abdelsalam, M. E. *Faraday Discussions* **2004,** 125, 117-132.
33. Lee, Y. C.; Kuo, T. J.; Hsu, C. J.; Su, Y. W.; Chen, C. C. *Langmuir* **2002,** 18, (25), 9942-9946.
34. Cassagneau, T.; Caruso, F. *Advanced Materials* **2002,** 14, (1), 34-38.
35. Haynes, C. L.; Van Duyne, R. P. *Journal of Physical Chemistry B* **2001,** 105, (24), 5599-5611.
36. Zhang, G.; Wang, D. Y.; Mohwald, H. *Nano Letters* **2007,** 7, 3410-3413.
37. Yang, S. M.; Jang, S. G.; Choi, D. G.; Kim, S.; Yu, H. K. *Small* **2006,** 2, (4), 458-475.
38. Jensen, T. R.; Malinsky, M. D.; Haynes, C. L.; Van Duyne, R. P. *Journal of Physical Chemistry B* **2000,** 104, (45), 10549-10556.
39. Rindzevicius, T.; Alaverdyan, Y.; Dahlin, A.; Hook, F.; Sutherland, D. S.; Kall, M. *Nano Letters* **2005,** 5, (11), 2335-2339.
40. Zayats, A. V.; Smolyaninov, II; Maradudin, A. A. *Physics Reports-Review Section of Physics Letters* **2005,** 408, (3-4), 131-314.
41. Barnes, W. L.; Dereux, A.; Ebbesen, T. W. *Nature* **2003,** 424, (6950), 824-830.
42. Maier, S. A.; Atwater, H. A. *Journal of Applied Physics* **2005,** 98, (1).
43. Salomon, L.; Bassou, G.; Aourag, H.; Dufour, J. P.; de Fornel, F.; Carcenac, F.; Zayats, A. V. *Physical Review B* **2002,** 65, (12).
44. Raether, H., *Surface Plasmons*. Springer-Verlag: Berlin, 1988.
45. Kretschm.E; Raether, H. *Zeitschrift Fur Naturforschung Part a-Astrophysik Physik Und Physikalische Chemie* **1968,** A 23, (12), 2135-&.
46. Homola, J. *Analytical and Bioanalytical Chemistry* **2003,** 377, (3), 528-539.
47. Takeda, S.; Wiltzius, P. *Chemistry of Materials* **2006,** 18, (24), 5643-5645.

CHAPTER 2
VARIABLE POROSITY METALLIC INVERSE OPALS FOR NARROW BAND THERMAL EMISSION APPLICATIONS

(Adapted in part from Xindi Yu et al, Adv. Mat. 2007)

2.1 Introduction

Metallic photonic crystals, metal based structures with periodicities on the scale of the wavelength of light, have attracted considerable attention due to the potential for new properties, including the possibility of a complete photonic band gap with reduced structural constraints compared to purely dielectric photonic crystals[1], unique optical absorption and thermally stimulated emission behavior [2, 3], and interesting plasmonic physics [4]. Photonic applications may include high efficiency light sources [5], chemical detection [6], and photovoltaic energy conversion [3]. Other applications for three-dimensionally porous metals, so called "metal foams", include acoustic damping, high strength to weight structures, catalytic materials, and battery electrodes [7]. The photonic properties of metallic inverse opal structures have been of significant interest because of the simplicity of fabrication and potential for large area structures. However, in practice, experiments on metal inverse opals have been inconclusive prior to this work [8-10], presumably because of structural inhomogeneities due to synthetic limitations. In this work, we demonstrate an electrochemical approach for fabricating high quality metal inverse opals with complete control over sample thickness, surface topography and for the first time, the structural openness (metal filling fraction). Optical measurements conclusively demonstrate that metal inverse opals modulate the absorption and thermal emission of the metal and that these effects only become three-dimensional (3D) in nature at high degrees of structural openness.

2.2 Nickel Inverse Opal Preparation

2.2.1 Conductive Substrate Preparation

The fabrication process of basic metallic inverse opal in this work follows a template assisted process that has been demonstrated before [11]. Basically a conductive substrate is first prepared by evaporating a thin film (~50 nm) of gold on a silicon wafer with chromium adhesion layer (1~5 nm). The substrate is then cleaned in piranha solution (3:1 mixture of sulfuric acid and 30% hydrogen peroxide) at ~100 °C for 1~5 mins, followed by rinse clean in DI water and blow dry in N_2. The substrates are then soaked in 10mM 3-Mercapto-1-propanesulfonic acid, sodium salt ($HS\text{-}(CH_2)_3\text{-}SO_3Na$) aqueous solution for more than 1 hour to form a monolayer of negatively charged molecules on the gold surface. After another rinse in deionized (DI) water and dry in N_2, the substrates are ready to use. Alternatively, if other metals are used instead of gold, whose native oxide provides a high enough surface charge density, the step of self assembled monolayer treatment can be skipped. Tungsten is one of those metals.

2.2.2 Colloidal Crystal Growth on Conductive Substrate

The next step is to grow colloidal crystal on these substrates through vertical deposition process (see chapter 1 for details). Sulfate terminated polystyrene particles are used, with diameter ranging from 500 nm to 2.8 μm. The charge of the colloids is chosen to be the same as the SAM layer to avoid colloids from randomly pack on the substrate due to long range electrostatic interaction. Most of the work conducted here is based on 2.2 μm and 1.8 μm diameter particles because of their monodispersity and high enough surface charge to enable the formation of high quality opal structure.

2.2.3 Electrodeposition through Template

As grown, the colloidal particles are held together by weak Van der Waals VdW force, which turns out to be too weak to have the crystal survive the later processing steps. To improve on this, colloidal crystals are sintered at temperatures slightly lower than the glass transition temperature of the polymer (PS), which is at 105 °C. The idea is to allow particles to deform in a slow and controllable way. Exact sintering temperature varies from a batch of particle to another, but in the range of 85 °C to 95 °C, with time duration of 1~5 hours. Over-sintering induces

too much lateral shrinkage, although the interconnection between the spheres becomes very strong, the whole film tends to detach from the substrate. So, correct sintering parameters are quite essential. Also, I always allow the heating system to ramp up and down slowly (>30min) to ensure negligible thermal stress.

Nickel is then electrodeposited into the colloidal template. Various metals, e.g. Au, Ag W, Pt, Pd, Co, Ni and Zn [10-14], have been formed into inverse opals. Here, nickel is selected because of its high reflectivity in the infra-red, temperature stability, and ease of electrochemical processing. The final thickness of the template nickel film is regulated by controlling the total charge passed during deposition. After electrodeposition, the PS microspheres are removed with tetrahydrofuran, resulting in a nickel inverse opal. Although the electrodeposition is quite homogeneous, gradual thickness variations do occur over the sample surface. These variations turn out to be useful, as they generate regions of different number of layers and surface terminations over the same sample (Fig. 2.1). SEM reveals a direct correspondence between the color, green, red or yellow, and the surface termination. As the color goes from green to red to yellow, the surface topography goes from shallow to deep bowl-like features, to deep cavities with openings at the top, as expected for electrodeposition through a layer of colloidal particles.

2.3 Optical Property of Nickel Inverse Opal as Prepared

The reflectivity of a nickel inverse opal with varying surface termination is collected at normal incidence using an FTIR microscope (Fig. 2.1c). The three different surface terminations exhibit very different properties, and agree qualitatively with previous observation on monolayer cavity structures [15]. Our data is consistent with a model where the optics are essentially due to a combination of Bragg plasmon and Mie plasmon interactions in the top layer of the structure [15]. Light does not directly penetrate into the structure due to the small skin depth of nickel (~20 nm in near to mid IR) and the small size of the windows that connect the spherical cavities (SEM micrographs in Figure 2.1). Despite the fact that Bragg surface plasmon modes and TM Mie plasmon modes can have strong field near the metal surface [16], which can result in propagation of light through a porous metal film [17], experimentally, we observe that plasmon based propagation of light into our structure is minimal. This is probably because the geometry of the top layer is different from that of interior layers, limiting the overall plasmon coupling efficiency.

2.4 Tuning Filling Fraction of Nickel by Electropolishing

To increase the penetration depth of light, and thus explore the effect of 3D periodicity on the optical properties, the windows that interconnect the spherical cavities must be enlarged. This perhaps could be accomplished by depositing material around the PS opal prior to metal deposition, for example, Al_2O_3 by atomic layer deposition, which would increase the size of the windows and decrease the overall metal filling fraction (FF). However, Al_2O_3 would also deposit as an insulating layer on the substrate, preventing electrodeposition. Our preferred route rather is to homogeneously remove metal from the metal inverse opal by electroetching, a procedure commonly known as electropolishing, after removal of the colloidal template.

Through control of the etching kinetics, the nickel inverse opals are uniformly etched through their entire thickness (Fig. 2.2b). The result of this etching can be structurally modeled as an increase in the diameter of the spherical cavities. The nickel FF after etching is determined by SEM measurements. This is done by measuring the size of the interconnection window. In ideal case, when spherical cavities are in mere contact, the contact window is infinitesimal. As the spherical cavity diameter increases, the window grows accordingly. Assume the original radius of the spherical cavity is R and the increase in that value is r. The radius of the window is x. The remaining filling fraction of metal is directly related to r which can be calculated through geometry, shown in figure 2.3.

2.5 Evolution of Optical Properties as Metal Filling Fraction Changes

$$\frac{x}{R} = \sqrt{(\frac{r}{R})^2 + 2(\frac{r}{R})}$$

The optical properties as a function of structural openness are determined by successive electropolishing steps followed by measurements of optical properties. After each etching step, SEM images are collected to verify the amount of nickel removed. All spectra are collected from the same region of the sample. Figure 2.2 presents both the reflectivity evolution and SEM images of the three distinct surface topographies (three color areas) as the nickel volume fraction is reduced. The optical properties change dramatically as the interconnections between voids become larger and the nickel FF is reduced. As nickel is removed, the reflectivity generally decreases and the main features in the spectra shift to longer wavelengths. The most dramatic change is that the reflectivity spectra of three different color areas, which initially are quite different, become fairly similar. Light now propagates deep into the structure and surface effects become much less important. The optical properties of the structure are now truly 3D.

To determine the penetration depth of light into the nickel inverse opal, the reflectivity as a function of the number of layers and metal FF is measured from samples one to five layers thick (Fig. 2.4), each partially or completely formed layer is counted as one layer. Only the red color area is presented in figure 2.4, the other two color areas exhibit similar behavior. In each graph, the four curves correspond to the four levels of etching exhibited in Figure 2.2a. Before etching, the spectra of all five samples are nearly identical, confirming that light is only interacting with the surface layer. As the structure opens up, spectra from samples of different thickness diverge. After the first etching step (red trace), the monolayer optical properties are different than the multilayer samples, but all multilayer samples are similar. By the final etching step (blue trace), the four and five layer samples are still similar, but the optical properties of the monolayer through three layer samples are different. Qualitatively, this data indicates that light substantially penetrates three to four layers into the fully etched samples (~5% nickel by volume). The limited penetration depth is further confirmed by the less than 1% transmission through a free standing six layer sample consisting of ~5% nickel by volume, over all investigated wavelengths (Fig. 2.5).

2.6 Thermal Emission Property of Nickel Inverse Opal

The thermal emission properties of metallic photonic crystals have been of considerable interest [2, 5, 18]. Kirchoff's law states that emissivity (ε) and absorptance (α) of an object are equal for systems in thermal equilibrium. For the nickel inverse opals studied here, where transmission is negligible and Bragg scattering from the triangular pattern at the surface does not occur at wavelengths longer than ~1.9µm for 2.2µm spheres, in the sample normal direction, $\varepsilon = \alpha = 1 - R$ with R being reflectivity. Emission measurements are performed by heating the nickel photonic crystal to ~450 ºC in a reductive atmosphere (5% H_2 in Ar); the thermal emission is collected by the FTIR microscope. Emissivity is obtained by normalizing the emission from the Ni samples to that from the reference blackbody, a carbon black coated silicon wafer heated to the same temperature under Ar (Fig. 2.6a). Emissivity from samples of different structural openness, ranging from 26% to 5% Ni by volume as before, is plotted together with reflectivity. Only data taken from the red color area is presented, data from other two color areas show similar effects. Spectra are grouped in pairs: each pair of the same color belongs to same structure openness. Emissivity appears as a mirror image of reflectivity ($\varepsilon = 1\text{-R}$) even down to fine details for all wavelengths above 2μm, confirming that the emission from the metal photonic crystal is modulated in a similar fashion as the reflectance. For wavelengths below 2μm, the relationship disappears as Bragg scattered light is not collected, leading to an underestimation of the reflectivity. Emissivity in some cases slightly exceeds 1, almost certainly because the surface temperature of nickel samples is slightly higher than that of the reference sample; a temperature difference of ~5 ºC is sufficient to explain this result. The emission of the carbon black reference sample is greater, and thus it is slightly cooler than the metal inverse opals, even though the temperature of the substrate heater is the same for both experiments. Comparing the emission spectra with those of other metallic structures [2], our system does not suppress thermal emission as efficiently, resulting in a broader high emissivity envelope.

2.7 Thermal Stability of Nickel Inverse Opal

A nickel inverse opal on silicon can be heated to ~550 ºC without structural degradation. However once heated to 600 ºC, it significantly collapses, even under a reductive atmosphere (Fig. 2.6b). For thermal emission applications, it may be desirable for the metal structure to survive at higher temperature, for example, at 700 ºC, blackbody emission peaks near 3μm. To protect the inverse opal structure, a 50nm layer of Al_2O_3 is coated on the sample via atomic layer deposition. No change is observed in reflectivity or SEM images before and after the sample is held at 750 ºC for one hour under reductive atmosphere, the same treatment at 800 ºC results in only slight changes, indicating the Al_2O_3 layer increases the working temperature of the nickel structure by at least 200 ºC.

It turns out that the main reason for structure collapse is that Ni reacts with Si at elevated temperature for form nickel silicide. The 50nm Au/ 5nm Cr layer is not sufficient to block diffusion of nickel ions. A better process would be to use a silicon wafer with 200nm thermal grown oxide as diffusion barrier, followed by the same process. This will prevent silicide formation to at least 800 °C [19]. Knowing this problem, the thermal stability experiment is performed again on quartz substrate. The result shows that without Al_2O_3, grains of nickel grow to about 500 nm at 650 °C and at 750 °C, grain growth destroy the structure completely (Fig. 2.8). So, a stable surface oxide layer will improve the temperature stability of nickel even further. Depending the thermal stability, 1000 °C might not be unrealistic.

2.8 Conclusion

These experiments demonstrate that high quality three dimensional metallic photonic crystal structures can be made through a combination of colloidal crystal templated electrodeposition and electropolishing. Only after the structure is considerably opened up, allowing light to penetrate deep into the structure, do 3D optical properties appear. Emission is indeed strongly modified by the photonic crystal. Because our experiments have probed all possible degrees of structural openness and surface topographies, we are able to conclusively determine the maximum possible modulation of the emission for an FCC inverse opal structure. Although this modulation may not be sufficient for some applications, the electrochemical infilling and etching approach described here is quite flexible and is compatible with other methods commonly used to generate 3D photonic crystals, including laser holography [20], direct writing [21], and phase mask lithography [22]. It is likely a combination of these methods may generate structures with narrow emissive features.

2.9 Experimental

The substrate is prepared by evaporating ~50nm of gold on a 700μm thick silicon wafer using a 1~5 nm of chromium as an adhesion layer. It is then soaked in a saturated 3-Mercapto-1-propanesulfonic acid, sodium salt ($HS-(CH_2)_3-SO_3Na$) ethanol solution for 30 min forming a monolayer of hydrophilic molecules on the gold surface. 2.2 μm diameter sulfate terminated polystyrene spheres (*Molecular Probes Inc*) are formed into an opal film on this substrate via evaporative deposition at 50 ºC with a colloid volume concentration of 0.4% in water [23]. Ni is electrodeposited using the electrodeposition solution Techni Nickel S (*Technic Inc.*) under constant current mode (1 mA/cm^2) in a two electrode setup with a platinum flag as the anode. Electropolishing is performed using the solution, EPS1250 (*Electro Polish Systems Inc.*) under constant voltage mode (4V) in a two electrode setup with a stainless steel plate as cathode. Polishing is performed with 1sec pulses on 10sec intervals. The interval is selected to allow ions to diffuse in and out of the inverse opal between etching pulses. Optical measurements are carried out on a Bruker vertex 70 FTIR coupled with Hyperion 1000 microscope. A CaF_2 objective (2.4X, NA=0.07) is used for all measurements. A Linkam THMS600 heating chamber with a KBr window is used to heat the sample. Gas flow is regulated at 2 liter per min in all measurements. The substrate heater is set at 500 ºC for all emission experiments. Due to thermal resistance of the substrate, surface temperature of the substrate is about 50 ºC lower than that of the substrate heater. Temperature survivability studies are performed in a tube furnace (Lindberg Blue M) under a flowing reductive atmosphere (5% H_2 in Ar).

2.10 Figures

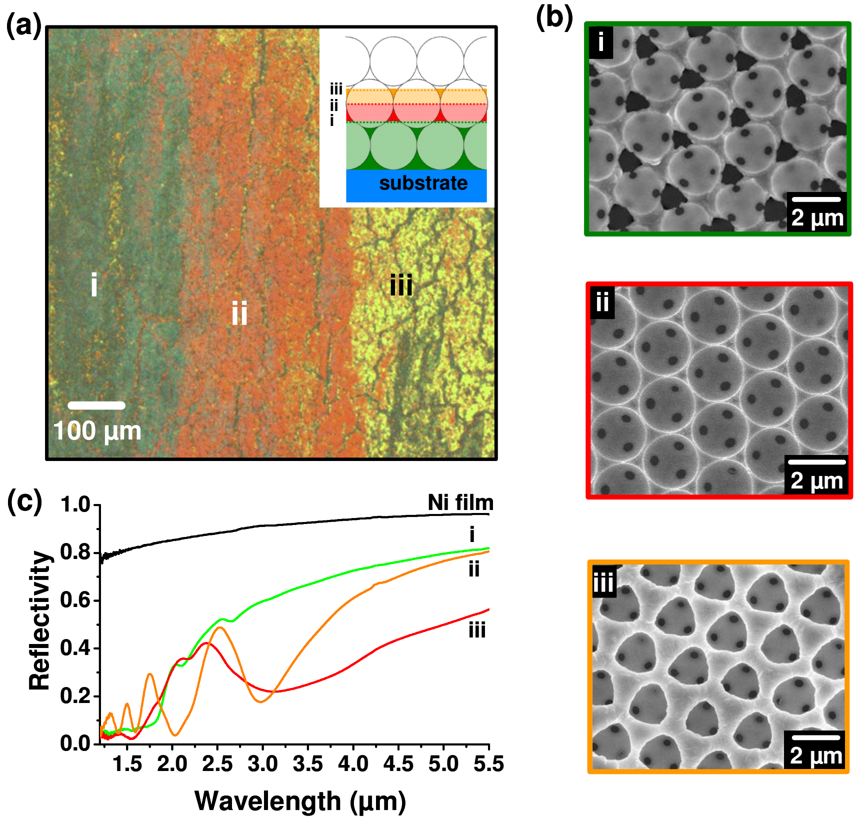

Figure 2.1. Electrodeposited nickel inverse opal. a) Optical micrograph of the nickel inverse opal; the different surface topographies appear green (i), red (ii), and yellow (iii). Inset: Nickel electrodeposition begins at the substrate and propagates upward. Top of the color bands correspond to the surface topography of three color regions observed under optical microscopy. b) SEM images of the three different surface topographies observed in (a). C, IR reflectance from the three color regions of an electrodeposited nickel film.

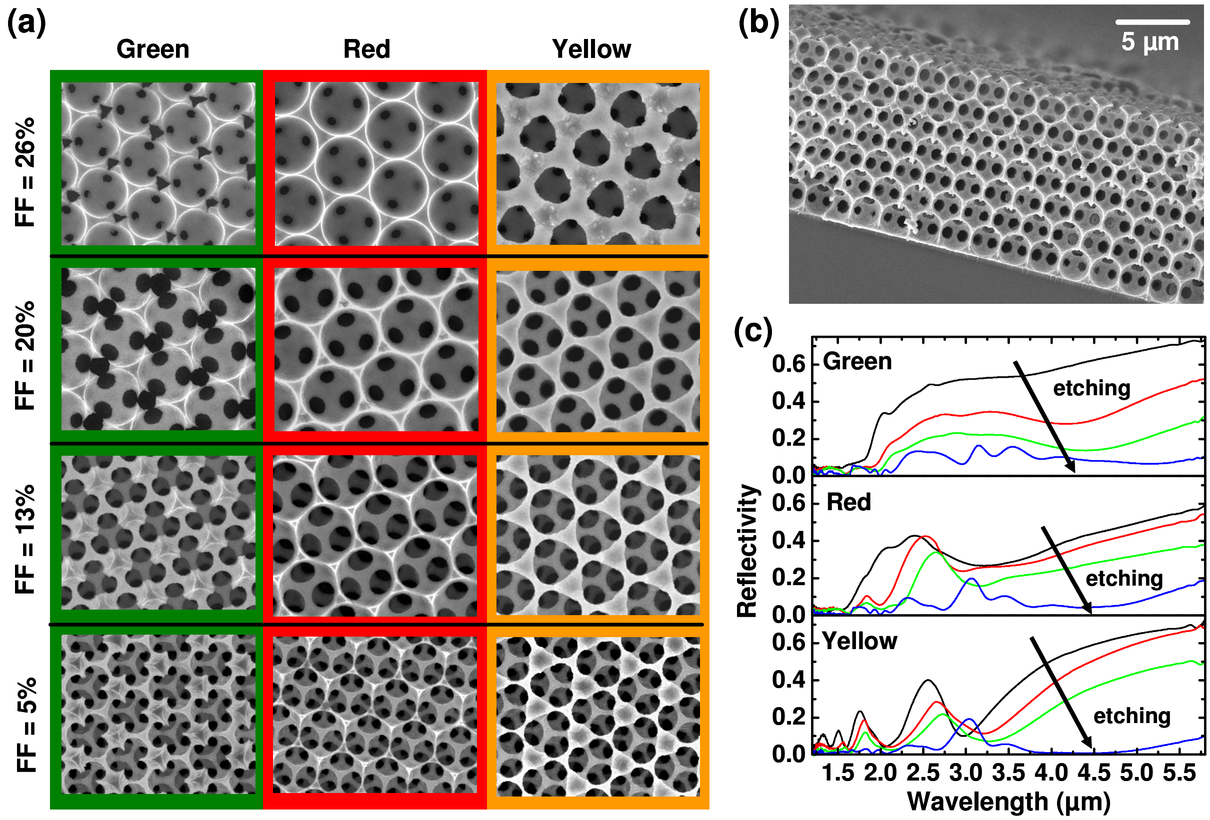

Figure 2.2. Increased structural openness by electropolishing. a) Top view SEM images of nickel inverse opal of different surface topographies and structure openness. The four rows present nominal nickel filling fractions (FF) of 26% (as deposited), 20%, 13%, and 5% (maximum etching before structural collapse). The three columns correspond to the three different surface topographies described in Figure 1. b) SEM image of nickel inverse opal cross-section after etching (nickel filling fraction = 13%). Etching is uniform throughout the thickness of the structure. c) Reflectivity evolution as nickel filling fraction reduces. Spectra are from the green, red and yellow regions. For each color region, the traces correspond to FF of 26% (black), 20% (red), 13% (green), and 5% (blue); matching the SEM images in (a). All SEM images and reflective spectra are taken on the same 4 to 5 layer thick sample.

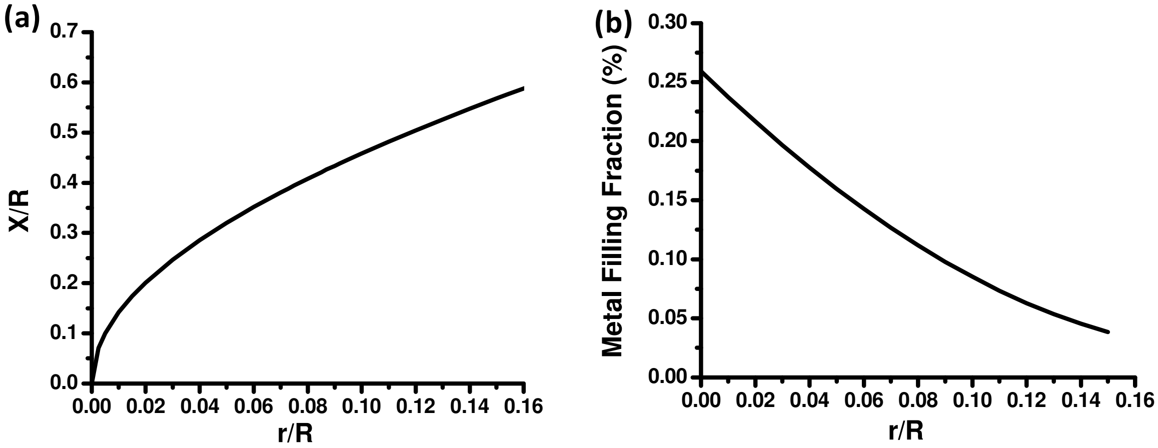

Figure 2.3. (a) Interconnection window relative radius (its ratio to spherical cavity radius) and (b) metal filling fraction as a function of relative spherical cavity radius change.

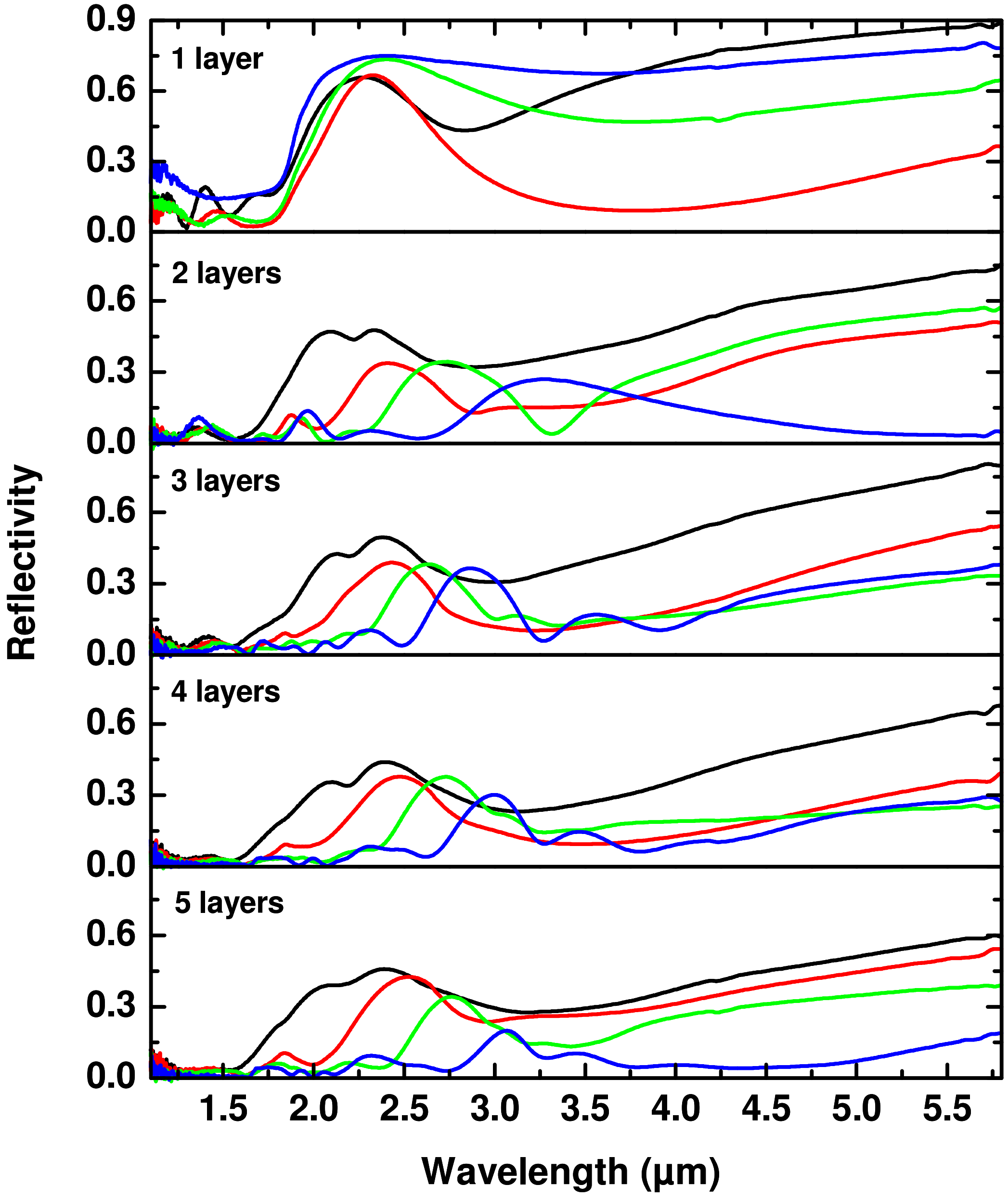

Figure 2.4. Nickel inverse opal reflectivity as function of thickness and FF. Reflectance spectra collected from 1 to 5-layer thick samples terminated with the “red” topography. Within each set of spectra, the color scheme corresponds to the four different nickel FFs presented in Figure 2.

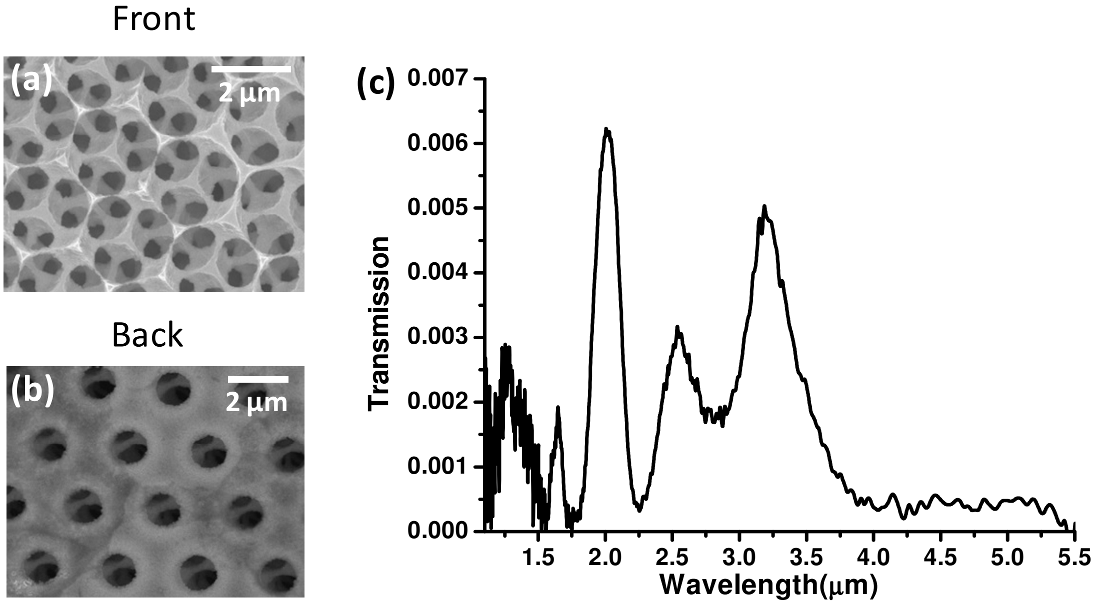

Figure 2.5 (a) Front surface and (b) back surface SEM images of a free standing low filling fraction (~5%) nickel inverse opal. (c) Transmission spectrum of the sample shown in (a) and (b).

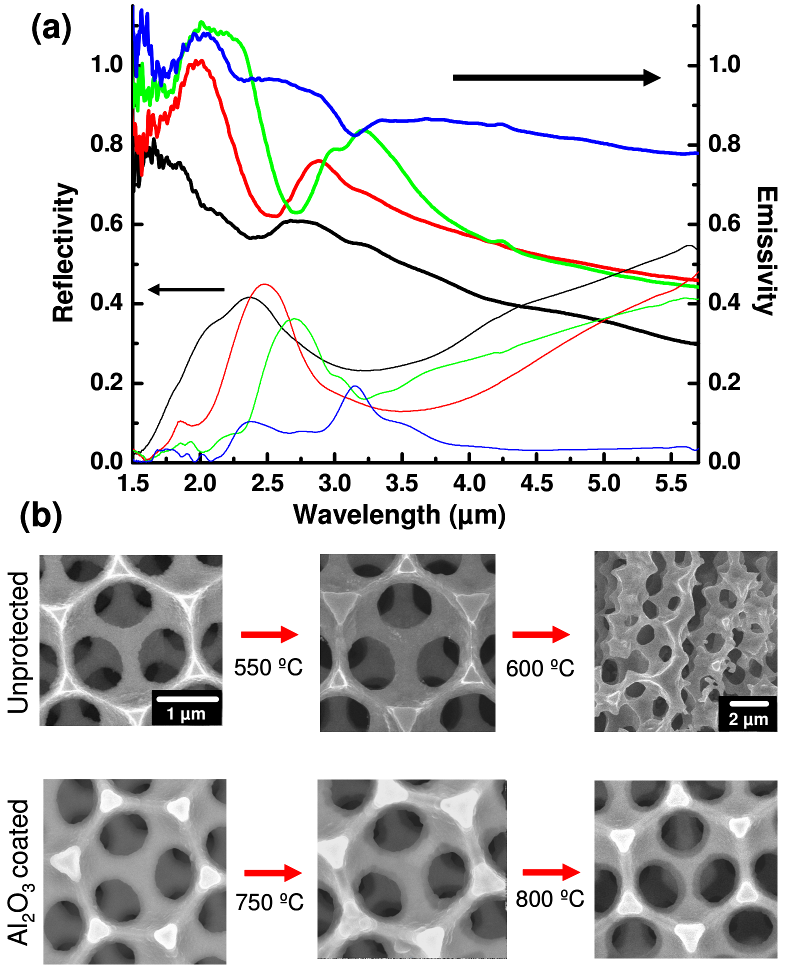

Figure 2.6. Emission and thermal stability of nickel inverse opal. a) Reflectivity and Emissivity measured from red topography area of nickel inverse opals are plotted together. Samples heated to ~450 ºC for emission studies. See text for details. Each pair of lines of the same color are taken from the same spot of a sample at the same FF. FFs correspond to those presented in Figure 2. Thick lines (emissivity) closely match one minus the thin lines (reflectivity), as expected. b) Top view SEM images of nickel inverse opal after heat treatment at various temperatures. The top row is an unprotected structure, the bottom row an Al_2O_3 protected nickel structure. Images are taken after holding the sample at the indicated temperature for one hour under a reductive atmosphere. All images are the same magnification except for the top right image, which is presented at a lower magnification as indicated to more clearly show the structural collapse.

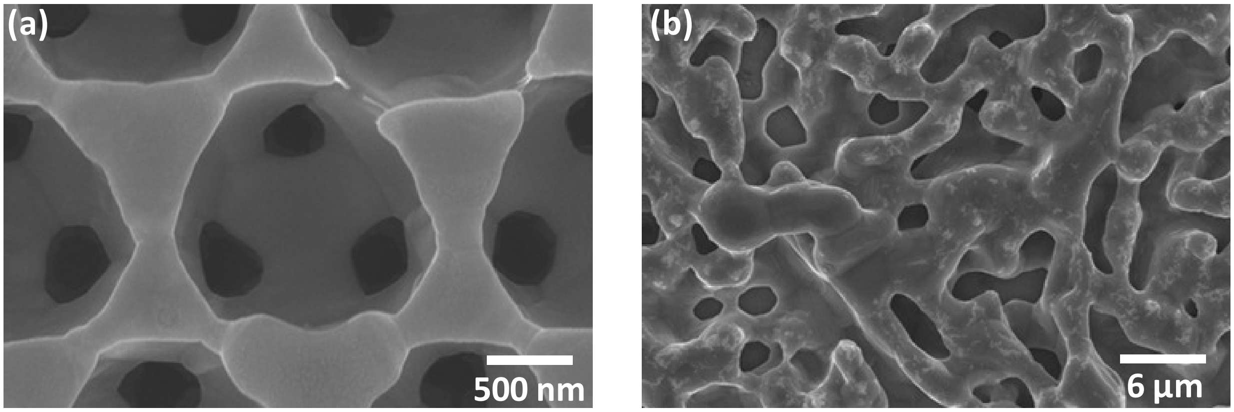

Figure 2.7. Nickel inverse opal fabricated on quartz substrate after thermal treatment at (a) 650 °C and (b) 750 °C for 1 hour under 5% H_2 in Ar.

2.11 Reference

1. Zhang, W. Y.; Lei, X. Y.; Wang, Z. L.; Zheng, D. G.; Tam, W. Y.; Chan, C. T.; Sheng, P. *Physical Review Letters* **2000,** 84, (13), 2853-2856.
2. Fleming, J. G.; Lin, S. Y.; El-Kady, I.; Biswas, R.; Ho, K. M. *Nature* **2002,** 417, (6884), 52-55.
3. Lin, S. Y.; Moreno, J.; Fleming, J. G. *Applied Physics Letters* **2003,** 83, (2), 380-382.
4. Ozbay, E. *Science* **2006,** 311, (5758), 189-193.
5. Puscasu, I.; Pralle, M.; McNeal, M.; Daly, J.; Greenwald, A.; Johnson, E.; Biswas, R.; Ding, C. G. *Journal Of Applied Physics* **2005,** 98, (1), 013531.
6. Baraton, M. I.; Merhari, L. *Synthesis And Reactivity In Inorganic Metal-Organic And Nano-Metal Chemistry* **2005,** 35, (10), 733-742.
7. Banhart, J. *Progress In Materials Science* **2001,** 46, (6), 559-632.
8. Pokrovsky, A. L.; Kamaev, V.; Li, C. Y.; Vardeny, Z. V.; Efros, A. L.; Kurdyukov, D. A.; Golubev, V. G. *Physical Review B* **2005,** 71, (16), 165114.
9. Li, W. J.; Sun, G.; Tang, F. Q.; Tam, W. Y.; Li, J. S.; Chan, C. T.; Sheng, P. *Journal Of Physics-Condensed Matter* **2005,** 17, (13), 2177-2190.
10. von Freymann, G.; John, S.; Schulz-Dobrick, M.; Vekris, E.; Tetreault, N.; Wong, S.; Kitaev, V.; Ozin, G. A. *Applied Physics Letters* **2004,** 84, (2), 224-226.
11. Bartlett, P. N.; Baumberg, J. J.; Coyle, S.; Abdelsalam, M. E. *Faraday Discussions* **2004,** 125, 117-132.
12. Bartlett, P. N.; Ghanem, M. A.; El Hallag, I. S.; de Groot, P.; Zhukov, A. *Journal Of Materials Chemistry* **2003,** 13, (10), 2596-2602.
13. Juarez, B. H.; Lopez, C.; Alonso, C. *Journal Of Physical Chemistry B* **2004,** 108, (43), 16708-16712.
14. Bartlett, P. N.; Birkin, P. R.; Ghanem, M. A. *Chemical Communications* **2000**, (17), 1671-1672.
15. Kelf, T. A.; Sugawara, Y.; Baumberg, J. J.; Abdelsalam, M.; Bartlett, P. N. *Physical Review Letters* **2005,** 95, (11), 116802.
16. Cole, R. M.; Sugawara, Y.; Baumberg, J. J.; Mahajan, S.; Abdelsalam, M.; Bartlett, P. N. *Physical Review Letters* **2006,** 97, (13).
17. Ebbesen, T. W.; Lezec, H. J.; Ghaemi, H. F.; Thio, T.; Wolff, P. A. *Nature* **1998,** 391, (6668), 667-669.
18. Chan, D. L. C.; Soljacic, M.; Joannopoulos, J. D. *Physical Review E* **2006,** 74, (1), 016609.
19. Lee, P. S.; Mangelinck, D.; Pey, K. L.; Ding, J.; Dai, J. Y.; Ho, C. S.; See, A. *Microelectronic Engineering* **2000,** 51-2, 583-594.
20. Escuti, M. J.; Crawford, G. P. *Optical Engineering* **2004,** 43, (9), 1973-1987.
21. Gratson, G. M.; Xu, M. J.; Lewis, J. A. *Nature* **2004,** 428, (6981), 386-386.

22. Jeon, S.; Park, J. U.; Cirelli, R.; Yang, S.; Heitzman, C. E.; Braun, P. V.; Kenis, P. J. A.; Rogers, J. A. *Proceedings Of The National Academy Of Sciences Of The United States Of America* **2004,** 101, (34), 12428-12433.
23. Colvin, V. L. *Mrs Bulletin* **2001,** 26, (8), 637-641.

CHAPTER 3
OTHER STRUCTURAL DESIGNS FOR NARROW BAND THERMAL EMISSION SYSTEMS

3.1 Introduction

The porous nickel system discussed in chapter 2 belongs to the family of 3D metallic photonic crystals, which have been shown to modulate light via strong coherent scattering and absorption [1-4]. A well acknowledged example is metallic woodpile structure [5] which has diamond lattice symmetry. Despite initial difficulty in fabrication, the woodpile geometry has been successfully made by different methods [6-10], followed by template assisted fabrication [11, 12]. Other than metallic woodpile structure, a modified metallic inverse opal structure has also been proposed [13],which shows, at least in simulation, superior performance compared with the metallic woodpile structure.

Metallodielectric systems of other dimensions (0D, 1D and 2D) also have been studied for thermal emission purposes. In 2D systems [14, 15], surface plasmon and photonic modes are taken advantage to achieve directionally and spectrally selective radiation. However, in most cases, direction and wavelength are correlated. In other words, narrow band emissions of different wavelengths emits in different directions, which could be a significant disadvantage for applications such as thermal photovoltaic devices.

1D systems based on metal dielectric multilayers have shown surprising narrow band radiation behavior and very good directional control. [16] However, 1D systems face a few grand challenges. First of all, thermal emission from a high temperature source covers a wide band from below 1 µm to above 10 µm. There are limited choices of dielectric materials that are transparent throughout the whole wavelength range. Furthermore, the choice of metal and dielectric materials should have similar thermal expansion coefficient to reduce stress build up during operation. (For example the linear thermal expansion coefficients of tungsten and CaF_2 (a typical IR transparent material) are 4.3ppm/K and 20ppm/K, respectively. For temperature change of 1000 °C, the stress built up in the film is on the order of a 1 GPa, which might cause creep, buckling, or rupture to occur.

0D systems based on resonance cavities appear as very attractive candidate for thermal emission [17]. The advantages are obvious: 1) there are no spatial correlation requirements between these cavities; 2) angular dependence is very weak; 3) band width of radiation can be potentially adjusted by mixing cavities of different geometries.

In this chapter, a few designs in 3D, 2D and 0D will be discussed.

3.2 Spherical Cavities with Cylindrical Interconnections (3D system)

3.2.1 Structural Design

It has been proposed that a modified 3D interconnected cavity network shows very narrow thermal emission features[13]. The proposed structure has spherical cavities connected by a relatively large connection window and a flat crystal air interface (Fig. 3.1). Although sharing many features with the structure discussed in chapter 2, the difference in between is significant enough to result in completely different optical behavior.

3.2.2 Fabrication

To fabricate such a structure requires similar approach that have been used to produce non-close packed colloidal structures[18], where a cylindrical connection is resulted between spherical cavities. However, in this case the window size will be much larger and uniformity over large sample area will be needed.

The proposed approach takes advantage of the irreversible process described in chapter 5, which result in an alumina disk between every pair of polystyrene particles after conformal coating and conformal etching. In this case, polystyrene colloidal crystal is grown on a conductive substrate (gold film evaporated on silicon for example). The resulting PS/Al_2O_3 composite will be the template in which electrodeposition of nickel will grow through and eventually form a solid thick nickel film (>10 µm). This thick film will help keeping the sample flat after it is released from the substrate. The silicon wafer to start with is preferred to be thin (~100 µm), and is eventually etched in 20% KOH at elevated temperature (~60 °C) after nickel plating. KOH attacks silicon and alumina during the process and leave polystyrene, nickel, gold and chromium intact. Chromium layer is then etched by one electropolishing pulse (see chapter 2.9 for details), followed by removing gold layer using a KI/I_2 based selective etchant. After this step, the bottom of the nickel layer, polystyrene and the bottom Al_2O_3 rings are exposed. The template can then be etched in KOH (for Al_2O_3) and THF (for PS).

3.2.3 Structural Parameters

According to the fabrication scheme outlined above, the diameter of the spherical cavities is the same as that of the colloidal particles. The cylinder diameter is however, determined by the size of the w rings. Assume the colloidal sphere has a radius of R=1, a conformal alumina coating thickness of x, which is also the conformal etching thickness. The range of x is between 0 and 0.15. The final radius of the ring particles is a function of x (see figure 3.2 for details). The maximum cylinder radius/sphere radius ratio is 0.4, smaller than the proposed 0.5. The consequence of this difference in optics needs further study.

3.3 Square Array of Inverse Pyramids (2D System)

3.3.1 Structural Design

Inverse metallic pyramid arrays of small periodicity have been applied as surface plasmon sensors in visible wavelengths with very high sensitivity [19]. The same structure with larger periodicity can be easily fabricated with optical lithography and selective etching. And similar response is expected with optical features in near infrared longer wavelengths. Although emission wavelength will be angular dependent, which is intrinsic to all propagating surface plasmon modes, structure of this kind can still be applied in particular applications where a broadband emission source and a grading is combined to get monochromatic light.

3.3.2 Fabrication

Fabrication starts with (100) terminated silicon wafer with a thick thermal oxide or silicon nitride (SiN) as etching mask layer. The surface is patterned by photolithography with square or circular hole array exposed. The directional RIE etches the mask layer and exposed the silicon surface. This is followed by anisotropic silicon etching. The etching mask can then be stripped by selective etching. The final result is an array of inverse pyramids with base angle of 54.7°. Metal can be directly deposited onto this template by physical vapor deposition with thickness larger than skin depth of the metal. In my study, gold, nickel, molybdenum have been used. Alternatively, the patterned silicon will function as a master. After surface fluorosilane treatment, PDMS will be cured on top of that to form a stamp. After separation from the master, this stamp will then be coated with a thin layer of metal (Ni for example) as seeding layer followed by electrodeposition. The metal foil will be peeled off from the stamp to get the final metal structure (See figure 3.3 for schematics).

3.3.3 Optical Property

Square inverse pyramid array with periodicity of 2 μm is commercially available (Klarite 302 by mesophotonics). The surface of that product is coated with a thick layer of gold with high roughness (Fig 3.4). After stripping away the gold layer, the smooth silicon surface is exposed. A 50 nm layer of gold with much smaller grain size and smoother surface is deposited on the sample surface via Ebeam evaporation (Fig. 3.5a).

Reflective spectrum in normal direction shows discrete and strong reflection minima (Fig 3.5b). When lens of different numerical apertures are used, which project and collect light at different ranges of directions, the feature around 1.8 µm remains at the same place with variations in intensity. Feature centered at 1.05 µm splits into double dips for high magnification lens. This result tends to indicate a propagating surface plasmon nature of the 1.05 µm feature and the origin of 1.8 µm feature remains unclear from this experiment.

It is well know that V shaped metal grooves support surface plasmon modes with well confined mode volume [20]. The bottom of the pyramid can be viewed as V groove in 2 perpendicular directions, which might support local resonance modes. However, the reflection minimum can also very well be resulted from scattering at wavelength smaller than the periodicity of the square array.

To further understand the optics of these devices, thermal emission is studied. Emission spectrum provides valuable information of the resonance modes, because reflection minima due to strong scattering do not show up in emission. To do that another sample is stripped of original gold coating and coated again with 100 nm of nickel with 5 nm chromium as adhesion layer. Reflection at normal direction is similar to the case of gold coated sample (Fig 3.6) with lower reflectivity at short wavelength due to lossier nature of nickel. Emissivity is then measured on this sample at different zenith and azimuthal angles (Fig 3.7). The result clearly indicate angular dependent dispersion relation, a signature of propagating surface plasmon based absorption system. So, the wide dip in normal reflection near 1.8 µm is indeed due to scattering (diffraction).

3.4 Monolayer of Spherical Cavities

3.4.1 Structural Design

Spherical cavities with highly reflective surface support distinctive resonance modes [21]. The idea of using arrays of spherical cavities as narrow band thermal emitters has recently been proposed [17]. The proposed structure has a monolayer of spherical colloidal particle arranged in a close packed fashion on a conductive substrate. Metal is then deposited via electrodeposition to a certain thickness and the particles are embedded in the metal, forming spherical cavities. The colloidal particles can then be removed to reach the final structure (Fig 3.8).

Obviously a nanoporous gold film is not compatible with high temperature applications due to its relatively low melting temperature. But the result shown there may also be transferred to structures made of other reflective metals. However, there are still some questions remaining, such as 1) whether the crystalline monolayer structure is needed to observe the same phenomena. 2) How sensitive is the optical response to surface termination. 3) How well does absorption observed translate to thermal emission at elevated temperature.

3.4.2 Fabrication

To answer these questions, some experiments reported in reference 17 is repeated. A monolayer of 1.8 μm diameter polystyrene particles are crystallized on gold surface. Nickel is electrodeposited in the template. Deposition is stopped multiple times during the process to take reflective measurements. The thicker the nickel layer, the more complete the spherical cavity is formed and the smaller the opening window of the cavity to outer space is. This fabrication procedure will be later called “top exposure”.

Alternatively, a thick layer of nickel is plated followed by etching away silicon substrate in KOH, and gold electrode layer in selective gold etchant. It is noticed that in most cases, a thin layer of nickel is formed between polystyrene spheres and the gold layer. This thin layer needs to be first removed by a few pulses of electropolishing. This opens up windows for optical coupling and chemical access to the cavity space. Colloids can then be removed by etching. This procedure will be later called “bottom exposure”.

As an extension of that, a random monolayer of colloids is formed by first destabilizing the colloidal solution (2%) with high concentration of salt (10mM $CaCl_2$). The destabilized solution is then casted on the substrate. Following the same electroplating/etching procedure mentioned above, a random monolayer of spherical cavities can be prepared. These samples will be called “random monolayer”.

3.4.3 Optical Property

For top exposure samples, reflective spectra are measured after different nickel electroplating duration. The first measurement is done after 3100 sec, when the growth front of nickel reaches roughly the equator of the spheres. The following measurements are taken at 600 sec. intervals of the plating time. From the spectrum (Fig 3.9), it is obvious that resonance features vary in intensity as the nickel thickness increases. More specifically, with the PS spheres in place, all resonance features grow stronger as the nickel covers more than half of the spheres and reaches a maximum at nickel thickness vs. sphere diameter $t/D{\sim}0.87$, and disappear at $t/D{\sim}1.1$, although at this moment, because of the growth pattern, connection windows remain on top of the spheres (Fig. 3.9b). Interestingly, after etching away the PS spheres, resonance blue shifts and becomes stronger, this indicates that for spherical cavities without dielectric filling, the coupling of light into the cavities is easier and the ideal metal thickness is higher than those with dielectric fillings.

Bottom exposure samples also show maximum mode coupling at certain opening window size. From geometrical calculation, t/D ~0.9 (Fig 3.10a). Random back exposure samples (Fig. 3.10b) show very similar behavior as crystalline samples, the slight red shift and broader peak width (Fig. 3.10c) is mainly due to more electropolishing pulses applied to the random sample and variation in t/D naturally associated with the random packing (Fig. 3.10b). This similarity is not surprising since the resonance is due to local response mode inside individual cavities. The geometrically arrangement of cavities should not have much impact.

Due to the similarity of three systems, only crystalline back exposure samples are extensively studied for their thermal emission properties. Measurement setup is similar to what is being used in chapter 2. The difference is that in this study, a manually adjustable tilting stage is built. So that angular dependent emission measurements are performed. (See figure 3.11 for experiment setup.) The emissivity spectrum (Fig 3.12) measured at normal direction matches very well with reflective spectrum. And emission remains at the same wavelength at angle smaller than 30°. At 45°, emissivity peak red shifts and reduces in intensity. Emission is not dependent on azimuthal angle by comparing figure 3.12b and figure 3.12a.

Multiply this emissivity to the blackbody emission intensity envelope, the emission intensity of the device at certain temperature can be predicted. Figure 3.13 shows such an emission spectrum at 1200K (927°C). Obviously, the emission peak is a lot narrower comparing with a black body emitter. From the reflection measurements shown earlier, all these properties are predicted to exist on top exposure and random cavity arrays.

Tuning of emission peak width is needed for applications such as thermal photovoltaic energy conversion. A broader emission peak can be achieved by mixing spherical particles of multiple diameters together in a random fashion and follow back side exposure fabrication scheme.

3.5 Conclusion

Examples of selective thermal emission discussed in this chapter are all based on optical resonance modes supported by metal structures. High selectivity, in other words, narrow emission bands correlates to the high quality factors of these resonance modes. For this purpose, more reflective and less lossy metals perform better. Reflective spectra of refractory metals and their melting temperatures are shown in figure 3.14. Tantalum appears to be the best material of choice. Combining structural design and the correct material choice, thermal emitters with appropriate band width can be engineered.

3.6 Figures

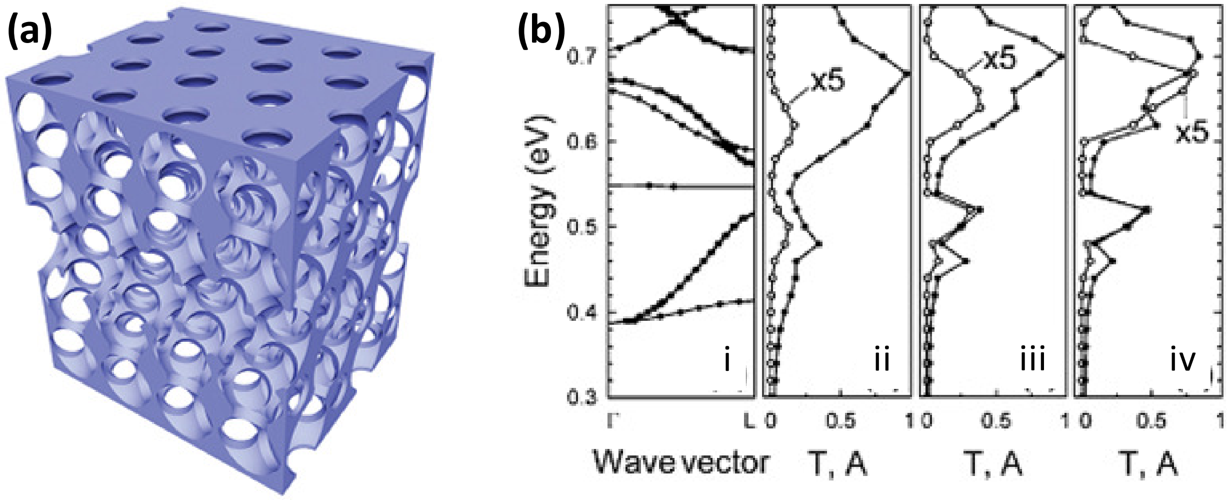

Figure 3.1 (Adopted from reference 13) (a) 3D visualization of the proposed structure. (b) (i) Calculated photonic band structure and (ii) optical transmittance T (open circles) and absorptance A (solid circles) along [111] for a 5-layer tungsten inverse opal with air cylinders. (iii),(iv) Calculations for analogous structures from molybdenum and tantalum, respectively. For all, we used sphere diameter D= 1.7 μm, cylinder diameter d/D = 0.5. T values are scaled by a factor of 5. In (i) no bands exist below 0.3 eV.

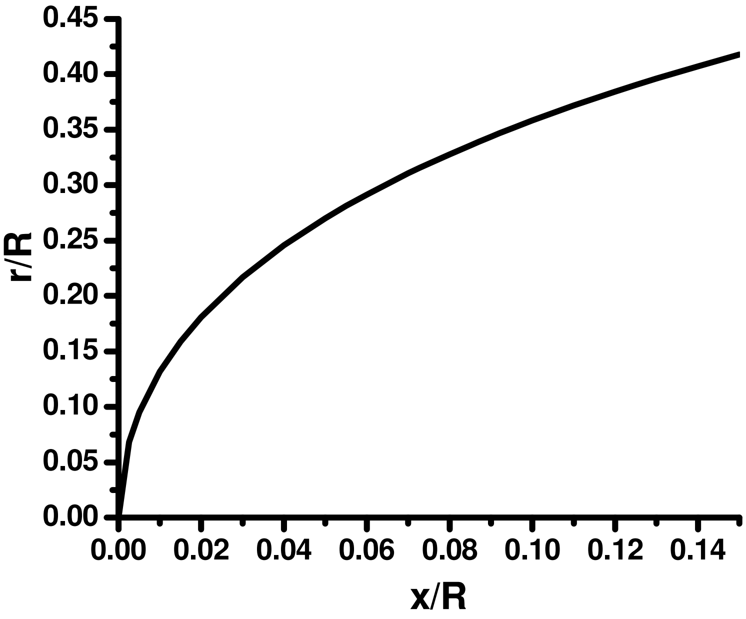

Figure 3.2 Cylinder diameter as a function of conformal coating and conformal etching thickness.

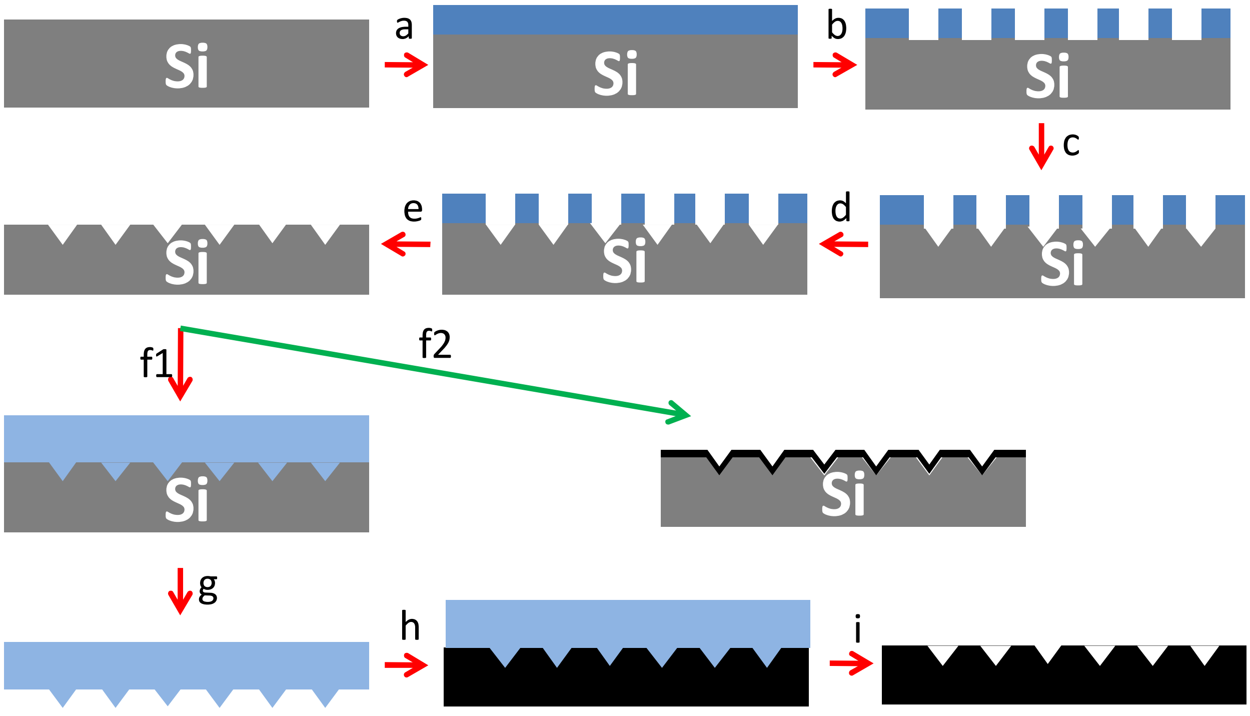

Figure 3.3 Fabrication Scheme of metal inverse pyramid array. See chapter 3.3.2 for details.

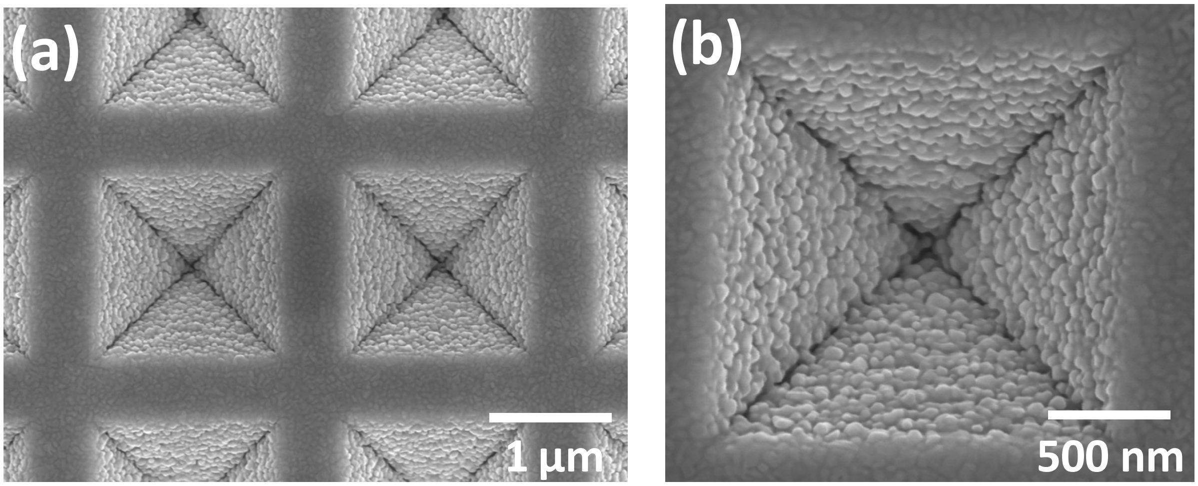

Figure 3.4 SEM images of commercial gold coated silicon inverse pyramid array (SERS sensor). (a) and (b) are images of different magnifications.

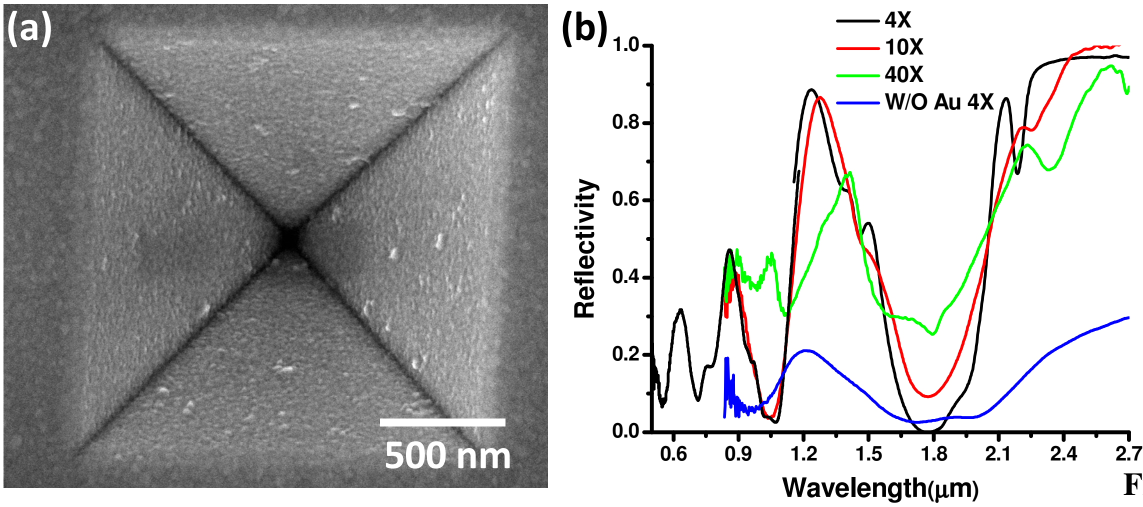

Figure 3.5 (a) top view SEM image of inverse pyramid array recoated with 50 nm gold. (b) reflective spectra at normal reflection under different conditions. Blue trace is from the silicon inverse pyramid array before metal coating measured with a 4X objective (NA=0.1). Black (4X, NA=0.1), red (10X, NA=0.25) and green (40X, NA=0.65) are measured after 50 nm gold coating with lens with different magnification and numerical apertures.

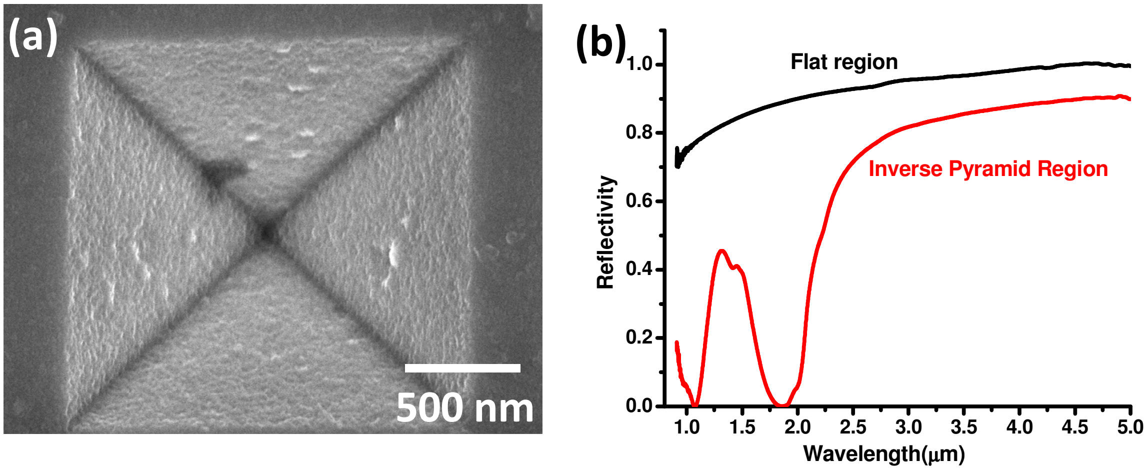

Figure 3.6 (a) top view SEM image of inverse pyramid array recoated with 100nm nickel. (b) reflective spectra at normal reflection for flat and structured region.

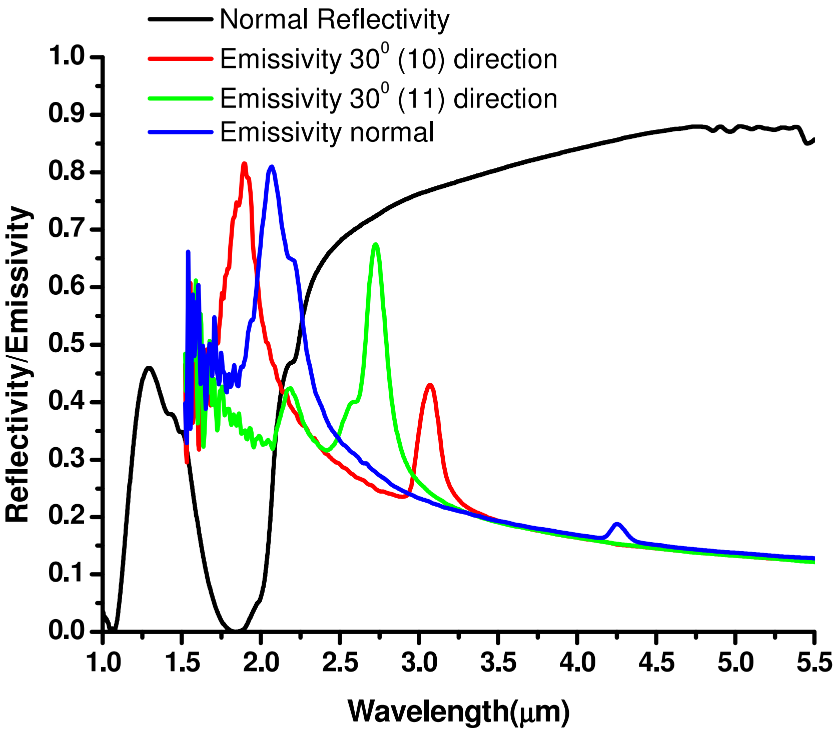

Figure 3.7 Emissivity of nickel inverse pyramid at different angles plot together with reflectivity collected at normal direction. Blue trace is taken at normal direction. Red and green trace are at 30° zenith angle and 0° and 45° azimuthal angle respectively.

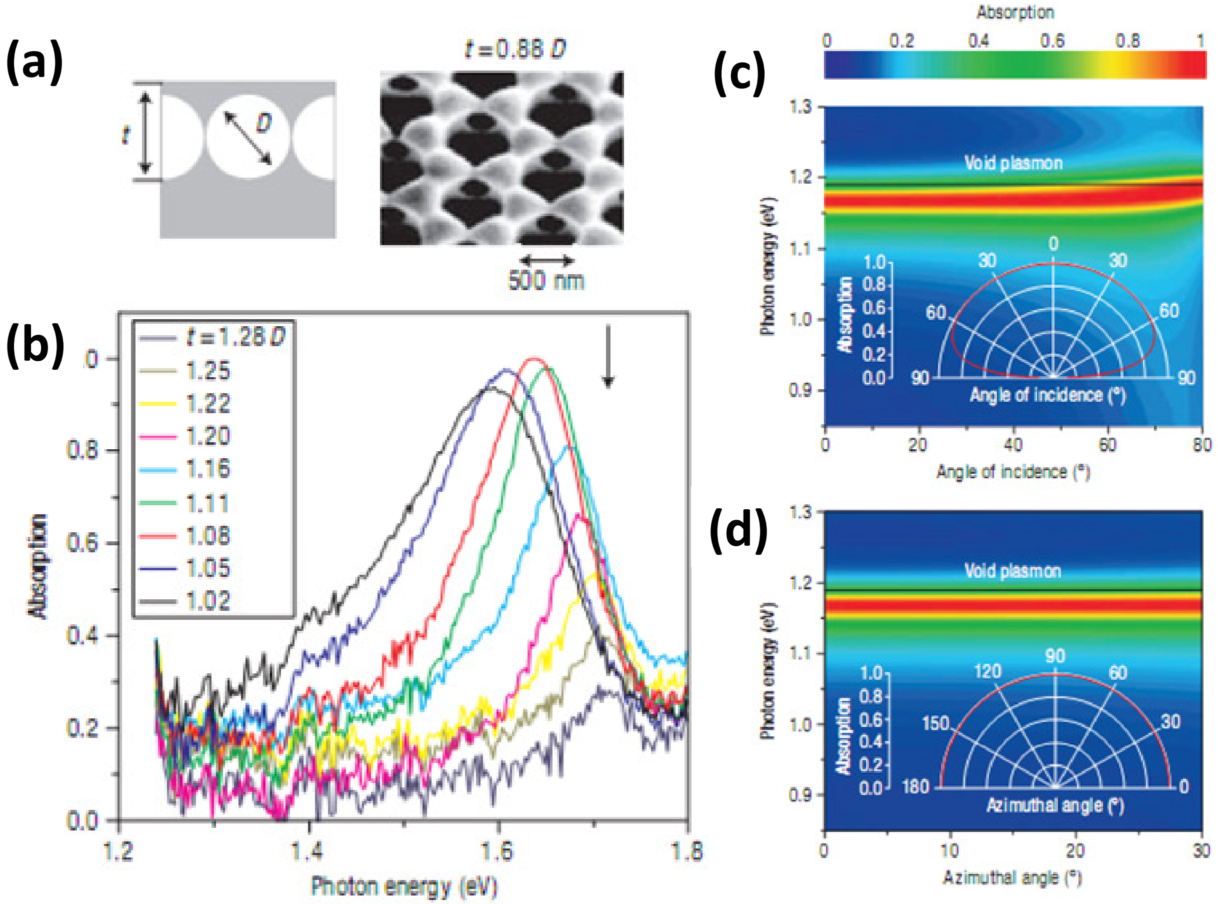

Figure 3.8 Adapted from reference 17. (a) Schematics and tiled top view SEM images of gold spherical cavity strutcure. (b) Absorption spectrum of the structure with different gold thickness at normal incidence. (c) Computer simulated zenith angle dependent absorption spectrum of a layer of 500-nm close-packed gold spherical cavities for p-polarized light incident along the G – M direction of the voids lattice. The metal extends 5 nm above the top of the inclusions to maximize absorption over a wide angular range. The cavities are filled with silica. (d), Under the same conditions as (c), azimuthal dependence of absorption for 20° off-normal incidence. The polar plot insets show the azimuthal angular behavior of absorption at the frequency of the dipolar void plasmon ω= 1.27 eV.

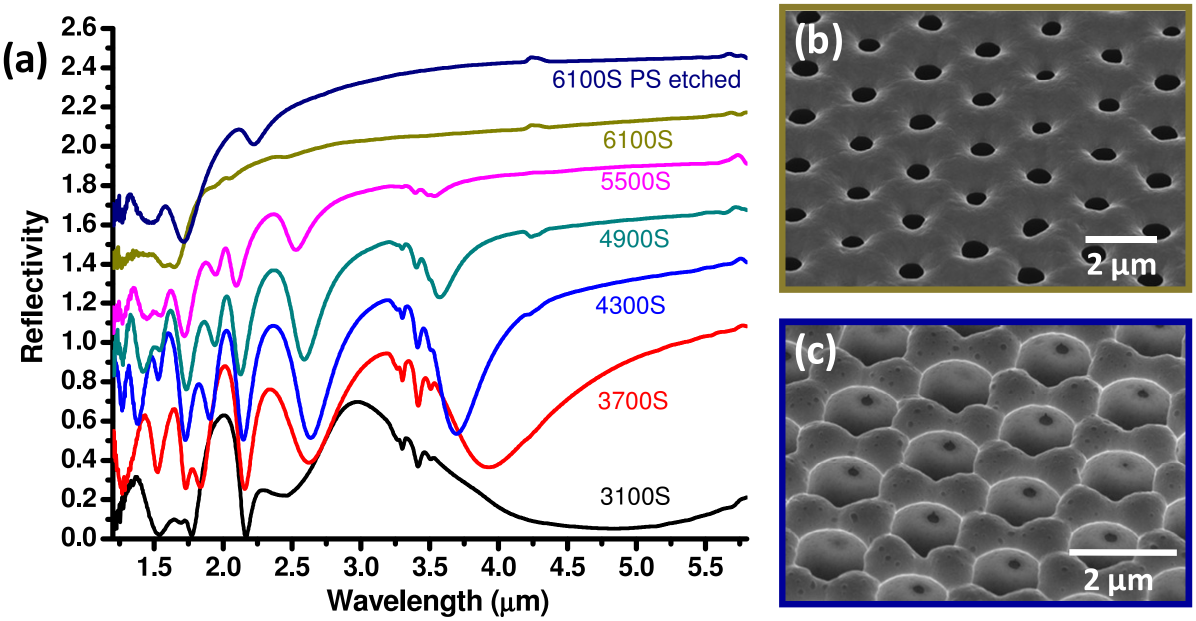

Figure 3.9 (a) Reflective spectrum evolution of top exposure nickel cavity structure as a function of nickel electroplating time. Each spectrum is offset for 0.25. (b) and (c) are tilted top view SEM images of the sample after 6100S and 4300S of nickel deposition and remove polystyrene template.

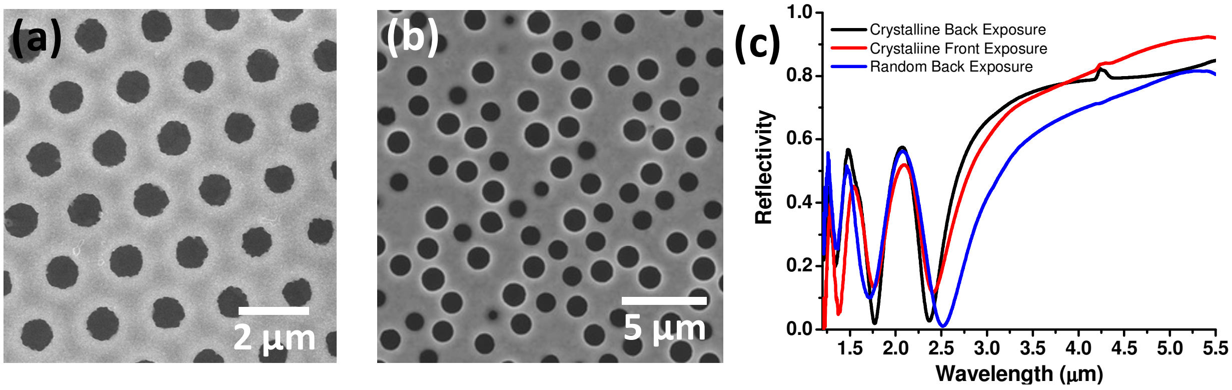

Figure 3.10 (a) and (b) Top view SEM images of crystalline and random back side exposure nickel spherical cavity structure. (c) Reflective spectrum for top exposure, back exposure and random nickel spherical cavities, all showing similar features.

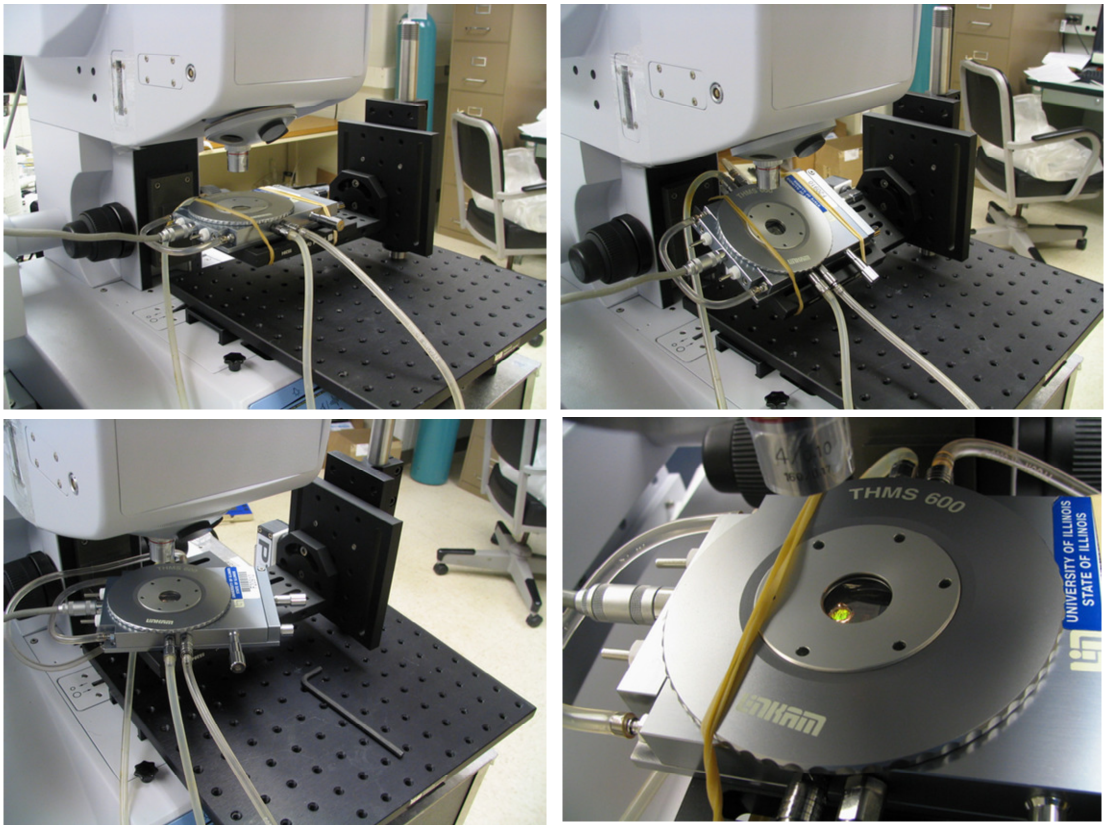

Figure 3.11 Angular dependent thermal emission setup.

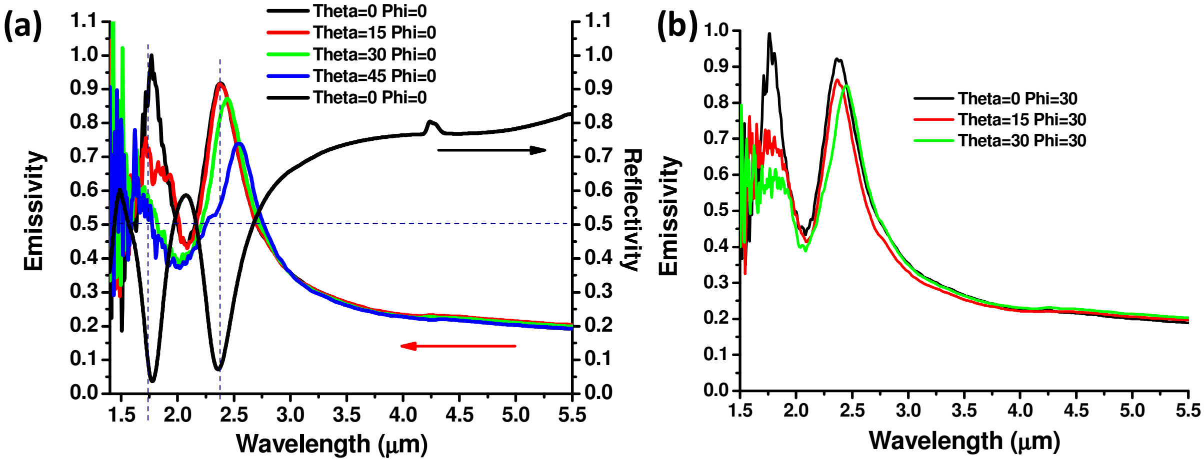

Figure 3.12 Angular dependent emissivity for back exposure nickel spherical cavities arranged in triangular lattice. (a) and (b) vary zenith angle (θ) while keep azimuthal angle (φ) at 0° and 30°. Emissivity shows weak dependence on θ and is independent to φ.

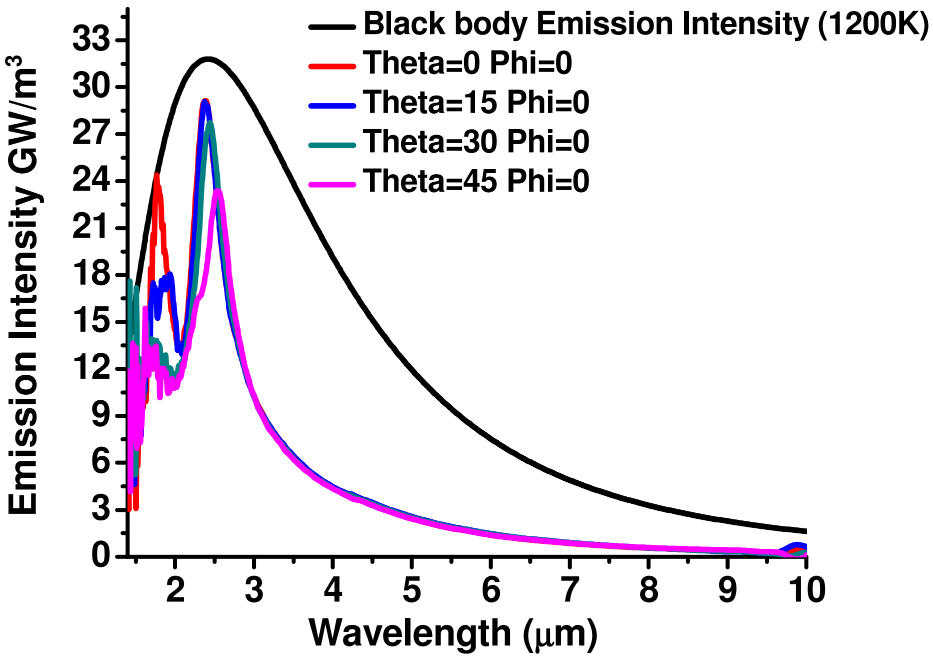

Figure 3.13 Emission spectrum at 1200K extrapolated from emissivity measured from nickel spherical cavities.

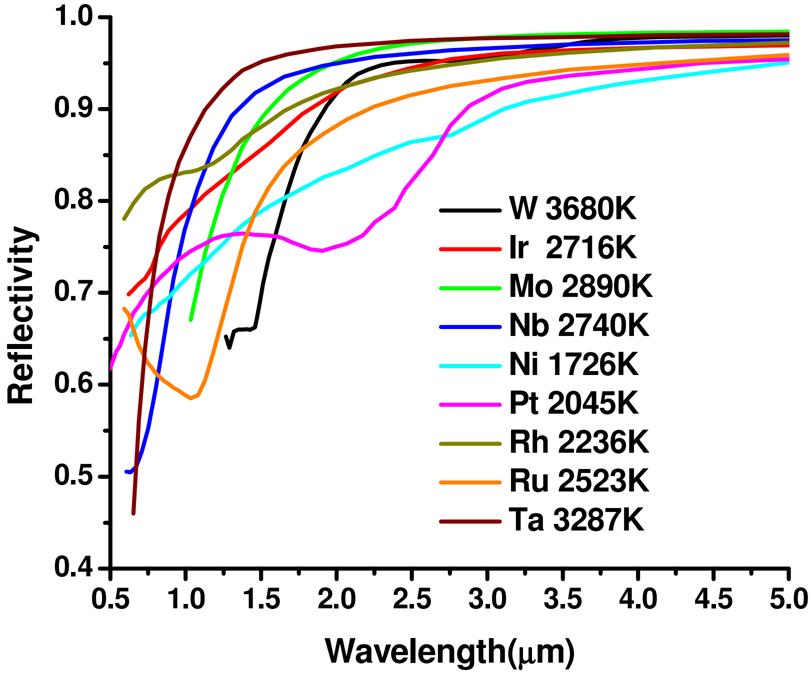

Figure 3.14 Reflective spectra and melting temperature of refractory metals.

3.7 Reference

1. Moroz, A. *Physical Review Letters* **1999,** 83, (25), 5274-5277.
2. Zhang, W. Y.; Lei, X. Y.; Wang, Z. L.; Zheng, D. G.; Tam, W. Y.; Chan, C. T.; Sheng, P. *Physical Review Letters* **2000,** 84, (13), 2853-2856.
3. Zhang, W. Y.; Wang, Z. L.; Hu, A.; Ming, N. B. *Journal of Physics-Condensed Matter* **2000,** 12, (44), 9361-9370.
4. Bartlett, P. N.; Baumberg, J. J.; Coyle, S.; Abdelsalam, M. E. *Faraday Discussions* **2004,** 125, 117-132.
5. Fleming, J. G.; Lin, S. Y.; El-Kady, I.; Biswas, R.; Ho, K. M. *Nature* **2002,** 417, (6884), 52-55.
6. Deubel, M.; Von Freymann, G.; Wegener, M.; Pereira, S.; Busch, K.; Soukoulis, C. M. *Nature Materials* **2004,** 3, (7), 444-447.
7. Gratson, G. M.; Xu, M. J.; Lewis, J. A. *Nature* **2004,** 428, (6981), 386-386.
8. Lee, J. H.; Kim, C. H.; Ho, K. M.; Constant, K. *Advanced Materials* **2005,** 17, (20), 2481.
9. Lin, Y. K.; Rivera, D.; Chen, K. P. *Optics Express* **2006,** 14, (2), 887-892.
10. Lin, Y.; Herman, P. R.; Darmawikarta, K. *Applied Physics Letters* **2005,** 86, (7), 3.
11. Braun, P. V.; Wiltzius, P. *Nature* **1999,** 402, (6762), 603-604.
12. Nagpal, P.; Han, S. E.; Stein, A.; Norris, D. J. *Nano Letters* **2008,** 8, (10), 3238-3243.
13. Han, S. E.; Andreas, S.; Norris, D. J. *Physical Review Letters* **2007,** 99, (5), 053906.
14. Puscasu, I.; Pralle, M.; McNeal, M.; Daly, J.; Greenwald, A.; Johnson, E.; Biswas, R.; Ding, C. G. *Journal Of Applied Physics* **2005,** 98, (1), 013531.
15. Celanovic, I.; Jovanovic, N.; Kassakian, J. *Applied Physics Letters* **2008,** 92, (19).
16. Celanovic, I.; Perreault, D.; Kassakian, J. *Physical Review B* **2005,** 72, (7).
17. Teperik, T. V.; de Abajo, F. J. G.; Borisov, A. G.; Abdelsalam, M.; Bartlett, P. N.; Sugawara, Y.; Baumberg, J. J. *Nature Photonics* **2008,** 2, (5), 299-301.
18. Gaillot, D. P.; Summers, C. J. *Journal of Applied Physics* **2006,** 100, (11), 10.
19. Gao, H. W.; Henzie, J.; Lee, M. H.; Odom, T. W. *Proceedings of the National Academy of Sciences of the United States of America* **2008,** 105, (51), 20146-20151.
20. Bozhevolnyi, S. I.; Volkov, V. S.; Devaux, E.; Laluet, J. Y.; Ebbesen, T. W. *Nature* **2006,** 440, (7083), 508-511.
21. Boardman, A. D., *Electromagnetic Surface Modes*. Wiley, Chichester: 1982.

CHAPTER 4
HIGH QUALITY FACTOR METALLODIELECTRIC HYBRID PLASMONIC-PHOTONIC CRYSTALS

The work presented in this chapter was a collaboration with Lei Shi, Dr. Dezhuan Han and Professor Jian Zi from Fudan University at Shanghai, China

4.1 Introduction

Since the 1980s, when surface plasmons (SP) were first used to investigate chemistry at a metal surface,[1] SP based sensors have become an important tool for biological and chemical sensing[2]. The effectiveness of these sensors relies on two key points: the strong and selective binding of analyte to the sensor surface and the sensitivity of the optical response of the SP systems to changes in the local dielectric environment resulting from those binding events. As nano-fabrication technologies have advanced, SP-based phenomena on nano-structured metal surfaces have been actively studied[3-10], and the resolution limit has been constantly improved, currently reaching sub-molecular scale[11]. A major difficulty with these SP sensors comes from the lossy nature of their resonance modes, which is due to strong absorption of light by the metal nanostructures themselves. As a result, further sensitivity improvements become increasingly challenging[8]. On the other hand, enjoying very low absorption, pure dielectric material based optical sensors have achieved very high sensitivity due to their extremely high quality factor resonance modes[12]. However, fiber optics based systems are difficult to miniaturize[13] and most nano-structure based systems require complicated and precise fabrications[14]. Here we report a simple SP device based on self-assembly of a periodic dielectric structure on flat metal surface, a hybrid plasmonic crystal, which combines a SP system's high field localization and the dielectric photonic crystal's long propagation length and mode coupling capability. This system supports both plasmonic and optical resonance modes with Q factors one order of magnitude higher than typical nanostructured plasmonic systems[9]. We show that as a sensor, this device can achieve atomic layer resolution and a large linear dynamic range, without sophisticated nanopatterning or data processing[11].

4.2 Sample Fabrication

The hybrid plasmonic crystal described here consists of a close packed monolayer of polystyrene colloids self-assembled on a chemically modified gold surface. Figure 1b presents a top view SEM image and schematic diagrams of the device. Typically, the colloidal monolayer region covers an area of a few millimeters by one centimeter. See experimental for details. Samples composed of colloids ranging in diameter from 830 nm to 2.1 μm have been studied. However, majority of the work is done on a batch of 830 nm polystyrene particles.

4.3 Optical Property

A reflection spectrum taken at normal incidence with unpolarized light shows distinct features as reflection minima (Fig. 4.1a). For colloidal monolayer made of colloids with different diameter, the optical features linearly scale proportionally with colloid size (Fig 4.2). Each reflection minimum corresponds to the coupling of light into a unique surface propagation mode (or modes if degenerate) which subsequently is absorbed by the metal as the wave propagates on the metal surface. In this unique design, the colloidal monolayer here functions not only as the scattering element, but also as the guiding media of the wave, which contributes to long propagation length and resultant high Q factor. The peak near 793 nm, which has a full width half maximum (FWHM) of 6 nm (0.012 eV), achieves a Q factor (defined as Peak Frequency/FWHM in frequency) of 132. When the double peaks near 880 nm are decoupled, each of them has a Q factor near 100, as compared to below 20 in a typical SP system (Table 4.1)[8, 9, 15-19].

4.4 Propagation length of resonance modes extrapolated from Q factor

After interacting with a periodically patterned surface, light is coupled into surface propagation modes with $k_{sm}=k_0+nG_1+mG_2$, in which k_{sm}, k_0 are the wave vector of surface modes and the in-plane component of incident light. At normal incidence $k_0=0$. G1, G_2 are the two reciprocal lattice vector of the triangular lattice. n and m are two integers. From band structure analysis, we found that the four modes all follow the same characteristics, having wave-vector corresponds to smallest lattice vector when $k_0=0$. The wavelength of the surface mode can be calculated as $\lambda_{sm}=2\pi/ k_{sm}=719$nm. For the four modes SPM1, GM1, SPM2, GM2, FWHM are measured to be 3.73nm, 1.26nm, 2.62nm, 1.66nm according to RCWA simulation. Q (f_{max}/FWHM) of each mode is then calculated to be 278, 781, 340, 478. Q factor is related to energy flow of a resonance structure by the following relation:

$$Q = 2\pi \frac{E_{total}}{E_{dissipate}}$$

Where E_{total} and $E_{dissipate}$ are the total energy stored in the system and the energy dissipated in one period T. The intensity of a surface mode propagating in the plasmonic crystal follows this relation:

$$I = I_0 Exp(-r/\delta_{sm})$$

where δ_{sm} is the decay length. The total energy stored is

$$E_{total} = \int_{\substack{all \\ \mathrm{mod}\, e \\ volume}} I_0(\vec{r})d\vec{r}$$

After one period, a wave propagates a distance of λ_{sm}, and the intensity can be written as

$$I = I_0 Exp(-\lambda_{sm} / \delta_{sm})$$

The total energy dissipated in one period is

$$E_{dissipated} = [1 - Exp(-\lambda_{sm} / \delta_{sm})] \times \int_{\substack{all \\ \mathrm{mod}\,e \\ volume}} I_0(\vec{r}) d\vec{r} = \lambda_{sm} / \delta_{sm} \times \int_{\substack{all \\ \mathrm{mod}\,e \\ volume}} I_0(\vec{r}) d\vec{r}$$

In this case, loss comes from both absorption by the metal and the coupling back into the free space.

$$Q = 2\pi \frac{\delta_{sm}}{\lambda_{sm}}$$

$$\delta_{sm} = \frac{Q}{2\pi} \lambda_{sm}$$

By this means, δ_{sm} of the four modes (from SPM1 to GM2) are calculated to be 31.8, 89.4, 38.9, 54.7μm. A comparison between the propagation length of these resonance modes and that of surface Plasmon modes at flat gold surface can be found in table 4.2.

4.5 Optical Study with Computer Simulation

Because of the structural simplicity and periodic nature of the hybrid plasmonic crystal, rigorous coupled wave analysis (RCWA), a relatively low computational cost simulation technique, is applied to study the physics of the optical modes and to generate most of the simulation data shown here. Korringa Kohn Rostoker (KKR) method is also applied to obtain the band structure of the resonance system. (Fig. 4.3) At normal incidence, simulations show no difference between the two orthogonal polarizations. So, simulation results based on only one polarization (Fig. 4.1a) are shown here. The unit cell is shown as the dashed rectangle in the middle panel of figure 4.1b, and a periodic boundary condition is used. When a simple model of a colloidal monolayer on top of gold surface is simulated, the simulated spectrum has the right peak shapes. However, the positions of two of the peaks are off by 6 nm (Fig. 4.4). By shifting the center of spheres towards metal by 10 nm (~1%), a reasonable assumption given due to van der Waals and capillary forces which slightly flatten the contact point between the colloid and gold surface, an accurate match is reached between simulation and experiment (Fig. 4.1a). The much narrower peak widths and absence of a double-peak in the simulation as compared to the experimental spectra, is due to the exact perpendicular incidence condition assumed in the simulation. The experimental spectra were collected using a collection angle of 4°. The different dispersion relation of TE and TM modes causes the peaks to split and broaden (Fig. 4.3). The non-normal components also contribute to the minor spectrum features near 770nm and 1000nm. (A detailed analysis of the spectrum is provided in the next session.) Inevitable structural defects formed during self-assembly process also contribute to peak broadening.

At each absorption peak, the field intensity profile (Fig. 4.1c) is calculated and plotted as $|E|^2$ on a cross-sectional cut through the center of a colloid along the ΓM direction (Fig. 4.1b), as shown by the dashed red line in figure 4.1b. Incident light has an intensity of $|E|^2=1$. The four resonance modes have very different field distributions; the first and third modes counting from longest wavelength have the strongest field intensity at the metal interface, while the other two modes have fields concentrated within the colloids. We name the modes according to their main field distribution features sequentially from longer to shorter wavelengths. There are two surface plasmon modes (SPM1&2) and two guided modes (GM1&2). SPM2 and GM2 have nodes (zero intensity points) inside the sphere, similar to higher order modes in a slab dielectric waveguide[20]. They also have larger portions of their field intensity farther away from the metal surface and stronger hot spots on top of the spheres, as compared with their lower energy counterparts. As we will show, understanding the modal intensity distribution is essential to both understand and design a hybrid plasmonic sensor for maximum responsivity.

4.6 Detailed Analysis of Optical Spectrum

As can be seen, multiple optical features are clearly seen on the experimental obtained spectrum. The origin of each feature can be traced by a careful comparison with the band structure obtained by KKR method (Fig 4.3). All reflection measurements reported here are taken with a homebuilt CaF_2 objective with numerical aperture of 0.07, which corresponds to a half collection angle of 4 degrees. Simulation shown in figure 1a is based on normal incident light with electric field polarized along Γ-K' direction. Simulation captures the main features of the measurement. However, there are more details in measurement which require angular dependent simulation (band diagram, figure 4.3) to understand. The four panels correspond to two polarizations along 2 directions. Main features are listed as blue marks on the very left.

Starting from the longest wavelength, the first optical feature corresponds to the lowest band in both S and P polarization. The double peak here is caused by the difference between S and P polarization at angles away from normal incidence. The smaller peak near 1000nm corresponds to the 2nd band in P polarizations at small angles. Next, comes the main feature GM1, matching the 3rd band in P polarization and 2nd band in S polarizations. Away from normal direction, the S and P bands slowly move in opposite direction in wavelength, causing the peak to slightly broaden. Moving to shorter wavelength, there are a few merely noticeable features corresponds to the various bands in the band diagram. Next main feature is SPM2. Like SPM1 the double peak is caused by difference in P and S polarizations. The weaker lower branch in P polarization might result in the smaller features near 900nm. Moving to shorter wavelength, we crossed a few bands weak at small angles, resulting in weak features in the reflection spectrum. Then, comes the main feature GM2. It is noticed that in this case, both P and S polarizations have very small dispersion at small angles. That might contribute to the high Q factor of GM2. Moving further to shorter wavelength, one more band is crossed that generate a minor feature around 770nm.

4.7 Optical Response vs. Structure Evolution

To demonstrate the effect of field distribution, we coat our structure with alumina (n=1.57-1.59), by two methods with very different deposition patterns. (Fig 4.5) In the first method, physical vapor deposition (PVD), Al_2O_3 (n=1.57) is directionally deposited onto the structure along a direction perpendicular to the metal surface (Fig. 4.6a) and the reflectivity is measured for several coating thicknesses (Fig. 4.6c). The peak position of the four modes is plotted vs. coating thickness in figure 4.6a; the response appears to be quite linear and matches well with RCWA simulations. As expected, the magnitude of the peak shift is related to the modal intensity near the top of the colloidal particles, as this is where the PVD Al_2O_3 primarily grows. For the second deposition method, Al_2O_3 (n=1.59) is grown by atomic layer deposition (ALD), a technique which coats all accessible surfaces at same rate of roughly one monolayer per cycle (Fig. 4.6b). As expected, since ALD coats all the free surfaces of the colloids, larger peak shifts are observed for all optical modes for the same coating thickness vs. PVD Al_2O_3. Most significantly, the SPMs, which have field maxima just above the metal surface and outside the colloids, shift more than the GMs, which have a significant fraction of their modal intensity inside of the colloids. It is worth mentioning that under the ALD coating condition, the intensity of SPMs changes dramatically. The peak of SPM1 reduces in intensity and disappears between 25 nm and 42 nm of Al_2O_3 coating, while the peak intensity of SPM2 decreases first, reaching a minima at a coating thickness of ~25 nm, and then increases with increasing coating thickness. A new peak near 725 nm, corresponding to a third SPM, starts to appear. Interestingly, the evolution of peak height of SPM3 with coating thickness shows an opposite behavior compared with SPM2. Although the exact cause of non-monotonic changes in peak intensity requires further study, we believe it is related to the difference in field distribution of each resonance mode and the local refractive index change when coating material is gradually applied. The changes in coupling efficiency with coating morphology help to elucidate the unique physics of this system, and provide the possibility to accurately utilize the intensity evolution together with the peak shift as an indicator of the local dielectric environment for example in a biosensor application as has been shown by other authors[21].

4.8 Optical Sensitivity of the Sensor

4.8.1 Traditional Figure of Merit (FOM)

Different definitions have been used to characterize the sensitivity of SP sensors[2, 21-23]. Here we adopt a simple and widely accepted definition[8] based on a figure of merit (FOM) defined as

$$\mathrm{FOM} = \frac{\mathrm{Peak\ shift\ (eV)/FWHM\ (eV)}}{\Delta \mathrm{RIU}}$$

ΔRIU here refers to the bulk refractive index (RI) unit change of the environment surrounding the sample. However, because of the relatively small RI contrast between PS and common liquids such as ethanol or water, all optical features disappear when our sample is immersed in those liquids. Given the good match between RCWA simulation and experimental study in all studies shown above, we rely on RCWA to simulate the situation when our plasmonic optical sensor is surrounded by materials with RI ranging from 1.05 to 1.2 (Fig 4.7a). The result shows a linear relation between peak shift and ΔRIU for SPM modes and a non-linear relation for GMs, where higher refractive indices results in larger incremental changes in peak shift. Combining these results and the FWHM obtained from experiment, the FOM of GM2 is extrapolated to be larger than 37. When decoupled, the stronger peak in SPM2 has FOM=30. Both values are higher than most of the plasmonic sensors reported so far (see supplementary information for details). In the following study, we focus on GM2 due to its highest sensitivity.

4.8.2 Improved Figure of Merit

Although this definition of sensitivity has the merit of being simple and universal, it does not properly represent the real situation of surface based sensing, where the goal is generally to detect the adsorption of a thin layer of material on the sensor surface rather than the bulk environment. The difference lies in the fact that optical modes concentrated near the surface are more responsive to changes at the surface coating even though their response toward changes in the bulk RI change is what is described by the this FOM. With that in mind, we propose a modified empirical FOM2 that takes into account the film thickness.

$$\mathrm{FOM2} = \frac{\mathrm{FOM}}{\text{Coating thickness (nm)}} = \frac{\text{Peak shift (eV)/FWHM (eV)}}{\Delta\mathrm{RIU} \cdot \text{Coating thickness (nm)}}$$

ΔRIU here refers to the refractive index unit change between the coating material and air. When the response is nonlinear, the FOM2 is taken as the value for small coating thicknesses. How thick the coating layer can extend into the bulk before the linear relationship between the peak shift and coating thickness breaks down is defined as the linear dynamic range. Experimentally, FOM2 can be well characterized by measuring the peak shift vs. the ALD coating thickness. Along with the measurements based on alumina ALD, we also performed the same peak shift vs. ALD coating thickness measurement for hafnia (HfO_2), which has a refractive index of n=1.96.

(Fig. 4.8) All data points of GM2 from both Al_2O_3 and HfO_2 ALD experiments are plotted in figure 3b with numerator of FOM2 (the peak shift/FWHM) plotted on Y axis and denominator (the refractive index difference between the deposited material and air times the coating thickness) on X axis. Both data sets can be fit very well with a line of slope=FOM2=0.359 nm^{-1}, demonstrating the linear dynamic range of this sensor to the RI of both alumina and hafnia to be at least 57nm. Although the study here is based on inorganic materials with higher refractive index comparing with organic molecules in bio-sensing application, the linear relation obtain from two materials with very different refractive index not only convinced us that FOM2 is a generally applicable figure of merit, but also indicate that the result obtained here can be extrapolated to organic molecules by calculating with a lower refractive index. The linear dynamic range here is fundamentally limited by the geometry of the colloidal monolayer, and not any optical effect. A thicker ALD coating seals off the interstitial space among three adjacent spheres and thus blocks the pathway of the reactive gas, and thus from this point forward, material is only deposited on top of the spheres. Another benefit of the large linear dynamic range is that because of the inevitable fabrication non-uniformity, there is a 2-3 nm sample-to-sample fluctuation in peak positions for samples right after colloidal self-assembly. Since the linear dynamic range is much greater than the coating thickness required to move the peaks by a few nanometers, and such fluctuations can be easily compensated by using a thin ALD coating enabling batch-to-batch tuning of devices prior to use.

4.8.3 Detection Limit of the Sensor

A more straightforward way to evaluate the sensitivity of a sensor is to determine how small a change it can detect. The reflectivity of the sensor is measured after each Al_2O_3 ALD cycle from the 40th to 45th cycle. Another measurement is made at 50th cycle (Fig. 4.7c). In cycles 40 to 45, where the sample is removed from the chamber after each cycle, ~1.5 Å is deposited per cycle, while between cycles 46-50, where the sample remains in the deposition chamber, ~1 Å of material is deposited per cycle; see experimental details for additional information. The peak shift of GM2 is plotted as a function of ALD cycle number; the error bar is the resolution of the spectrometer. The inset shows the normalized reflection spectrum (0 to 1 scale) after the 40th, 41st, 45th and 50th cycle. A clear difference can be observed between 40th and 41st cycle. From our calculations, this sensitivity is sufficient for example to detect the difference in layer thickness of one CH_2 group in a self-assembled monolayer.

4.9 Sensing Application

For real applications, this sensor can function in two situations. If analyte is in the solution phase, sensor will be dipped in the solution to facilitate analyte bonding followed by rinsing step to watch away the physisorbed molecules. If the analyte is in gas phase, or airborne, this sensor can be applied directly. We further demonstrate the gas phase sensing capability of this optical sensor by detecting the physisorption of ethanol on the sample surface. Argon gas is bubbled through an ethanol filled bubbler held at room temperature and the resulting gas is measured to contain ethanol with partial pressure of 4.5 kPa, which is 58% of the saturated ethanol partial pressure at room temperature. At equilibrium, the ethanol in the vapor forms a thin physisorbed layer, with refractive index close to that of bulk ethanol (1.36), on all exposed surface of the sensor. We alternately introduce dry argon and this ethanol containing argon into the chamber while the sample is held at each of the three different temperatures: 25, 40, and 55 °C. At the same time, the optical response of the sample is monitored. We found that the peak positions of the optical features followed the gas environment closely (Fig. 4.9). By measuring the peak shift of GM2, the amount of ethanol physisorbed on the surface can be determined.

Using the FOM2 obtained above, and assuming the physisorbed layer has a RI equal to that of bulk ethanol (1.36), the ethanol coating thickness is 10.6, 4.4, and 2.8 nm at 25, 40, and 55 °C, respectively. These results are confirmed by measuring the physisorption of ethanol on a flat polystyrene film with ellipsometry under similar conditions. In this case, Polystyrene solution of the same batch is dried and dissolved in toluene to make a 1% solution. The solution is then filtered through a 0.45µm PTFE filter and spin coated on silicon wafer and 1500RPM for 60S. Silicon wafer is pretreated in a boiling solution of 3:1 ratio of sulfuric acid and 30% hydrogen peroxide. The resulted polystyrene film has a thickness of 38.6nm measured by ellipsometry. The film is then treated with UV ozone for 4 minutes, same as the process the plasmonic crystal goes through. The thickness is reduced to 33.4nm. A special optical window is made to fit on the Linkam THMS600 heating stage to match the 70 degree incident angle. By introducing ethanol containing argon into the chamber and controlling the sample temperature, the resulting ethanol coating thickness is listed in table 4.3. The absolute value of coating thickness is within 20% of the result obtained from measuring the plasmonic crystal. The ratio of the coating thickness at 3 different temperatures is within 10%. Given the fact that physisorption is largely determined by surface of the polystyrene, the difference here is within the fluctuation range.

4.10 Conclusion

In conclusion, the simple hybrid plasmonic crystal based on a colloidal monolayer on a flat gold surface demonstrated here shows rich and unique physics, and exhibits an exceptionally high sensitivity. It requires only a simple detection apparatus, is straightforward to simulate and is tolerant to the imperfections of self-assembly. The SPMs of this design unifies the long propagation nature of dielectric waveguides and the highly localized field effect of surface plasmons. , where a significant portion of energy is concentrated near the metal surface and the propagation length calculated from the Q factor still approaches the propagation length of surface plasmons at a planar gold-air interface (see supplementary information table 2). GMs, on the other hand, have the majority of the energy concentrated in the dielectric layer away from the metal surface, which makes it ideal for applications such as surface enhanced fluorescence[24] where quenching needs to be avoided. Along with sensing applications, the high Q resonances of both the GMs and SPMs make this concept a strong candidate for applications including surface emitting lasers[25, 26] and narrow band optical filters[4].

4.11 Experimental

Experiment: The substrate was prepared by evaporating 100 nm of gold on a 700 μm thick silicon wafer with 5 nm of chromium as an adhesion layer. It was then soaked in a 20 mM 3-mercapto-1-propanesulfonic acid, sodium salt (HS-$(CH_2)_3$-SO_3Na) water solution for overnight, forming a monolayer of hydrophilic molecules on the gold surface. Sulfate-terminated PS spheres (Molecular Probes) of various diameters were formed into opal films on this substrate via evaporative deposition at 50~55 °C with a colloid volume concentration of 0.05~0.2% in water. Atomic layer deposition is performed in commercial ALD equipment (Cambridge NanoTech Inc.) at 80 °C with trimethylaluminum (for Al_2O_3)/ tetrakis (dimethylamido) hafnium(IV) (for HfO_2) and water as precursors. When the sample remains in the ALD chamber between cycles the growth rate is very consistent for both hafnia and alumina. However, when the sample is exposed to the laboratory environment, such as when the peak shift was measured per ALD cycle, the thickness of layer deposited (Al_2O_3 and possibly molecular contaminants) is slightly greater. Physical vapor deposition is done by E-beam evaporation (FC-1800, Temescal) at a rate of 1 Å/S. The dielectric films of various materials by different deposition methods reported here are also deposited on bare silicon substrates under the same condition. Their coating rate, thickness, and refractive indices are measured by ellipsometry (VASE, J.A. Woollam Co. Inc.) using the Cauchy model. The RI of polystyrene is measured by dissolving the PS spheres in toluene followed by spin coating of this solution on a silicon wafer. Reflection spectra are measured by Bruker vertex 70 FTIR coupled with a Hyperion 1000 microscope. A CaF_2 objective (2.4X, NA= 0.07) was used for all measurements. The spot size is ~300 μm. In the ethanol sensing experiment, the hybrid plasmonic crystal, pretreated with UV ozone for 4 minutes to activate the surface, is heated in a microscope compatible button heating chamber (Linkam THMS600) with CaF_2 window. Either dry argon or ethanol containing argon is introduced to the chamber. Ethanol containing argon is made by running argon through an ethanol bubbler. The ethanol vapor partial pressure is calculated by measuring the weight loss of the liquid over the time of the experiment. Experiments are performed at 3 different temperatures, 25, 40, 55 °C as shown in figure 4. One reflectance spectrum is measured every 3 minutes.

Simulation: All simulations use measured refractive indices for the dielectric materials and the Drude model for gold with $\omega_{sp} = 1.236\times10^{16}\,\text{rad/S}\;\; \gamma = 1.3\times10^{14}\,\text{rad/S}$, which gives dielectric constants that match well with experimental parameters[27]. We modified the existing KKR[28] code to simulate the PS sphere monolayer on flat gold surface. Commercial software is used for RCWA (DiffractMOD, RSoft Design Group). The grid size is automatically selected by the software to be ~5nm.

4.12 Tables

Table 4.1 Q factor and Figure of merit (if applicable) of typical nano-structure based optical systems (sensors) measured from published results. Q factor is defined as: Center of the peak(eV)/FWHM(eV) FOM is defined as: Peak shift(eV)/FWHM(eV)/ΔRIU. Result of our hybrid plasmonic crystal optical sensor is listed at the end as a comparison.

Description	Q factor	FOM	Reference
Individual Nanostructure based			
Dielectric core–metallic shell nanorice	2.5		Wang, H., Brandl, D. W., Le, F., Nordlander, P. & Halas, N. J. Nanorice: A hybrid plasmonic nanostructure. *Nano Lett* **6,** 827-832 (2006).
Nanoparticle with Silica core and gold shell of various thickness	<3.5		Loo, C. *et al.* Nanoshell-enabled photonics-based imaging and therapy of cancer. *Technol. Cancer Res. Treat.* **3,** 33-40 (2004).
Gold nanocage	4		Hu, M. *et al.* Ultrafast laser studies of the photothermal properties of gold nanocages. *J. Phys. Chem. B* **110,** 1520-1524 (2006).
Gold nanorods of various aspect ratio	<5		Murphy, C. J. *et al.* Anisotropic metal nanoparticles: Synthesis, assembly, and optical applications. *J. Phys. Chem. B* **109,** 13857-13870 (2005).
Individual holes on gold film	6.5	0.9	Rindzevicius, T. *et al.* Plasmonic sensing characteristics of single nanometric holes. *Nano Lett* **5,** 2335-2339 (2005).
Gold nanodisks and nanorings	<9.4		Aizpurua, J. *et al.* Optical properties of gold nanorings. *Phys. Rev. Lett.* **90,** 4 (2003).
Single silver nanoparticle	12.7	4.2	McFarland, A. D. & Van Duyne, R. P. Single silver nanoparticles as real-time optical sensors with zeptomole sensitivity. *Nano Lett* **3,** 1057-1062 (2003).

Table 4.1 (cont.)

Periodical nanostructure based			
Triangular metal island array	6		Haynes, C. L. & Van Duyne, R. P. Nanosphere lithography: A versatile nanofabrication tool for studies of size-dependent nanoparticle optics. *J. Phys. Chem. B* **105,** 5599-5611 (2001).
Uniformly oriented plasmonic particle arrays made by nanoimprint lithography	6		Lucas, B. D., Kim, J. S., Chin, C. & Guo, L. J. Nanoimprint lithography based approach for the fabrication of large-area, uniformly oriented plasmonic arrays. *Adv. Mater.* **20,** 1129-1134 (2008).
3D plasmon crystal with nanoimprint lithography	~13		Stewart, M. E. *et al.* Quantitative multispectral biosensing and 1D imaging using quasi-3D plasmonic crystals. *Proc. Natl. Acad. Sci. U. S. A.* **103,** 17143-17148 (2006).
Silver film over nanowells	16.8	14.5	Hicks, E. M. *et al.* Plasmonic properties of film over nanowell surfaces fabricated by nanosphere lithography. *J. Phys. Chem. B* **109,** 22351-22358 (2005).
sub-wavelength hole arrays on metal film	27.5		Ebbesen, T. W., Lezec, H. J., Ghaemi, H. F., Thio, T. & Wolff, P. A. Extraordinary optical transmission through sub-wavelength hole arrays. *Nature* **391,** 667-669 (1998).
Multiscale hole arrays on gold film	47.6	23.3	Henzie, J., Lee, M. H. & Odom, T. W. Multiscale patterning of plasmonic metamaterials. *Nat. Nanotechnol.* **2,** 549-554 (2007).
Our Hybrid plasmonic-photonic structure	132	>37(GM) 30(SPM)	

Table 4.2 Propagation Length Comparison

Mode	Wavelength(nm)	δ of plasmonic crystal (μm)	δ of gold air interface (μm)	δ of polystyrene (n=1.6) interface (μm)
SPM1	1035	31.8	97.8	22.6
GM1	984	89.4	87.8	20.2
SPM2	890	38.9	70.5	16.0
GM2	793	54.7	54.3	12.0

Table 4.3 Ethanol physisorption measured by optical/plasmonic sensor and ellipsometry

Temperature	25 ℃	40 ℃	55 ℃
GM2 peak shift (nm)	8.27	3.43	2.18
Coating thickness (nm)	10.6	4.41	2.80
Ratio	1	0.416	0.206
Ellipsometry measured thickness (nm)	8.49	3.42	1.55
Ratio	1	0.403	0.183

4.13 Figures

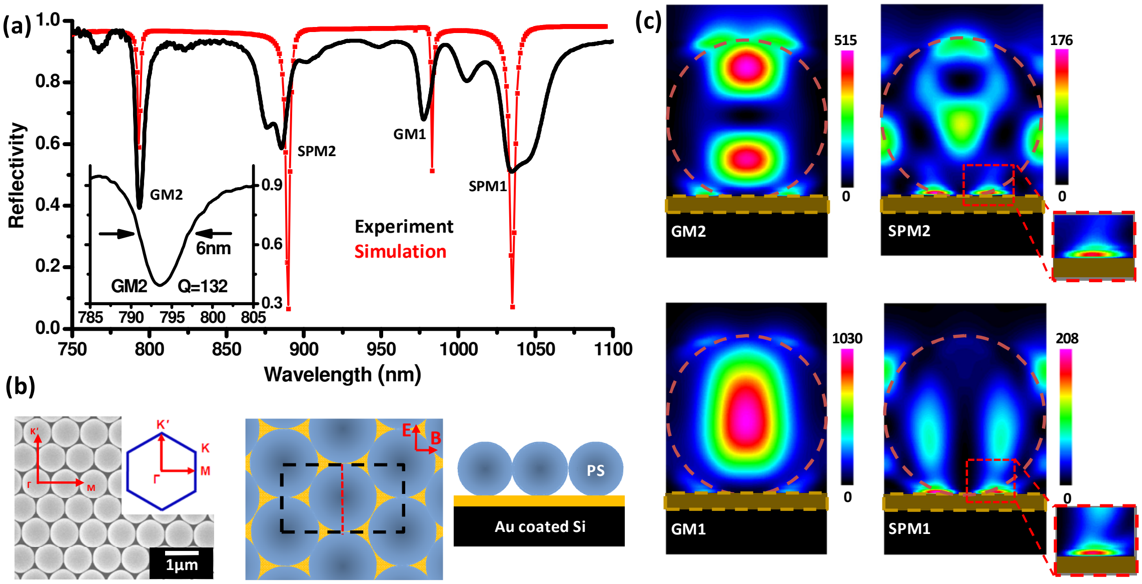

Figure 4.1. a) Reflection spectrum of a hybrid plasmonic crystal structure showing good match between experiment (black trace) and RCWA simulation (red trace). A detailed spectrum (experiment) of GM2 is shown in the inset. b) From left to right, top view SEM image, top view and side view schematics of the plasmonic crystal. The dashed rectangle shows the unit cell chosen in simulation. The red dashed line is the cross-section on which field maps are shown in (c). The polarization of incident light is shown as red arrows. c) E^2 map of four resonance modes. Color maps are in linear scale as shown along each panel. Incident light has $E^2 = 1$ in all cases. Dashed circles outline the perimeter of the colloids and the expanded insets are of the high field region adjacent to the substrate. The gold film is shown as the semi-transparent yellow rectangle.

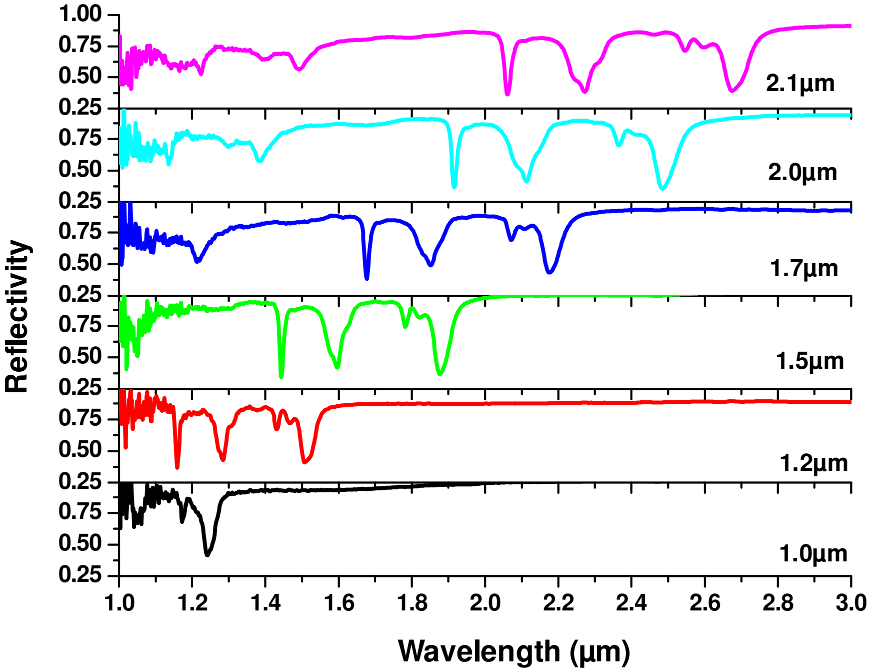

Figure 4.2 Reflection spectra of plasmonic crystal made from different colloid size. The same features are shown on all 6 spectra, the location of features scales proportional to the particle size.

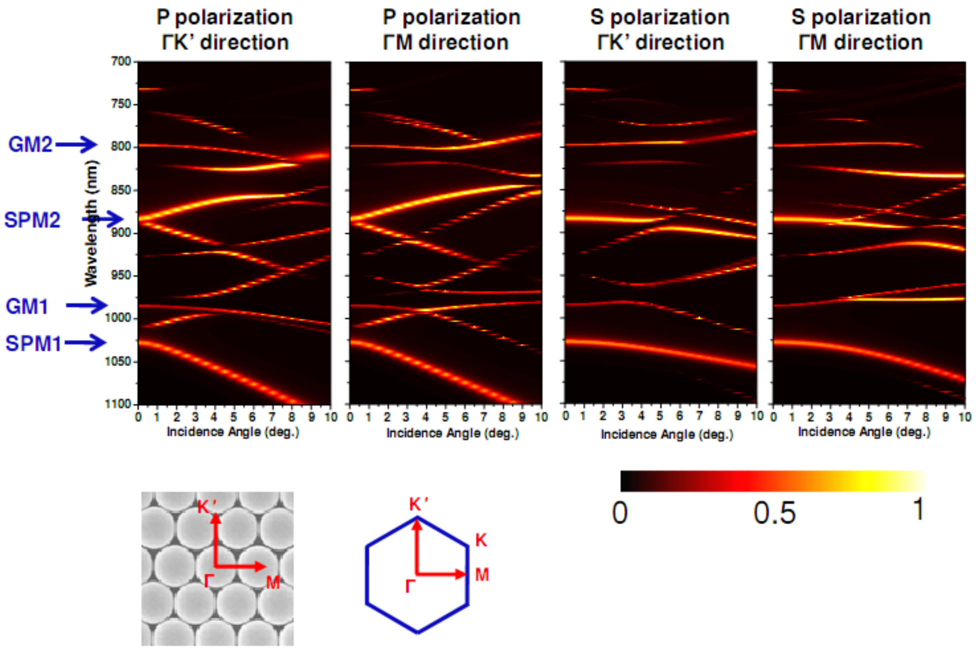

Figure 4.3 Band diagram of plasmonic crystal based on KKR methods. The structure being simulated is a 830nm PS colloidal monolayer on flat gold surface with point contact. Two characteristic incidence directions (lower panel) and polarizations are plotted as wavelength (nm) vs. incidence angle (degrees) for easier comparison with other results. The color maps show absorption on 0 to 1 scale. Four peaks are labeled on the left. It can be clearly seen that in the case of SPM1 and SPM2, P and S polarizations separate beyond 0 degree. That is the source of double peaks in the experimental reflectance spectrum.

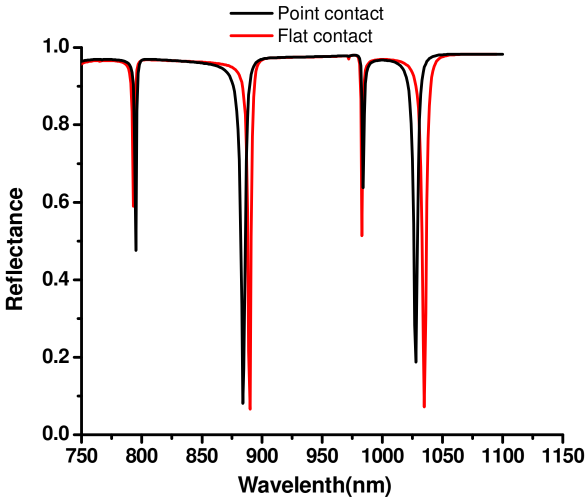

Figure 4.4 Reflection spectra of two slightly different structures based on RCWA simulation. Black trace represents the 830nm colloidal monolayer on gold with point contact. Red trace represents the structure with colloids shift 10nm towards the gold surface to form a flat surface contact. This change red shifts the SPMs can does not affect GMs as is expected from field distribution.

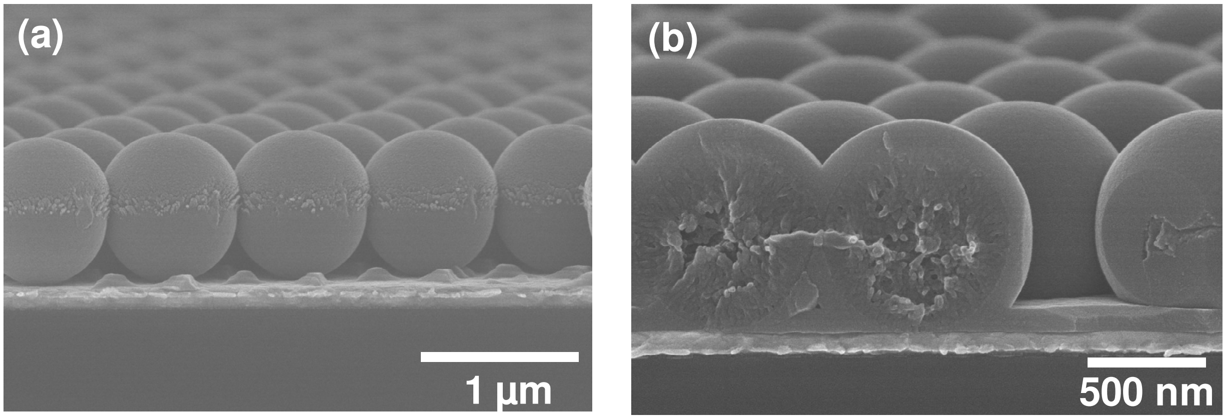

Figure 4.5 Cross-section SEM images of optical sensor after dielectric material coating by different methods. (a) After Al2O3 coating by physical vapor deposition (PVD), alumina deposit on the sensor in a directional way. (b) After Al2O3 coating by atomic layer deposition (ALD), alumina deposit on all exposed surface with uniform thickness.

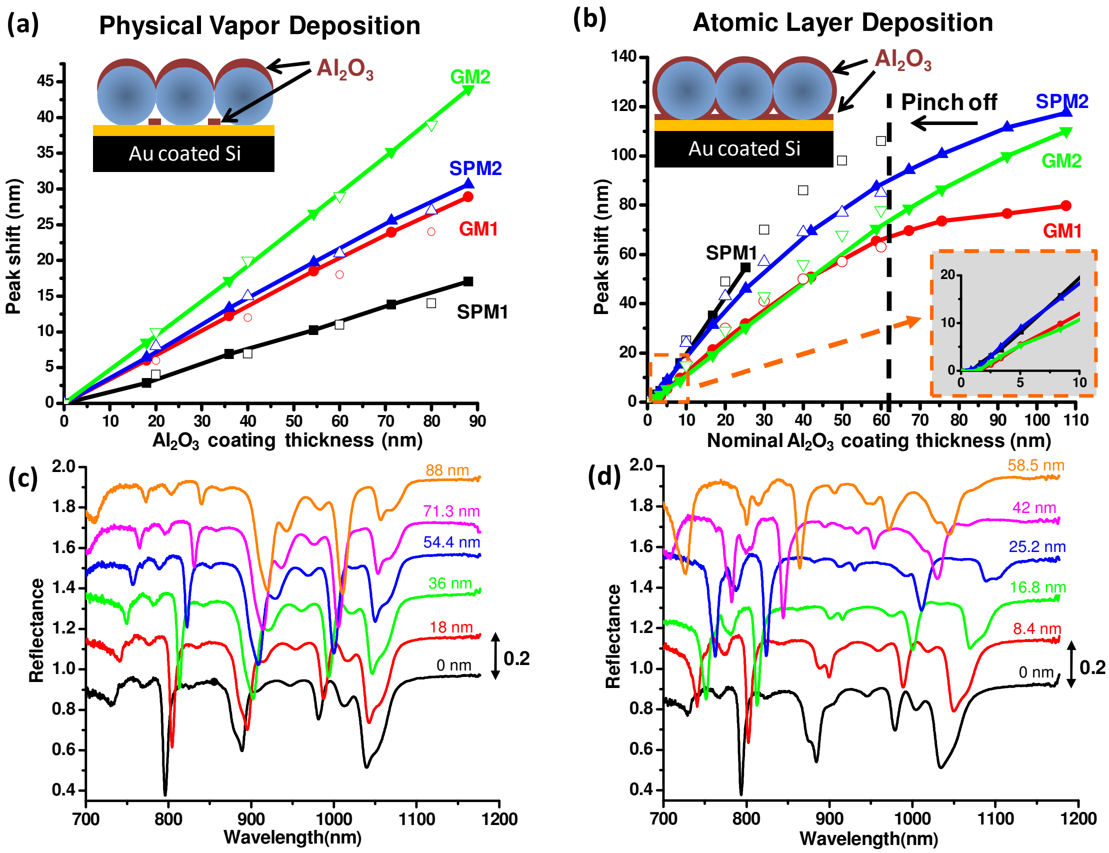

Figure 4.6. Reflection spectra peak shift as a function of Al2O3 coating thickness, both experiment (solid symbols, solid line as a guide to the eye) and simulation (open symbols), in the case of a) PVD and b) ALD. Insets illustrate the difference in coating geometry. The inset with gray background in (b) expands the optical response at initial growth steps. Because of the hydrophobicity of the surfaces, the growth rate for the first 20 cycles is much slower than in later cycles. The film thickness shown on x-axis however assumes each cycle deposits 0.8Å, and thus is a nominal thickness. This deposition rate is obtained by ellipsometric studies on thick Al2O3 coatings (20 to 40 nm) deposited on bare silicon wafers under the same condition. In ALD, the interstitial space between 3 adjacent colloids is completely sealed (pinch off) at a coating thickness of about 62nm, shown as a dashed line. Reflection spectrum evolution as the coating thickness increases for c) PVD and d) ALD. Traces are offset by 0.2.

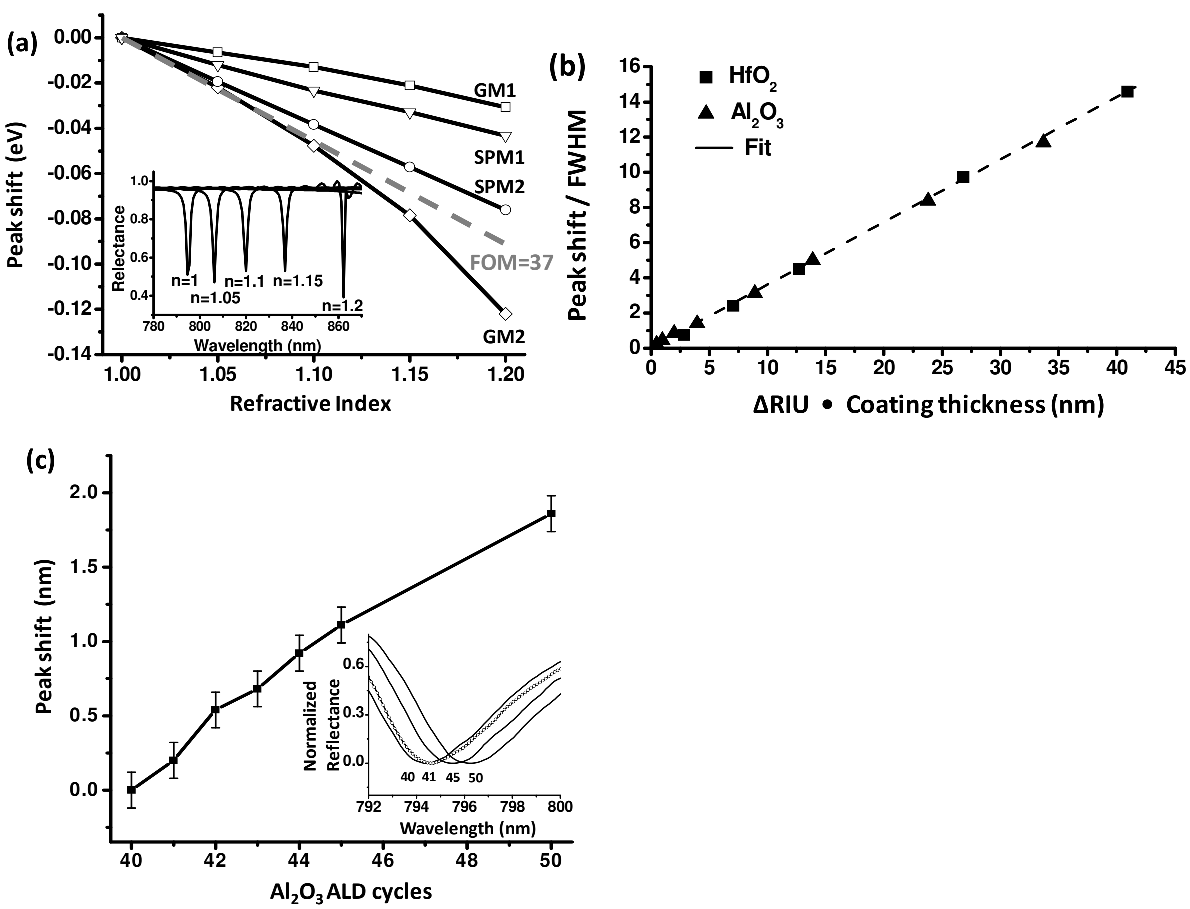

Figure 4.7. a) Absorption peak shift of the four resonance modes vs. environment refractive indices based on RCWA approximation. FOM of GM2 is extrapolated to be 37 by the initial slope. Inset shows the reflection spectrum of GM2 at different environmental refractive indices. b) Peakshift(ev)/FWHM(ev) as a function of refractive index unit change (ΔRIU) times coating thickness (nm) for the GM2 mode. The slope is the FOM2 proposed in the text. Data taken from AL2O3 and HfO2 ALD is shown as triangles and squares, respectively. All data falls on a straight line with a slope of 0.359 nm-1, demonstrating good linear dynamic range in both refractive index and film thickness. c) Peak shift (nm) of GM2 as a function of number of ALD cycles. The lines connecting the data points are guides to the eye. The error bar is the spectrometer resolution. The inset is the normalized reflection spectrum of GM2 for an increasing number of ALD cycles. The four traces correspond to 40, 41 (shown as a dashed line for clarity), 45 and 50 cycles. There is a clear peak shift from 40 to 41 cycles.

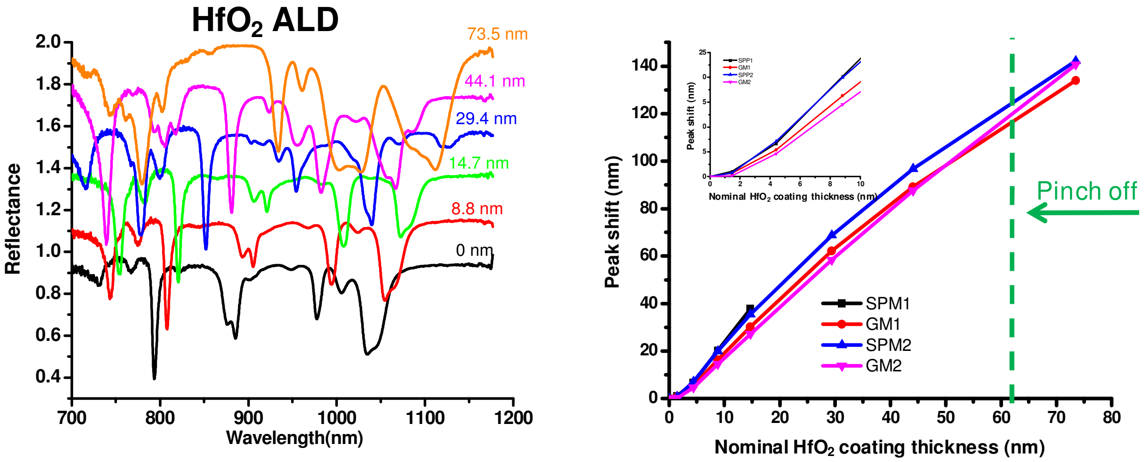

Figure 4.8 Optical response vs HfO_2 atomic layer deposition thickness. a) Reflection spectrum evolution as HfO_2 coating thickness increases. Each spectrum is offset by 0.2. Comparing with the case of Al_2O_3 ALD of the same coating thickness, the peaks shift faster, and the intensity evolution remains similar. b) Peak shift as a function of coating thickness. Due to hydrophobicity of the polystyrene surface, the initial growth rate for the first 20 cycles is slower, shown in the inset.

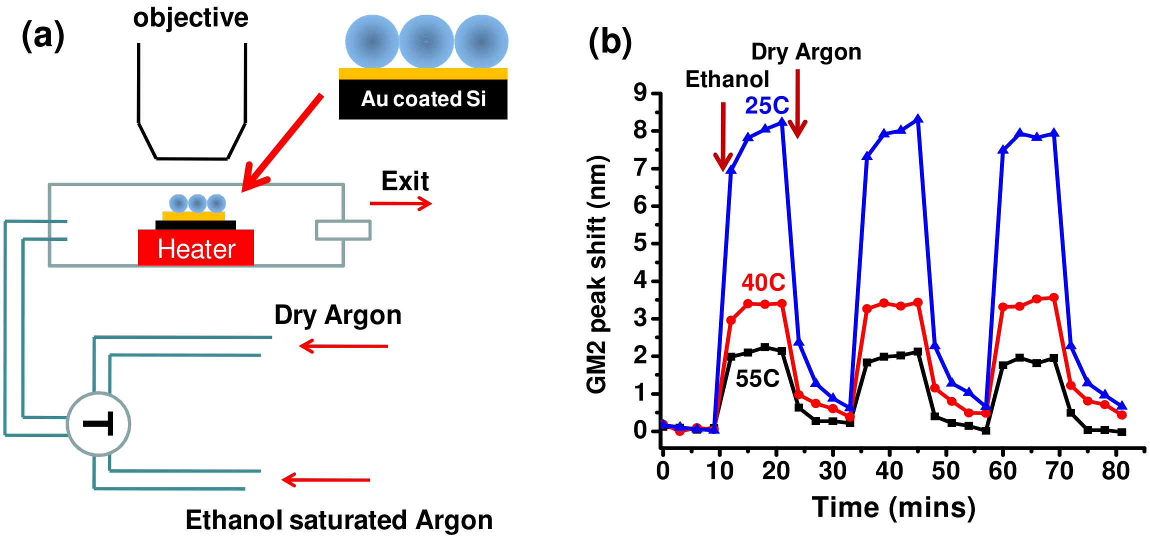

Figure 4.9 (a) Experimental setup of ethanol sensing. (b) GM2 peak shift from the dry argon state as the atmosphere cycles between dry argon and ethanol saturated argon at 25, 40, and 55 °C. The peak position closely follows the gas environment.

4.14 Reference

1. Gordon, J. G.; Ernst, S. *Surface Science* **1980,** 101, (1-3), 499-506.
2. Homola, J.; Yee, S. S.; Gauglitz, G. *Sensors and Actuators B-Chemical* **1999,** 54, (1-2), 3-15.
3. Kitson, S. C.; Barnes, W. L.; Sambles, J. R. *Phys. Rev. Lett.* **1996,** 77, (13), 2670-2673.
4. Ebbesen, T. W.; Lezec, H. J.; Ghaemi, H. F.; Thio, T.; Wolff, P. A. *Nature* **1998,** 391, (6668), 667-669.
5. Haynes, C. L.; Van Duyne, R. P. *Journal of Physical Chemistry B* **2001,** 105, (24), 5599-5611.
6. Henzie, J.; Lee, M. H.; Odom, T. W. *Nature Nanotechnology* **2007,** 2, (9), 549-554.
7. Lucas, B. D.; Kim, J. S.; Chin, C.; Guo, L. J. *Advanced Materials* **2008,** 20, (6), 1129-1134.
8. Anker, J. N.; Hall, W. P.; Lyandres, O.; Shah, N. C.; Zhao, J.; Van Duyne, R. P. *Nature Materials* **2008,** 7, (6), 442-453.
9. Stewart, M. E.; Anderton, C. R.; Thompson, L. B.; Maria, J.; Gray, S. K.; Rogers, J. A.; Nuzzo, R. G. *Chemical Reviews* **2008,** 108, (2), 494-521.
10. Linn, N. C.; Sun, C. H.; Arya, A.; Jiang, P.; Jiang, B. *Nanotechnology* **2009,** 20, (22), 225303.
11. Yao, J. M.; Stewart, M. E.; Maria, J.; Lee, T. W.; Gray, S. K.; Rogers, J. A.; Nuzzo, R. G. *Angewandte Chemie-International Edition* **2008,** 47, (27), 5013-5017.
12. Rao, Y. J. *Optics and Lasers in Engineering* **1999,** 31, (4), 297-324.
13. Ronot, C.; Archenault, M.; Gagnaire, H.; Goure, J. P.; Jaffrezicrenault, N.; Pichery, T. *Sensors and Actuators B-Chemical* **1993,** 11, (1-3), 375-381.
14. Block, I. D.; Chan, L. L.; Cunningham, B. T. *Microelectronic Engineering* **2007,** 84, (4), 603-608.
15. Hu, M.; Petrova, H.; Chen, J. Y.; McLellan, J. M.; Siekkinen, A. R.; Marquez, M.; Li, X. D.; Xia, Y. N.; Hartland, G. V. *Journal of Physical Chemistry B* **2006,** 110, (4), 1520-1524.
16. Wang, H.; Brandl, D. W.; Le, F.; Nordlander, P.; Halas, N. J. *Nano Letters* **2006,** 6, (4), 827-832.
17. Homola, J. *Analytical and Bioanalytical Chemistry* **2003,** 377, (3), 528-539.
18. Lu, Y.; Liu, G. L.; Kim, J.; Mejia, Y. X.; Lee, L. P. *Nano Letters* **2005,** 5, (1), 119-124.
19. Aizpurua, J.; Hanarp, P.; Sutherland, D. S.; Kall, M.; Bryant, G. W.; de Abajo, F. J. G. *Physical Review Letters* **2003,** 90, (5), 4.
20. Yariv, A.; Yeh, P., Guided Waves in Dielectric Slabs and Fibers. In *Photonics*, 6th ed.; Oxford Univ. Press: Oxford, 2007.
21. Stewart, M. E.; Mack, N. H.; Malyarchuk, V.; Soares, J.; Lee, T. W.; Gray, S. K.; Nuzzo, R. G.; Rogers, J. A. *Proceedings of the National Academy of Sciences of the United States of America* **2006,** 103, (46), 17143-17148.
22. McFarland, A. D.; Van Duyne, R. P. *Nano Letters* **2003,** 3, (8), 1057-1062.

23. Rindzevicius, T.; Alaverdyan, Y.; Dahlin, A.; Hook, F.; Sutherland, D. S.; Kall, M. *Nano Letters* **2005,** 5, (11), 2335-2339.
24. Liebermann, T.; Knoll, W. *Colloids and Surfaces a-Physicochemical and Engineering Aspects* **2000,** 171, (1-3), 115-130.
25. Tredicucci, A.; Gmachl, C.; Capasso, F.; Hutchinson, A. L.; Sivco, D. L.; Cho, A. Y. *Applied Physics Letters* **2000,** 76, (16), 2164-2166.
26. Tropper, A. C.; Foreman, H. D.; Garnache, A.; Wilcox, K. G.; Hoogland, S. H. *Journal of Physics D-Applied Physics* **2004,** 37, (9), R75-R85.
27. Johnson, P. B.; Christy, R. W. *Physical Review B* **1972,** 6, (12), 4370-4379.
28. Stefanou, N.; Yannopapas, V.; Modinos, A. *Computer Physics Communications* **1998,** 113, (1), 49-77.

CHAPTER 5

TEMPLATE ASSISTED THREE-DIMENSIONAL NANOLITHOGRAPHY VIA GEOMETRICALLY IRREVERSIBLE PROCESSING

(Adapted in part from Xindi Yu et al, Nano Letters 2007)

The work presented in this chapter was a collaboration with Dr. Huigang Zhang

5.1 Introduction

In recent years, considerable efforts have gone into combining conventional top-down nanofabrication and self-assembly based bottom-up methods to generate a diversity of complex nanostructures.[1-3] For example, through nanosphere lithography, a process that uses a colloidal monolayer as a deposition or etch mask, a variety of innovative 2-D nanostructures including triangles, rings, dots, and honeycomb structures have been generated.[4] However, the resulting patterns are generally limited to two dimensional structures of certain specific symmetries. Here we present a three dimensional template assisted nano fabrication technique that uniformly generates metallic and ceramic nanostructures throughout self-assembled colloidal templates. This method allows us to position the nanostructured objects at specific locations within the template, forming highly periodic multicomponent composite structures. Dissolving the template releases large quantities of unique shaped particles. Because the nanostructures are produced throughout the 3D template, much higher quantities particles are generated than for a 2-D fabrication process. In particular, ring shaped particles have attracted considerable attention because of their unique plasmonic,[5] optical[6] and magnetic properties[7] depending on the choice of materials. 2D based colloidal lithography has been a very popular method to generate particles of this kind.[4] However, each colloid in the colloidal monolayer only generates one ring particle, greatly limiting the quantities of particles generated per unit area. The advantages of a 3D lithographic approach are obvious, since all the colloids in the 3D colloidal crystal are utilized and each colloid generates 6 ring particles. As a result, particle areal density is increased by two orders of magnitude over a monolayer process.

5.2 Concept

The method proposed here takes advantage of the fact that conformal etching is not the geometric reverse of conformal growth at locations with negative surface curvature. A simple 2D representation illustrating this is shown in Figure 5.1. When the conformal coating thickness exceeds the minimum radius of the negative curvature, shown at point A in figure 1, the growth front along the normal direction moves faster than the rate of conformal coating. However, conformal etching propagates at the same rate along all directions. As a result, when the etching thickness equals the coating thickness, some coating material is left in the area originally having negative surface curvature.

5.3 Ring Particle Fabrication

3D colloidal crystals composed of close packed silica or polymer spheres are good examples of structures abundant of negative curvatures at the contact point of each pair of spheres. Using these as templates, nanoring particles can be fabricated as illustrated in figure 5.2. First a smooth film of tungsten with uniform thickness is coated onto a 3D silica colloid template through a static chemical vapor deposition (CVD) process (Fig. 5.2b).[8] Then, the tungsten coated sample is anodized in a sulfuric acid solution, converting roughly 10 nm of the surface of the tungsten to tungsten oxide.[9] The oxide layer is etched away in a potassium hydroxide solution. This process of anodization followed by chemical etching is repeated multiple times until the tungsten coated on the surface of the spheres other than the contact region is completely etched way, resulting in tungsten rings at the contact points between spheres (Fig. 5.2c). It is worthwhile to point out that for this specific system, the tungsten coating layer functions as the conductive pathway in the anodization step. Once a tungsten ring is electrically disconnected from the substrate, it is no longer etched. This makes the anodization a self-limiting process. As a result, even if the anodization is not completely uniform through the thickness of the template, the resulting tungsten rings are still quite monodispersed. After etching of the colloids in a dilute hydrofluoric acid (HF) solution followed by a washing and centrifugation step, the tungsten nanoring particles can be harvested (Figure 5.2d). A distinct advantage of this nanoring fabrication process is that it does not require a perfect colloidal crystal template, since the rings are only formed at each colloid pair contact point. So, even a randomly packed colloidal film can be used (figure 5.3). Electron diffraction (figure 5.4) indicates the rings are amorphous as expected for the CVD process utilized. The same principle can be applied to any material as long as the conformal coating and etching process exist which are compatible with the template being used. Aluminum oxide rings are generated by coating polystyrene colloidal crystal with Al_2O_3 through atomic layer deposition (ALD) followed by a slow HF etching (bottom SEM images of figure 5.2c,d) (See chapter 5.7 for details).

5.4 Geometry of the Ring Particles

The dimension of the rings generated can be easily calculated by simple geometry. **R** is the radius of the colloidal spheres; **x** is the thickness of the conformal coating layer and also the conformal etching layer (assuming they are equal); **r** and **h** are the radius and thickness of the ring particle.

$$r = \sqrt{x^2 + 2xR} - x \sim \sqrt{2xR} - x$$

$$h = \frac{2xR}{x + R} \sim 2x$$

The approximation is valid when **x**«**R** (in real case, x/R is <0.15 due to geometrical constraints). Since both **x** and **R** can be independently selected, the radius and the thickness of the ring particles can be independently controlled as shown in the figure 5.5a,b, where tungsten films of two different thickness, 60 nm and 40 nm, respectively, are coated on colloidal template grown using 1.58 µm diameter colloids. The thicker coating generates rings of greater thickness, 132 nm vs. 93 nm, and diameter, 640 nm vs. 454 nm. When colloidal templates of different sizes, 1.58 µm vs. 920 nm, are coated with tungsten with the same thickness (40nm), the radii of the final ring particles vary, 454 nm vs. 328 nm, while the thicknesses are kept roughly the same, 93 nm vs. 89 nm (figure 5.5b,c). By scaling the colloid size and coating thickness together, ring particles of different sizes but similar in aspect ratio are generated (figure 5.5a,d). Detailed dimensions of tungsten particle in each case are listed in table 5.1. SEM images of released ring particles fabricated from templates of different colloid sizes are shown in figure 5.7. The ability to independently modulate the dimensions of the resulting nanoparticles could be advantageous for numerous applications.

5.5 Optics of Metallodielectric Photonic Crystal

Along with providing a relatively high volume nanostructure fabrication process, this 3D lithography method results in a unique metallodielectric photonic crystal consisting of disconnected metallic elements supported by a dielectric structure. Popular methods for generating 3D metallodielectric photonic crystal involve the use of templates formed by colloidal self-assembly,[10] interference lithography[11, 12] or direct writing[13, 14] which are filled with a metal by conformal coating,[15] nanoparticle infilling,[16, 17] or electrodeposition.[18] The result is a connected metallic structure in which electric fields are conductively coupled. 3D optical metamaterials based on resonant structures require discrete capacitively coupled metal elements to be positioned inside a 3D matrix with accurate control over their position, geometry and orientation.[19, 20] In those cases, conductive coupling of the metallic elements is undesirable. The ability to position disconnected metallic elements in 3D space using a colloidal crystal template and our template assisted three-dimensional nanolithography process is demonstrated for the case of tungsten rings generated in a 3D silica colloidal crystal (figure 5.8a). Here, the disconnected tungsten rings form a periodic structure corresponding to Wyckoff notation 24d of space group Fm-3m with the ring axis normal to the colloid surface. The reflection and transmission spectra of the template (figure 5.8b) and the metallodielectric photonic crystal after all processing steps (figure 5.8c) are measured. Strong absorption is observed around 2.5 µm, while a pass band at long wavelengths is indicative of the discrete nature of the metal elements. The dependence of optical response to the number of layers is studied by measuring reflection and transmission spectrum at regions of different thickness over the same sample (figure 5.9). Except for the very thin region, all spectra show a reflection peak near 1.9 µm and Fabry-Pérot fringes at longer wavelengths. For all structural thicknesses, a strong transmission band always exists at long wavelength mid IR, indicating that the 3D metal structure is disconnected. Comparing figure 5.8b and 5.8c, it seems that the major optical response of the metallodielectric photonic crystal is dominated by the dielectric structure. The metal rings contribute little to the resonant behavior of the photonic crystal but dominated the absorption. It would be interesting to study the field distribution in the composite photonic crystal and its relation with total absorption. It is also interesting to study the behavior of a pure metallic photonic crystal with discrete metal elements. To do so, an infra-red transparent refractive index matching liquid (carbon tetrachloride) is applied on the metallo-dielectric photonic crystal with a CaF_2 window cover the top to ensure a flat top surface. Reflection and transmission spectra (figure 5.10) show that all features disappears at short wavelength and only Fabry-Pérot fringes remain at long wavelength with much lower modulation. Although the structure shown here is not a metamaterial, which requires resonance elements such as split rings[21] and a lower loss metal than CVD tungsten, we believe that by designing and fabricating a proper template with the appropriate curvature distribution using methods such as interference lithography or direct writing [11-14] and by choosing the right low loss materials, such structures may be achievable.

5.6 Conclusion

In summary, we describe an innovative fabrication technique: template assisted 3D nanolithography. Using colloidal crystals as templates, nanoring particles and metallodielectric photonic crystals are fabricated. The combination of this approach with more complex templates, with designed negative curvature distribution, for example those formed through optical interference,[11, 22-24] may provide a path to otherwise unobtainable nanostructures and complex photonic structures.

5.7 Experimental

5.7.1 Colloidal Film Formation

All percentage listed below are based on weight. All silicon wafer substrates mentioned are pre-cleaned by a mixture of (3:1) sulfuric acid and 30% hydrogen peroxide (hazardous, handle with care).

Colloidal films of 1.58 μm silica colloids are made by drying a few drops of 1% aqueous colloidal solution on a piece of silicon wafer. The multi-layer film appears amorphous with small crystalline domains. Colloidal crystals made from 920 nm and 550 nm diameter silica particles are formed by controlled drying process in 1.5% ethanol solution at 40 °C. Colloidal crystals made from 1.8 μm diameter polystyrene (PS) are formed by vertical drying a 0.2% aqueous solution PS colloidal spheres on a silicon wafer at 55 °C.

5.7.2 Tungsten Ring Particle Synthesis

A 2 nm alumina layer is coated by ALD on all silica colloidal films to improve structural strength and their adhesion to the substrate. Tungsten chemical vapor deposition is based on thermal decomposition of tungsten hexacarbonyl $W(CO)_6$.[8] The silica colloidal film sample and $W(CO)_6$ powder were loaded into a 30ml stainless steel tube. The tungsten film thickness can be controlled by varying the amount of $W(CO)_6$. The tube was evacuated and refilled with 5~10 psi of H_2. The tube was heated at 375C for 3h and cooled down naturally. Conformal-etching of tungsten is done by anodizing tungsten coated colloidal film in 10% sulfuric acid for 30S followed by chemical etching in 1M KOH solution. The resistance of the film is measured after each etching cycle and the reaction is stopped when the resistance goes to infinity. The degree of etching is then confirmed by SEM. To get discrete tungsten rings, the colloidal crystal is then etched in 1% HF aqueous solution followed by washing with DI water and centrifugation.

5.7.3 Alumina Ring Particle Synthesis

PS colloidal crystals are coated with about 60 nm of Al_2O_3 by atomic layer deposition (Cambridge NanoTech Inc.) with trimethylaluminum and water as precursors at 80 °C. Conformal etching is done in 10% w/w aqueous HF ethanol solution at -21 °C (temperature stabilized by the eutectic point of saturated salt water). Etching time is ~45 mins. The degree of etching is checked by SEM and more etching is performed as needed until ring particles are separated. PS colloids are then dissolved in tetrahydrofuran (THF). Particles are then washed for 2 cycles in THF by centrifugation.

5.8 Tables

Table 5.1. Colloid diameter, W coating thickness, and ring particle dimensions for images presented in figure 5.5

	colloid diameter (nm)	W coating thickness (nm)	ring particle diameter (nm) ± standard deviation (nm)	ring particle thickness (nm) ± standard deviation (nm)
(a)	1580	60	640±58	132±9.4
(b)	1580	40	454±93	93.1±4.6
(c)	920	40	328±37	88.8±4.2
(d)	550	20	220±12	41.9±4.0

5.9 Figures

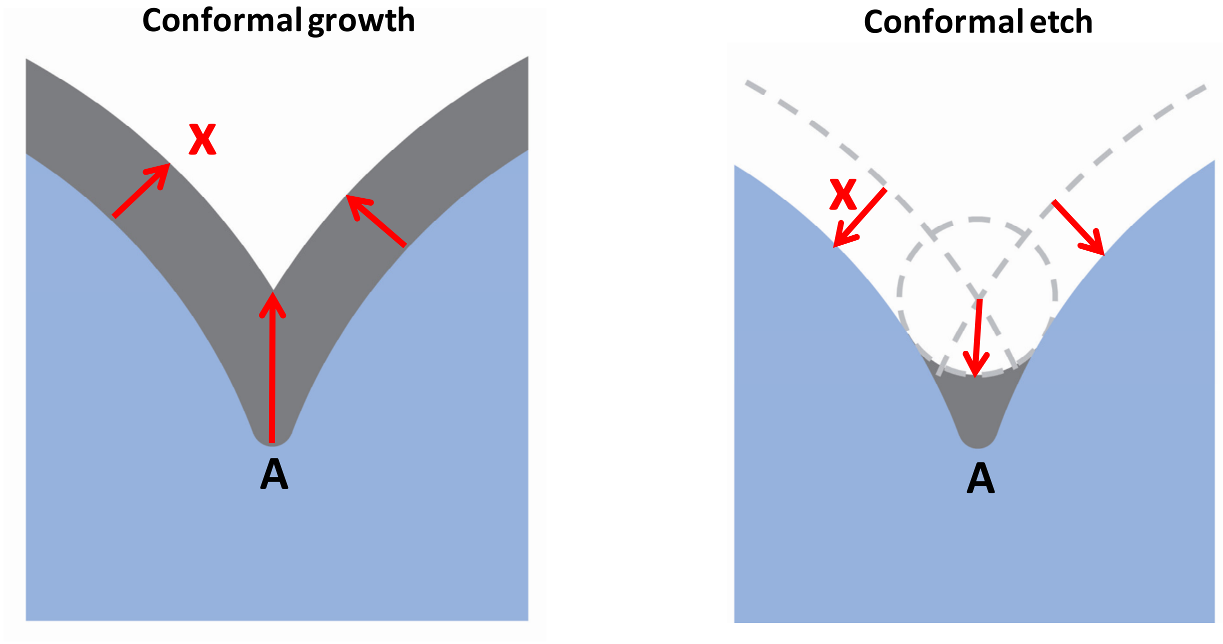

Figure 5.1. Schematic of an irreversible conformal growth (a) and conformal etching (b) process in two dimensions. After deposition and etching of the same thickness of material, some material remains in areas with a small negative radius of curvature.

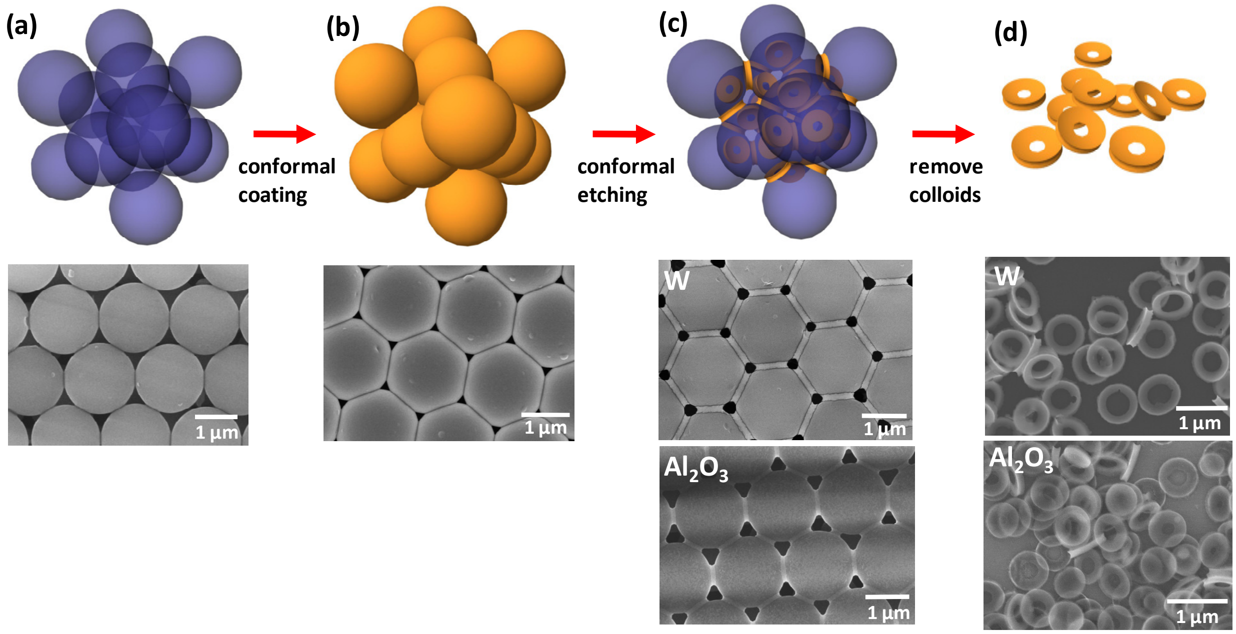

Figure 5.2. Schematic diagram and SEM images of the four stages of the process for synthesizing ring particles: (a) colloidal crystal template formed by self-assembly, SEM image shows a crystalline silica colloidal film; (b) after conformal coating by CVD or ALD, SEM shows a tungsten CVD coated silica colloidal crystal; (c) ring particles formed in between colloids after conformal wet etch, SEM images show tungsten and Al_2O_3 ring particles formed at the silica and polystyrene colloid contact points, respectively; (d) released ring particles, SEM images show well dispersed tungsten and Al_2O_3 ring particles after etching of the colloidal crystal template.

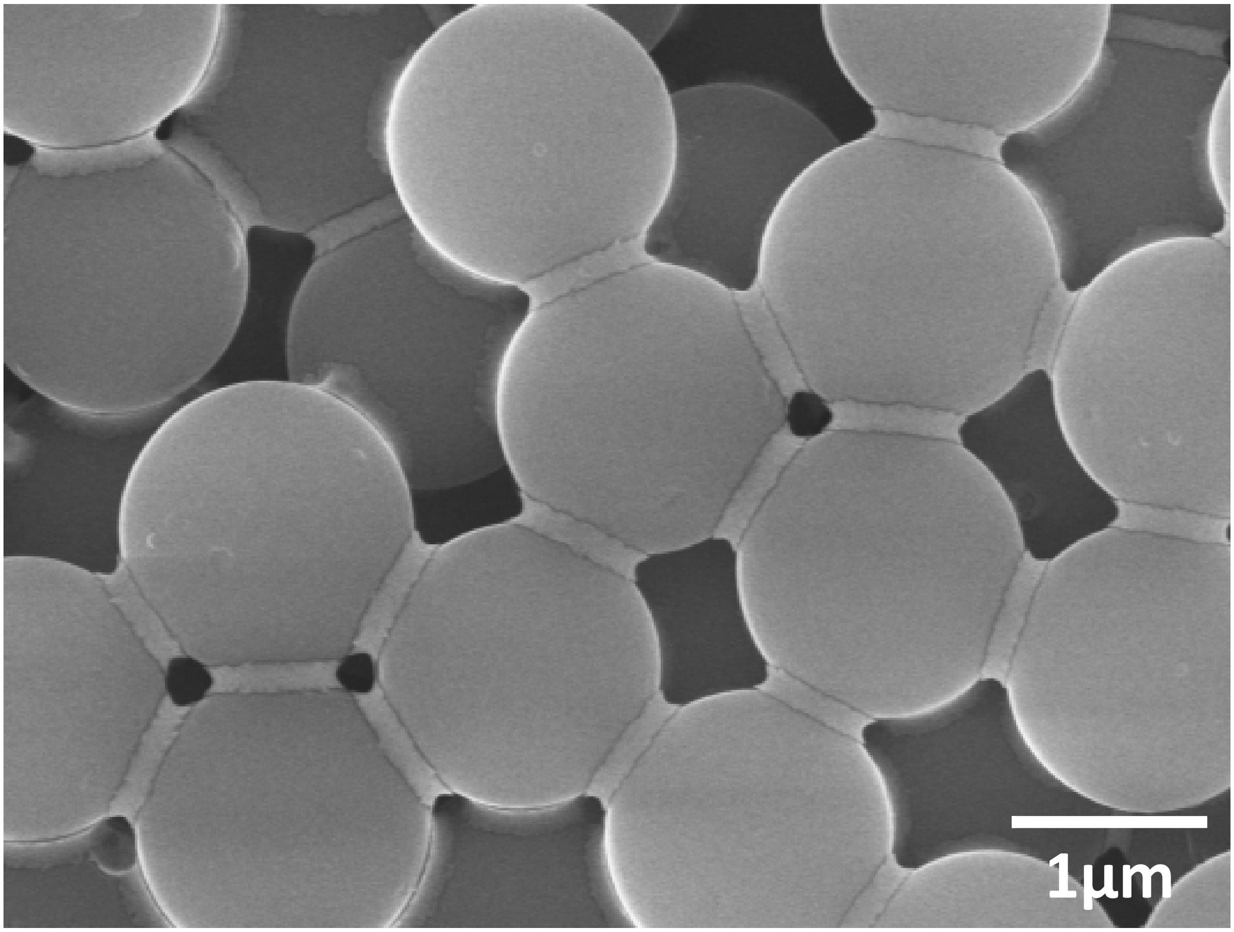

Figure 5.3. SEM image of tungsten ring particles generated in-situ at each colloid contact point in a randomly packed colloidal film. The ring particles are discrete and reasonably monodispersed.

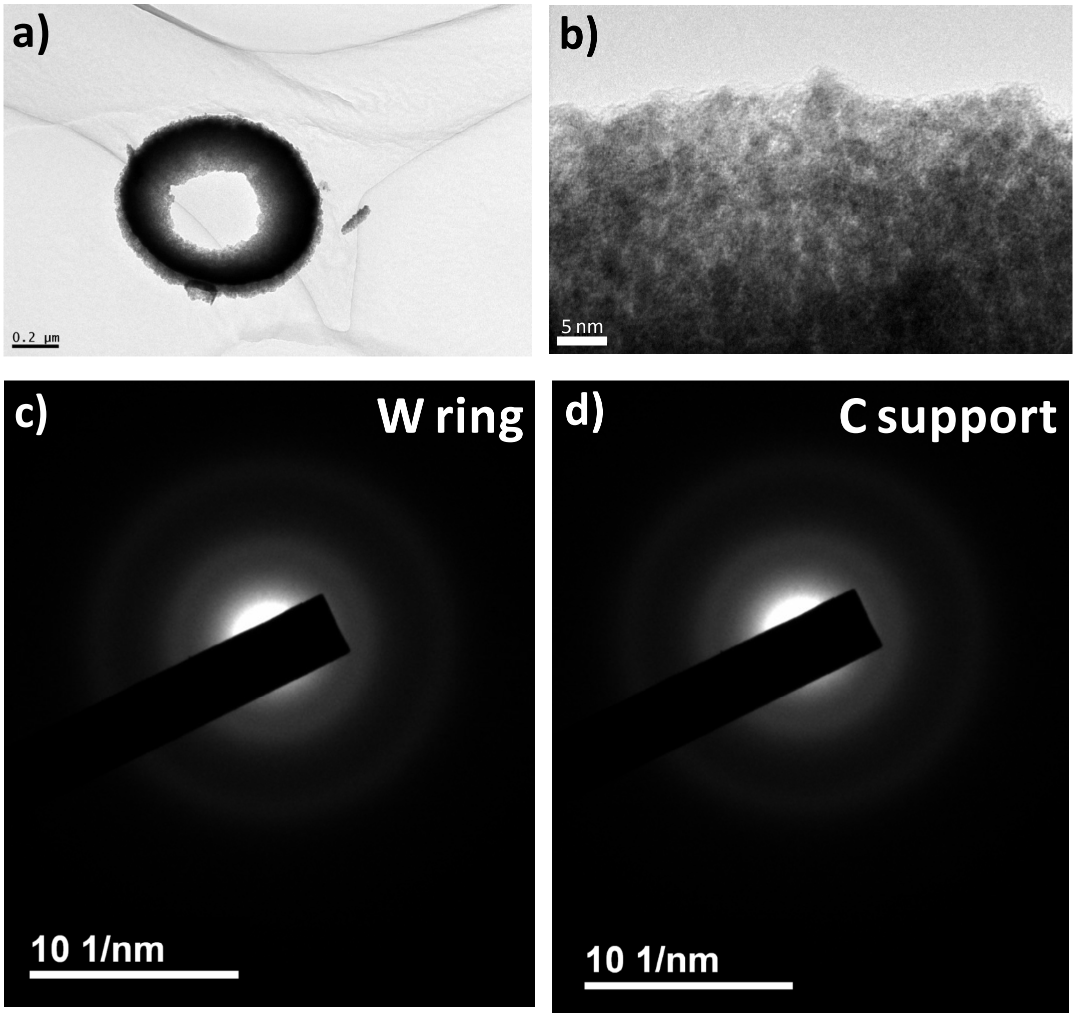

Figure 5.4. a) and b) TEM images of a tungsten ring particle. c) and d) Electron diffraction pattern of a single tungsten ring particle (c) and carbon support of the TEM grid (d). From the diffraction pattern, we conclude that the tungsten film is amorphous.

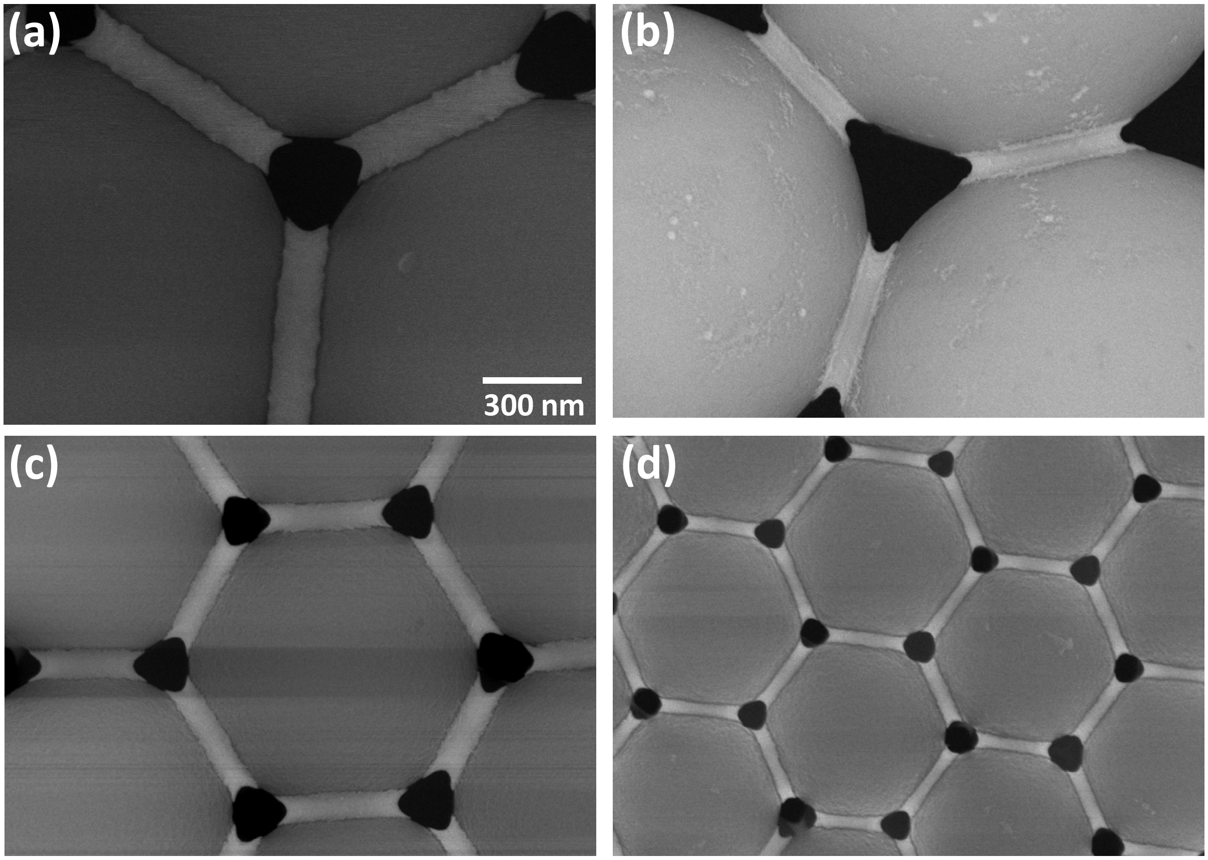

Figure 5.5. (a-d) SEM images of tungsten ring particles before release from the colloidal template. All images are of the same magnification. The diameter and the thickness of the rings can be independently adjusted by using colloids of different sizes as templates and by varying the conformal coating thickness (see table 1 for numerical values).

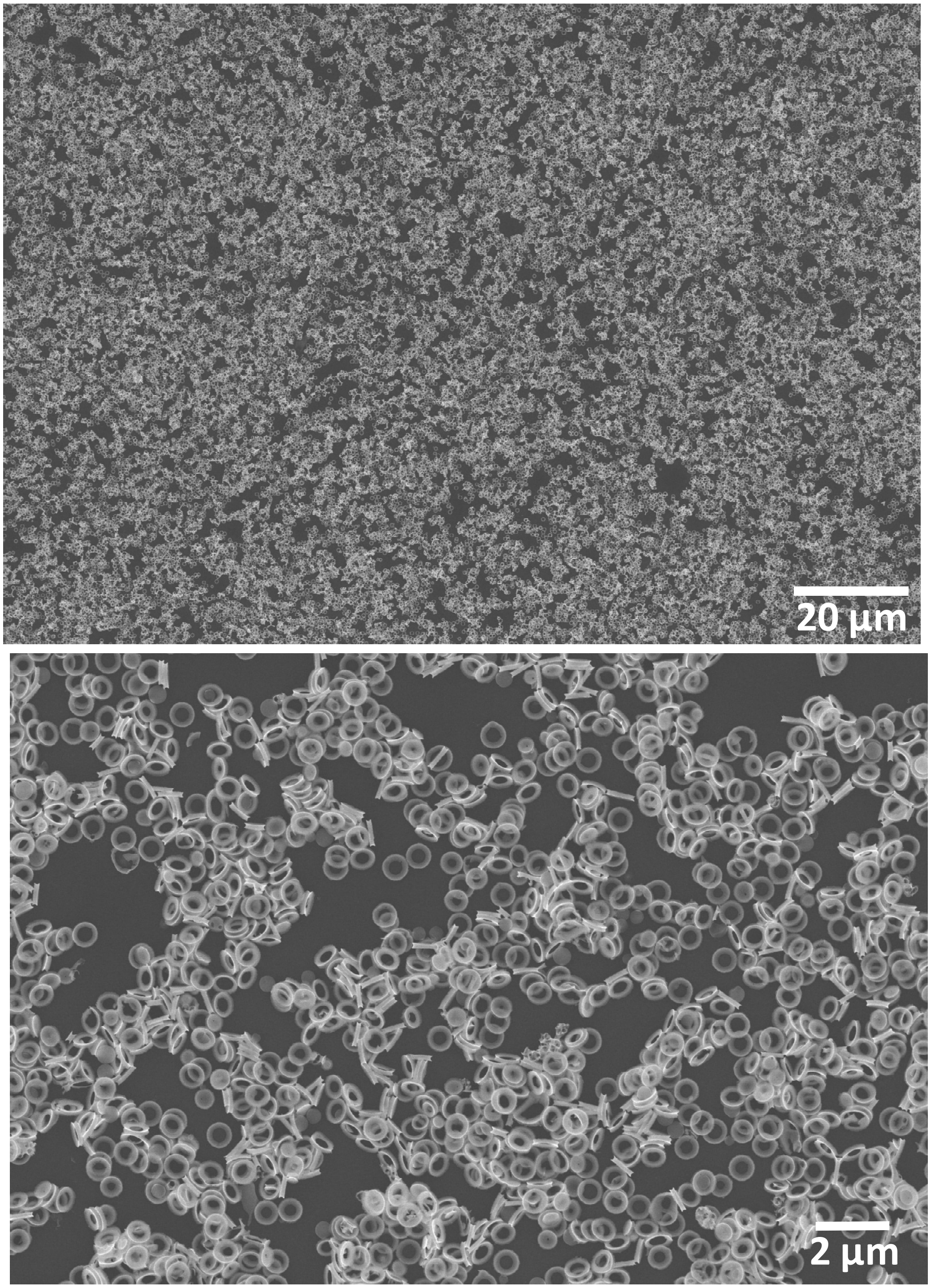

Figure 5.6. SEM images of large numbers of tungsten ring particles solvent cast on a silicon wafer. The 3D template assisted lithography technique is capable of producing ring particles with areal density 2 orders of magnitude higher than conventional nanosphere lithography approaches.

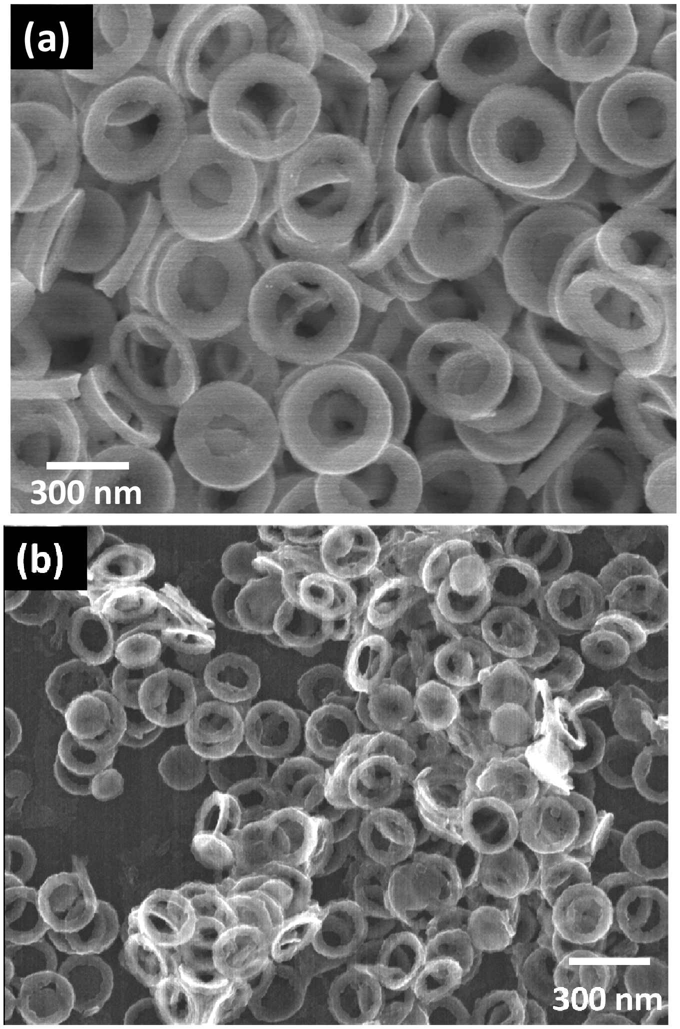

Figure 5.7 SEM images of released tungsten ring particles fabricated using templates formed from colloids of different diameter. The ring particles are released from colloidal templates formed from (a) 920nm and (b) 550nm diameter SiO_2 colloids. Image (a) and (b) are of same magnification. The tungsten coating thickness in (a) and (b) are very close to the samples shown in figure 5.5c and 5.5d in the main text.

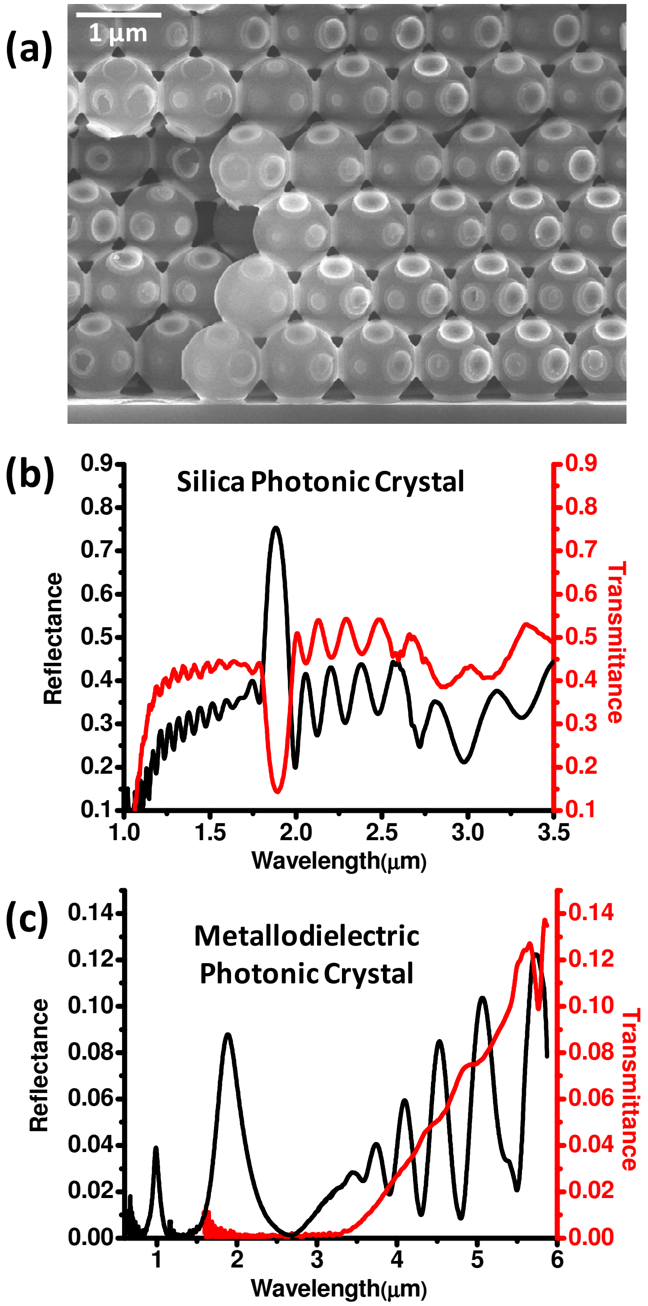

Figure 5.8 Metallodielectric photonic crystal composed of discrete W ring particles formed in-situ using a 920 nm diameter silica colloidal crystal template. (a) Cross-section SEM image of the metallodielectric colloidal crystal. Discrete tungsten ring particles are clearly seen. (b) Reflection (black trace) and transmission (red trace) spectra of silica colloidal crystal template before tungsten deposition. (c) Reflection (black trace) and transmission (red trace) spectra of metallodielectric photonic crystal shown in (a) after W deposition and etching.

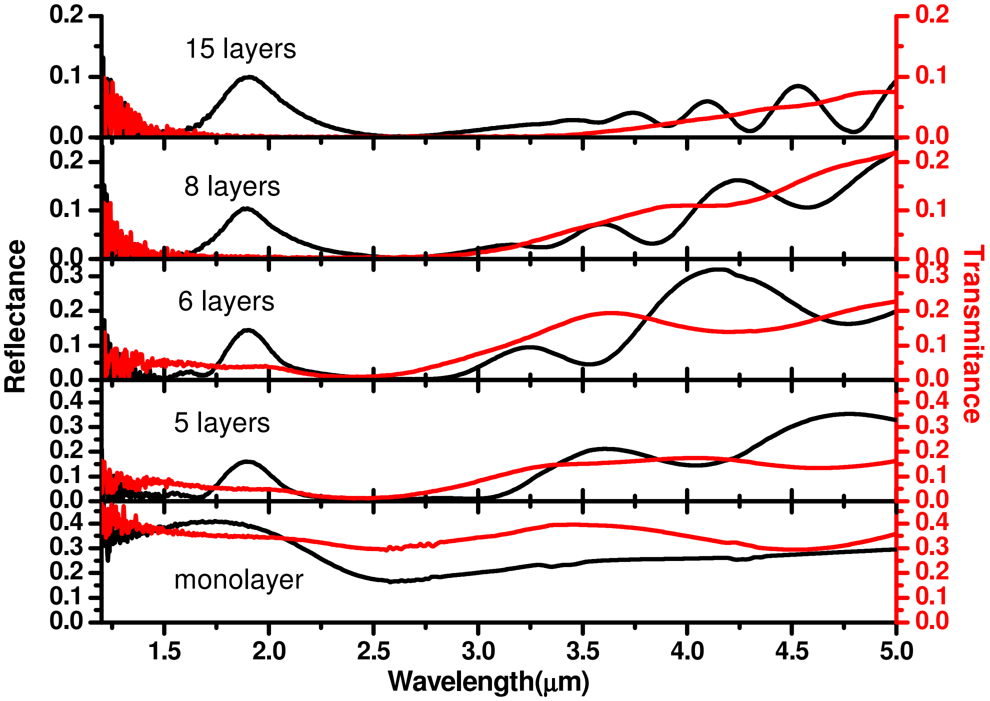

Figure 5.9 Reflection (black trace) and transmission (red trace) spectrum of a tungsten-silica metallodielectric photonic crystal as a function of number of layers. The photonic crystal shows a reflection peak near 1.9 μm and Fabry-Pérot fringes at longer wavelengths. For all structural thicknesses, a strong transmission band always exists at long wavelength mid IR, indicating that the 3D metal structure is disconnected.

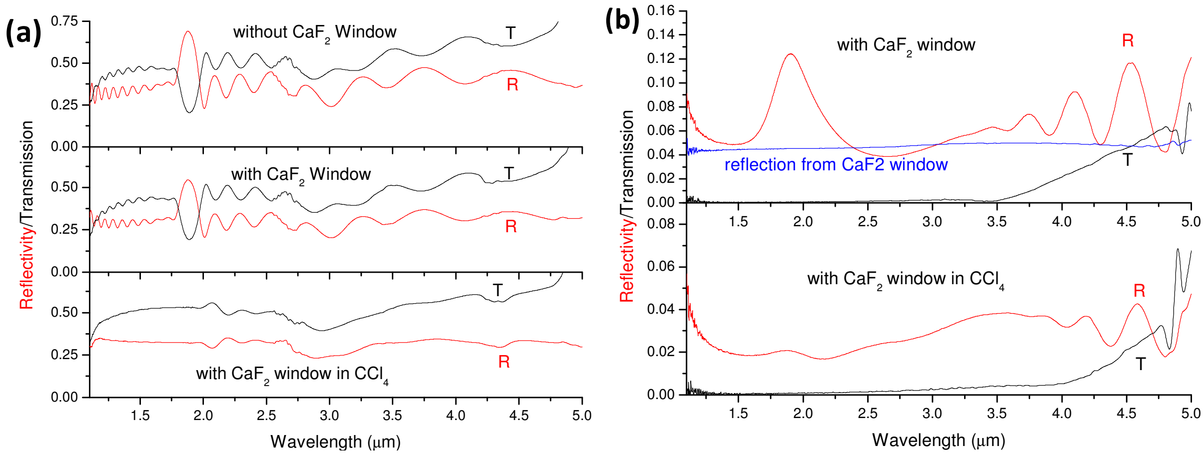

Figure 5.10. Reflection and transmission spectrum of refractive index matched dielectric (a) and metallodielectric (b) photonic crystals. (a) Reflection (red trace) and transmission (black trace) spectra of 15 layer 920 nm silica colloidal crystal in air (upper), in air with a CaF_2 window (middle) and in carbon tetrachloride (CCl_4) with a CaF_2 window. The refractive index of carbon tetrachloride matches that of silica fairly well. As a result the modulations become much weaker. (b) Reflection (red trace) and transmission (black trace) spectra of 15 layer tungsten silica metallodielectric photonic crystal made from the same colloidal crystal as in (a) in air with CaF_2 window (upper) and in CCl_4 with CaF_2 window (lower). The blue trace in the upper spectra is reflection from the CaF_2 window itself without sample under it. That explains the higher reflection base line in reflection spectrum. As shown in the lower spectra, when reflective index of the silica is matched, the modulation becomes much weaker, indicating that the majority of the optical response is due to the dielectric part of the photonic crystal, probably due to its higher volume filling fraction. However the pass band at longer wavelengths still exists with a slight red shift compared with the spectrum measured in air.

5.10 Reference

1. Hawker, C. J.; Russell, T. P. *Mrs Bulletin* **2005,** 30, (12), 952-966.
2. Chik, H.; Xu, J. M. *Materials Science & Engineering R-Reports* **2004,** 43, (4), 103-138.
3. Li, Y.; Cai, W.; Duan, G. *Chemistry of Materials* **2008,** 20, (3), 615-624.
4. Yang, S. M.; Jang, S. G.; Choi, D. G.; Kim, S.; Yu, H. K. *Small* **2006,** 2, (4), 458-475.
5. Anker, J. N.; Hall, W. P.; Lyandres, O.; Shah, N. C.; Zhao, J.; Van Duyne, R. P. *Nature Materials* **2008,** 7, (6), 442-453.
6. Little, B. E.; Foresi, J. S.; Steinmeyer, G.; Thoen, E. R.; Chu, S. T.; Haus, H. A.; Ippen, E. P.; Kimerling, L. C.; Greene, W. *Ieee Photonics Technology Letters* **1998,** 10, (4), 549-551.
7. Zhu, F. Q.; Fan, D. L.; Zhu, X. C.; Zhu, J. G.; Cammarata, R. C.; Chien, C. L. *Advanced Materials* **2004,** 16, (23-24), 2155.
8. Nagpal, P.; Han, S. E.; Stein, A.; Norris, D. J. *Nano Letters* **2008,** 8, (10), 3238-3243.
9. Anik, M.; Osseo-Asare, K. *Journal of the Electrochemical Society* **2002,** 149, (6), B224-B233.
10. Wong, S.; Kitaev, V.; Ozin, G. A. *Journal of the American Chemical Society* **2003,** 125, (50), 15589-15598.
11. Campbell, M.; Sharp, D. N.; Harrison, M. T.; Denning, R. G.; Turberfield, A. J. *Nature* **2000,** 404, (6773), 53-56.
12. Jeon, S.; Park, J. U.; Cirelli, R.; Yang, S.; Heitzman, C. E.; Braun, P. V.; Kenis, P. J. A.; Rogers, J. A. *Proceedings of the National Academy of Sciences of the United States of America* **2004,** 101, (34), 12428-12433.
13. Deubel, M.; Von Freymann, G.; Wegener, M.; Pereira, S.; Busch, K.; Soukoulis, C. M. *Nature Materials* **2004,** 3, (7), 444-447.
14. Gratson, G. M.; Xu, M. J.; Lewis, J. A. *Nature* **2004,** 428, (6981), 386-386.
15. Rill, M. S.; Plet, C.; Thiel, M.; Staude, I.; Von Freymann, G.; Linden, S.; Wegener, M. *Nature Materials* **2008,** 7, (7), 543-546.
16. Chen, H. H.; Suzuki, H.; Sato, O.; Gu, Z. Z. *Applied Physics a-Materials Science & Processing* **2005,** 81, (6), 1127-1130.
17. Liang, Z. J.; Susha, A. S.; Caruso, F. *Advanced Materials* **2002,** 14, (16), 1160-1164.
18. Bartlett, P. N.; Ghanem, M. A.; El Hallag, I. S.; de Groot, P.; Zhukov, A. *Journal Of Materials Chemistry* **2003,** 13, (10), 2596-2602.
19. Pendry, J. B.; Holden, A. J.; Robbins, D. J.; Stewart, W. J. *Ieee Transactions on Microwave Theory and Techniques* **1999,** 47, (11), 2075-2084.
20. Koschny, T.; Zhang, L.; Soukoulis, C. M. *Physical Review B* **2005,** 71, 121103.
21. Linden, S.; Enkrich, C.; Wegener, M.; Zhou, J. F.; Koschny, T.; Soukoulis, C. M. *Science* **2004,** 306, (5700), 1351-1353.
22. Chen, Y. C.; Geddes, J. B.; Lee, J. T.; Braun, P. V.; Wiltzius, P. *Applied Physics Letters* **2007,** 91, (24), 241103.

23. Pang, Y. K.; Lee, J. C. W.; Lee, H. F.; Tam, W. Y.; Chan, C. T.; Sheng, P. *Optics Express* **2005,** 13, (19), 7615-7620.
24. Rinne, J. W.; Wiltzius, P. *Optics Express* **2006,** 14, (21), 9909-9916.

CHAPTER 6
SPECIAL SHAPED NANOPARTICLES FOR BIOLOGICAL APPLICATIONS

The work presented in this chapter was a collaboration with Abhijit Mishra in Prof. Gerard Wong's group and Li Tang in Prof. Jianjun Cheng's group.

6.1 Introduction

One important topic in the field of bioscience is the transport and delivery of bio materials, which include DNAs, proteins and other molecules like cancer drugs. The criteria for successful delivery varies according to the nature of the payload. In the case of gene delivery, relatively large DNA/RNA molecules needs to transfer from outside the cell, cross cell membrane, move through inner cell skeleton, cross nucleus membrane and eventually reach the nucleus without any chemical and structural mutation. In the case of drug deliver, the key is to prevent the drug molecules from being captured by healthy organs of human body and causing side effects. The drug needs to keep circulating inside human body with high chemical stability until is concentrates at targeted area(s) and perform the desired function. These requirements are so complex and sometimes contradicting such that only in rare cases can simple molecular systems can meet all demands [1]. On the other hand, nanoparticle based delivery systems bring new hope to this challenging task [2-4]. It is because that, in principle, the chemical composition, internal structure, shape and size are all independently tunable. The next challenge is how to take advantage of these design parameters to achieve the final goal.

Recently, the effects of the shape of nanoparticles on their bio-interaction properties have attracted much attention. For example, particles of exactly the same chemical composition and different geometry have shown different efficiency endocytosis, an active transportation process in which cell deforms its cell membrane to bring external material inside [5]. The shape effect is probably not that surprising, because the world of micronbiology is abundant of irregular shapes, from red blood cell to various shaped viruses [6].

Let's hold on a second and think about how shape affects cell/particle interaction? Imagine a particle of certain shape hits a cell, the cell with it skeleton supported membrane probably would not sense the complete shape of the particle, but rather only obtain information of local geometry. That information probably triggers the cell to take action, that is to uptake that particle, or not to take action, which is to leave the particle alone. This local geometry effect has been demonstrated by interaction of cells and elliptical particles [7].

The next question is: what information about shape can cells gather? The answer is probably local curvatures. A curvature, $\kappa=1/R$, where R is the radius of curvature at a certain point. A 3D curvature can be well discribed by two parameters: mean curvature and Gaussian curvature. Mean curvature is the average of two principle curvatures along two major directions and contains the information about sharpness of the shape. It is proportional to the capillary pressure of a surface or an interface that has such curvature. The sharper the shape the larger the absolute value of the pressure. It's not hard to imagine that when a particle with very sharp edges hit a cell, the capillary force might induce membrane deformation and trigger an uptake event.

Gaussian curvature is defined as the multiplication of the two principle curvatures. The effect of Gaussian curvature can be subtle because a very large negative Gaussian curvature (NGC) could have a small mean curvature and thus little capillary pressure. Recently, Prof. Gerard Wong's group discovered that antimicrobial peptide function by distorting the bacterial membranes into a 3D phase full of NGC [8]. This phase could help to trigger endocytosis. NGC also presents in direct pore formation on the cell membrane [9]. All these clues lead to the hypothesis that particles with NGC might facilitate particle uptake by either triggering endocytosis or direct pore formation.

In this chapter, particles with large mean curvature and NGC are prepared via template assisted fabrication, sometimes with controlled surface chemistry. Preliminary biostudy results are also presented.

6.2 Metallic Nanoparticle with High Local Mean Curvature

Small particles intrinsically have smaller mean curvature. Smaller dimensions also probably make them easier to be uptaken than larger particles. Elliptical particles and rod shaped particles have smaller mean curvature at the ends. However, it is difficult to produce these kinds of particles with extremely sharp ends and their length, and sometimes diameter is generally polydisperse. Star shaped particles, ones with multiple arms extended from the same center, appear as good candidates because they have both sharp features at very ends of their arms and relatively spherical geometry when connecting all the tips.

Star particles have been chemical synthesized via seed mediated and surfactant directed process by carefully control growth kinetics [10]. These particles have are about 100 nm in diameter and the tip of these particles have radius of curvature of about 10 nm. Drawbacks of this approach include that the number of arms per particle is not well defined and the particles are also polydispersed in size.

To overcome all these issues, a different fabrication approach is taken here. In a colloidal crystal, spherical colloids occupy the FCC lattice sites. The interstitials left behind are either tetrahedral sites that look like pyramids with triangular bases or octahedral sites that are better described as cubes. The interstitials sites are interconnected by thinner parts.

In chapter 2, the interstitial of a colloidal crystal is first filled with nickel and then a technique called electropolishing reduces the metal filling fraction and leaves a highly porous skeleton. If the etching process goes further, the thinnest part will be completely consumed, leaving the thicker parts of the interstitials disconnect from each other and fall free as nanoparticles (Fig 6.1). By tuning the parameters, star nanoparticles with extremely sharp tips and smooth surface are produced (Fig.6.2). Radius of curvature at the tip is in the range of 2~5 nm, much narrower than chemical synthesized ones. And because of the highly regular colloidal crystal structure, size and shape dispersity is very narrow.

In principle, this three dimensional template assisted fabrication can produce nanoparticles with quantities on the same order of magnitude as the spherical colloids that form the colloidal crystal. However, difficulty in this approach lies in the step of harvesting the particles. Once particles detach from the main frame, most of them fall into the electropolishing solution, which is a mixture of phosphoric acid and diethlyene glycol monoethyl ether. The solution chemically etches nickel, too, in a slower rate because of low water content. How to remove all the acid and get particles within the time frame before their surface get significantly damaged is a huge challenge.

Luckily, if the porous nickel sample is tilted slightly upwards, there are some particles physisorbed on the sample surface. These particles can then be diluted in water and purified reasonably easily. The harvested particles are shown in figure 6.3.

Other than potential bio-interaction applications, metallic nanoparticles with sharp features also show interesting optical properties due to surface plasmon resonance [10]. It has been demonstrated that when excited at the correct wavelength and polarization, optical energy is highly concentrated near the sharp edges and the resulting Raman signal are orders of magnitude higher than without the enhancement [11]. Resonance frequency of nickel particles are measured by dark field scattering spectrum, in which scattered light is collected and normalized by bright field signal. The end result is a spectrum that represents the relative scattering cross-section of the particles for light of different wavelength. In order to obtain well separated particles, a flat PDMS stamp is used to pick up physisorbed nickel particles from the surface of the porous nickel film. SEM images show that the tips of star particles remain intact (Fig 6.4). Scattering spectrum shows that there are two major scattering peaks located in the blue and near IR regions (Fig 6.5). Strong resonances at the tips of these particles are expected at these wavelengths with light polarized along the stretching direction of these tips.

6.3 Gold Nanoparticles with Negative Gaussian Curvature

Particles with NGC are intrinsically difficult to synthesize via traditional chemical synthesis route because reaction tends to minimize the particle/solvent interface, resulting in particles with all positive gaussian curvatures (such as spherical particles). Kinetically controlled synthesis methods, in some cases do produce particles with NGC, such as the gold star particles mentioned earlier [10]. However, locations of NGC are hard to access by foreign objects.

In the interstitials of inverse opal structure, NGC exists near the contact point of colloidal spheres. If these space can be replicated into the form of nanoparticles, we will get the particles with the curvature we want. The detailed fabrication scheme is shown in figure 6.6. First, a colloidal crystal is formed on a conductive substrate. Then a layer of nickel is electrochemically deposited through the crystal. The thickness of that nickel layer is well controlled by monitoring the deposition voltage so that the growth front of nickel just reaches the lower part of the interconnection windows (Fig. 6.7a). Following that, gold is electrodeposited on top of nickel. The thickness of the gold layer is also controlled so that they fully replicate the NGC but is not too thick to be interconnected at the top. After removing the template, a monolayer of muffin like particles are exposed and anchored on the substrate via the gold/nickel interface (Fig. 6.7b). It turns out that this interface is weak enough (Fig 6.7c) that a brief sonication (30 sec.) breaks it easily and gold particles fall free into the solution without any contamination from the synthesis chemistry (Fig 6.7d). It's worth pointing out that surface chemistry can be applied at different stages of the process to decorate different surfaces of the particle with different functional groups. As shown in the inset of figure 6.7d, the surface of the particle can be divided into 3 groups: A, B and C, in which B contains areas with the NGC. Before etching away colloidal crystals, A surface is exposed. After etching away the colloids, A and B are exposed. And after final particle release, all 3 surfaces are exposed. What I have tried is to functionalize surface A and B with 2-Aminoethanethiol hydrochloride (10mM aqueous solution, 1hour) to obtain a positive surface charge and leave surface C unfunctionalized. Gold particles obtained that way are stable in millipore water for weeks when agitated slowly to avoid sedimentation.

Preliminary bio-studies are also carried out. In the first experiment, amine terminated gold particles are mixed with giant phosphate liquid vesicles at room temperature. The vesicles contain a green dye on the membrane so that it can be imaged under fluorescent microscope. It turns out that fluorescent imaging can also be done under dark field excitation. The advantage of using this microscopy method is that the gold nanoparticles (in orange/red color) can be imaged with vesicles at the same time. This allows tracking the motion and interaction of these moving objects. However, the result is a little surprising, as shown in figure 6.8, gold particles do not stick to the vesicle surface despite their oppositely charged surface. This result is most likely due to the fact that during vesicle synthesis, a large quantity of free phosphate lipids still exist in the liquid. They will adsorb onto the positively charged gold particles and probably cause charge inversion.

To avoid the complication, in the next experiment, particles are incubated with HeLa cancer cells. And after 30mins, many particles have been uptaken by the cells (Fig. 6.9). Detailed study of how does cell uptake rate depend on particle shape is not conducted yet that might deserve future effort. For this purpose, spherical gold particles of similar size can be used as good control experiment.

6.4 Ring Shaped Particles

Fabrication of ring shaped particles have been discussed in chapter 5. By choosing appropriate template, coating material and etching method, tungsten and alumina rings have been made with large quantity and good geometrically control. Particle of this unique geometry is also attractive for biology. The edge of the rim has sharp geometries, that is a large mean curvature. The middle of the rim has negative Gaussian curvature. And the center of the ring particle contains a hole which might function as a passage for material transportation in and out of cells (Fig. 6.10a).

Tungsten rings are relatively easier to fabricate comparing with alumina rings. And the formed particles are bright scattering centers under dark field imaging (Fig. 6.10b). However the bioimplication of tungsten ion is not completely understood. Because of that, alumina rings are selected for bio-related studies.

The fabrication process allows independent functionalization of two sets of surfaces (Fig. 6.11) to form patchy particles. Before etching away the colloidal template, the rim part of the ring particle (surface A in figure 6.11) is first exposed. After etching away the colloids, the rest of the surface (surface B) is also exposed. The first design is to make the rim part of the ring particle is hydrophobic and surface B hydrophilic and slightly positively charged. The surface charge will help stabilize the particles in the solution and help cells attract them. To enable easier detection, the particles need to be labeled with fluorescent dye molecules. The design would hopefully allow the particle to stay on the membrane leaving the central hole open for material transportation (Fig. 6.12).

The chemical functionalization of the rim is achieved this way: first, 1 mg of tetramethylrhodamine isothiocyanate (FRITC) is reacted with 10 mg of aminopropyltriethoxysilane (APS) in 1g anhydrous ethanol for overnight. Isocyanate group reacts with amine group to form a stable silanated rodamine dye. The solution is then diluted to 1 μM in ethanol and reacts with alumina ring samples before the colloidal templates are etched. The mixing ratio is chosen to keep appropriate distance between adjacent dye molecules to avoid self-quenching. After reacting for overnight, the sample is thoroughly rinsed in ethanol and appears orange, indicating that dye molecules have been attached to the surface. Then the sample is immersed in 1mM octadecyltrichlorosilane (OTS) hexane solution for 20mins and rinsed with fresh hexane. OTS backfills any pores that might remain during the dye-APS decoration step and probably cross-link with each other and form a thin over layer above the dye-APS layer. After this step, the rim of the particles are decorated with dye molecules and covered by hydrophobic molecules. And the surface of the sample turns superhydrophobic. The colloidal template is then dissolved in tetrahydrofuran (THF) and is purified by centrifugation and redispersed in fresh THF for 2 cycles. Afterwards, particles are transferred to aqueous solution by disperse and centrifuged in DI water for 2 more times. Under fluorescence microscope, particles show clear fluorescence (Fig 6.13). In aqueous solution, they are slightly aggregated, probably because the surface charge on these particles are not strong enough to prevent hydrophobic rim from approaching each other. Better control over surface chemistry is needed to prevent aggregation. For example, surface B can be decorated with negatively charge polymer, so that the electrostatic repulsion becomes much stronger between these particles.

6.5 Conclusion

A few examples shown in this chapter demonstrated state of art capability of manipulate the shape of nanoparticles and specifically functionalize specific surfaces to form patchy particles. And these particles can be made with quantities orders of magnitude higher than achievable with traditional 2D lithographic methods. Further refinement in fabrication techniques and incorporating appropriate surface chemistry will enable them to show biological functionalities.

6.6 Figures

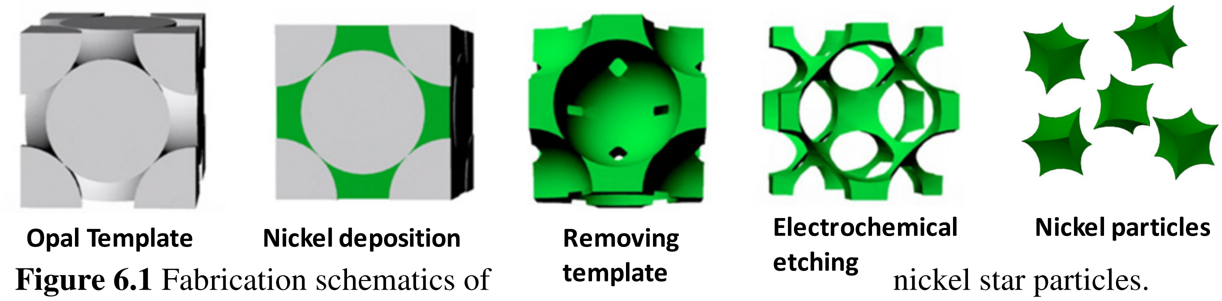

Figure 6.1 Fabrication schematics of nickel star particles.

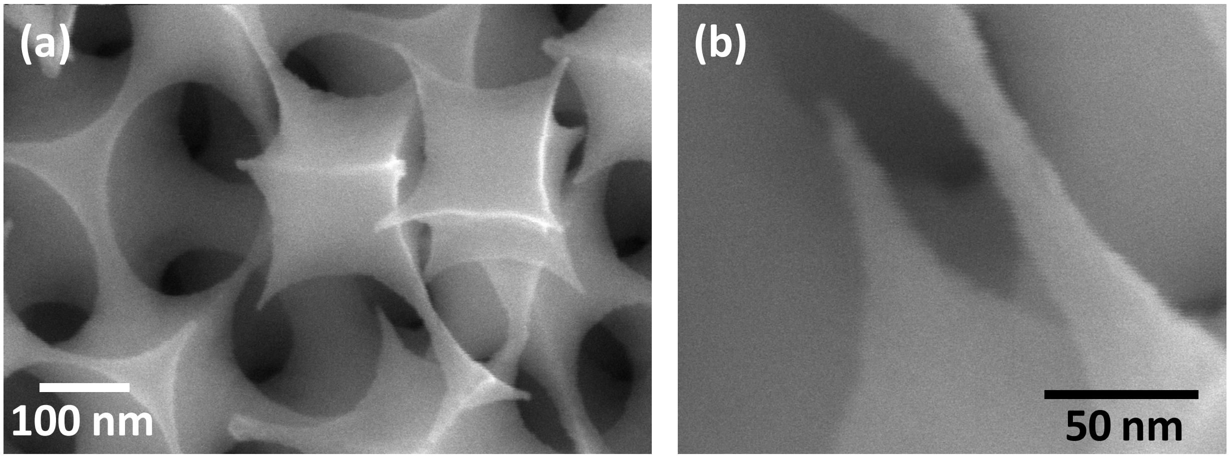

Figure 6.2 Nickel star particles fabricated via 3D template assisted lithography. Radius of curvature at the tip are on the order 2~5 nm.

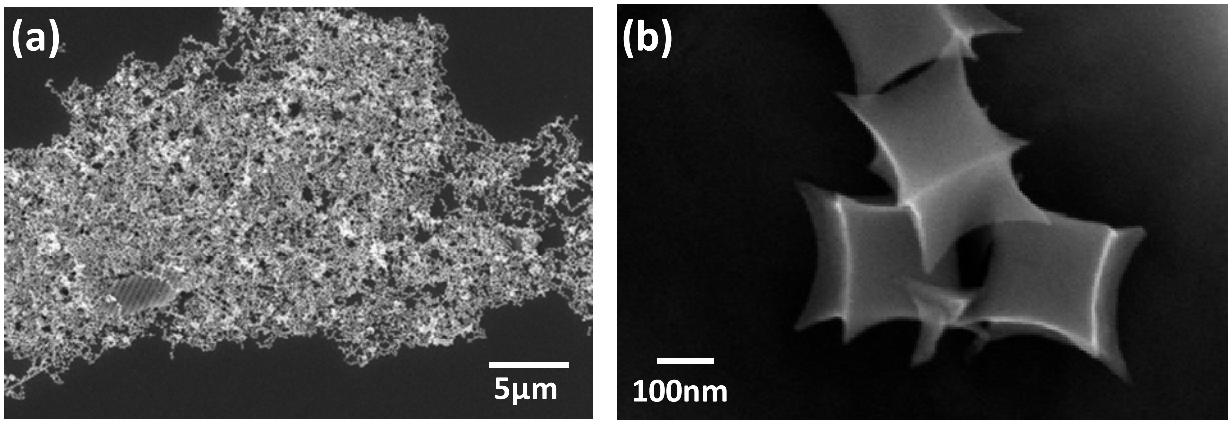

Figure 6.3 Collected nickel star particles after etching and purification. (a) and (b) are SEM images of different magnifications.

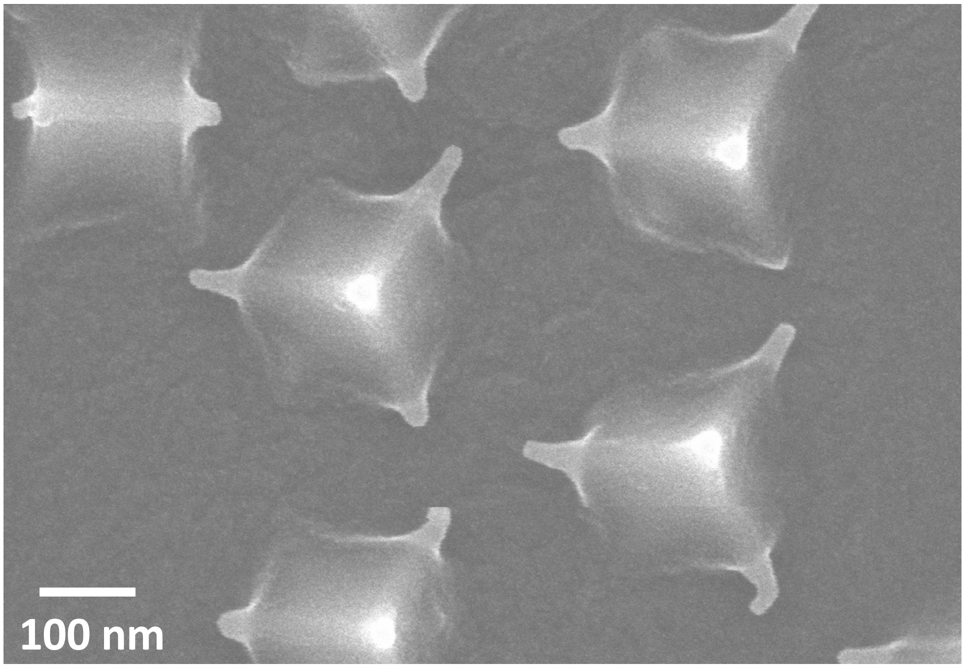

Figure 6.4 Nickel star particles after being transferred onto PDMS surface. All tips are well preserved. Increase in tip diameter is due to gold sputtering for SEM sample preparation.

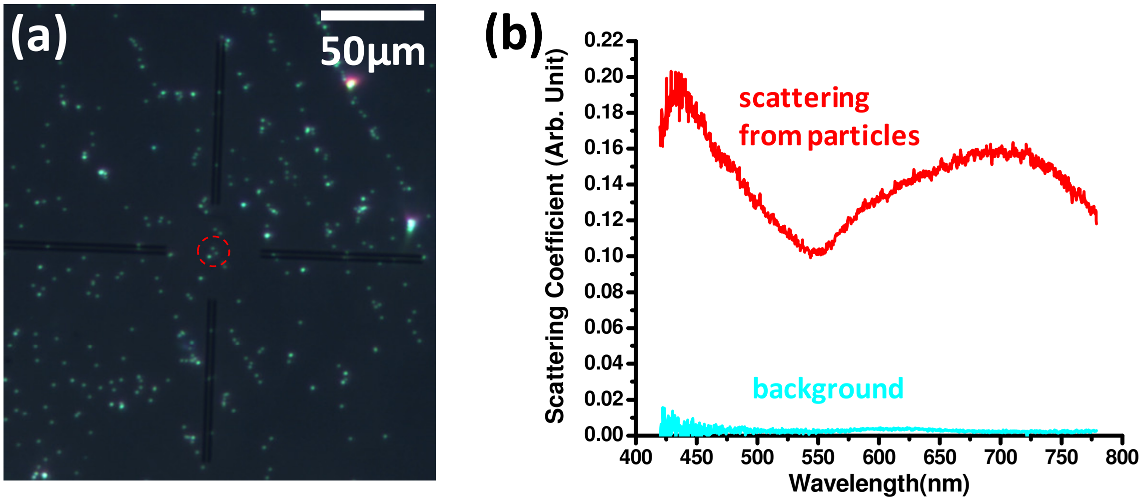

Figure 6.5 (a) Dark field image of nickel star particles transferred onto PDMS surface. The red circle shows the area in which scattering signal is collected for spectrum shown in (b). Particles show scattering maximum at 430 nm and 710 nm.

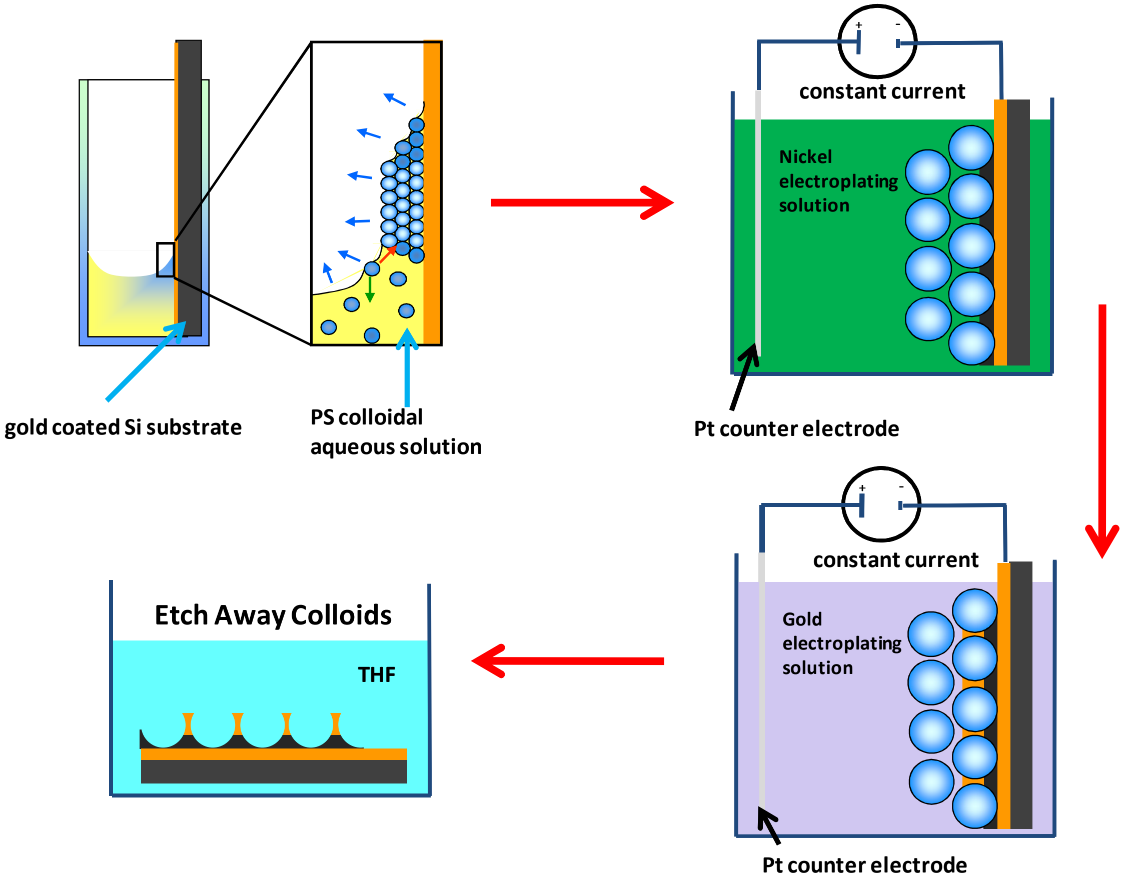

Figure 6.6 Fabrication scheme of gold nanoparticles with negative Gaussian curvature.

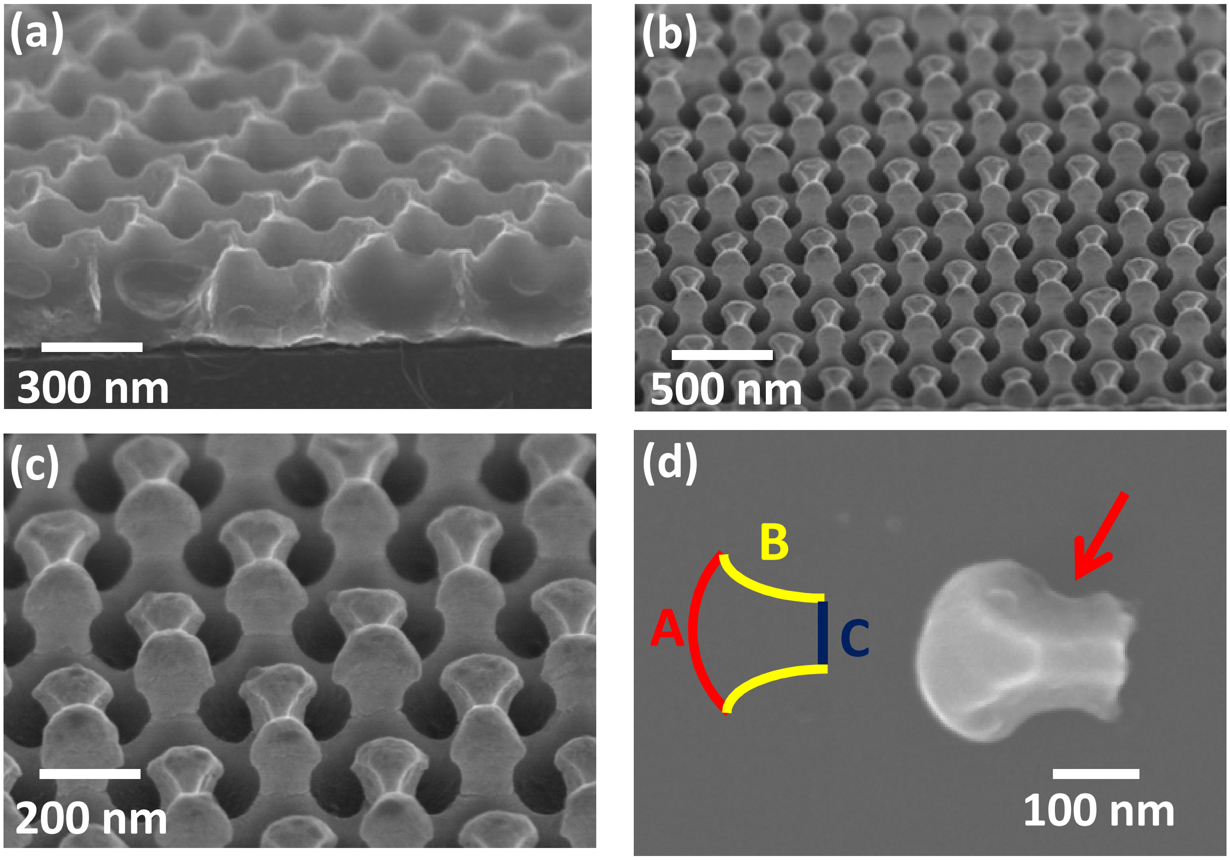

Figure 6.7 (a) and (b) Tilted SEM image of sample after nickel and gold electrodeposition. (c) zoom in image of (b), showing clear nickel/gold interface. Released gold particle after sonication. Red arrow points out the surface with negative Gaussian curvature.

Figure 6.8 A time sequence of 4 dark field optical images showing a gold particle with local negative approaches a phosphate giant vesicle and detaches from it.

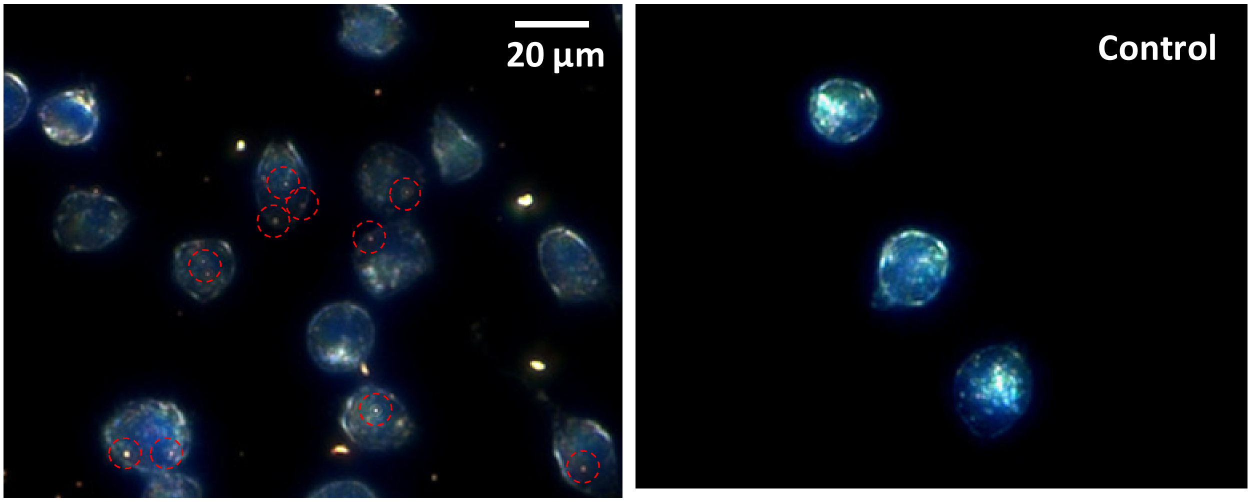

Figure 6.9 Dark field imagine of (a) gold nanoparticles with local negative Gaussian curvature incubated with HeLa cancer cells for 30mins and (b) the control without gold particle. Two images are of the same magnification. The red dotted circles in (a) highlight gold particles inside a cell.

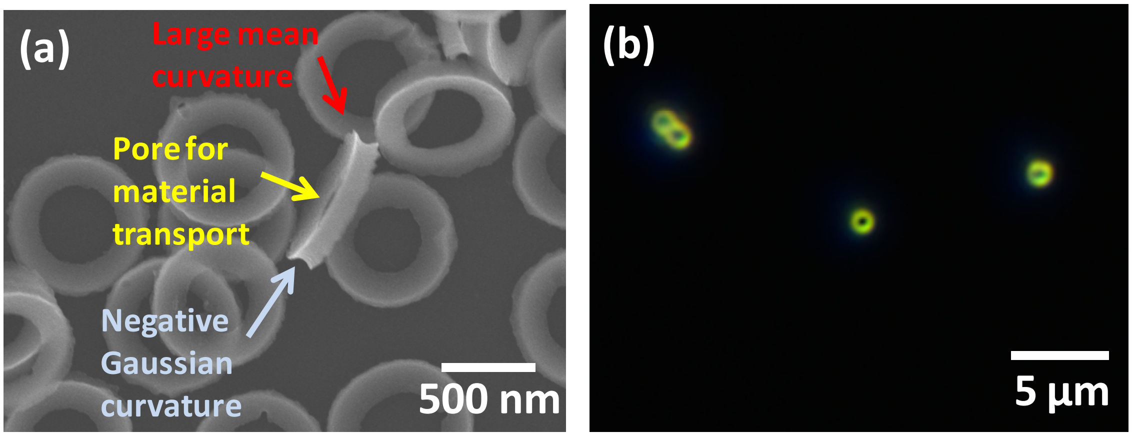

Figure 6.10 (a) SEM image of tungsten ring particles. Arrows show the geometrically features that might have biological implications. (b) Dark field optical image of tungsten rings (700 nm in diameter).

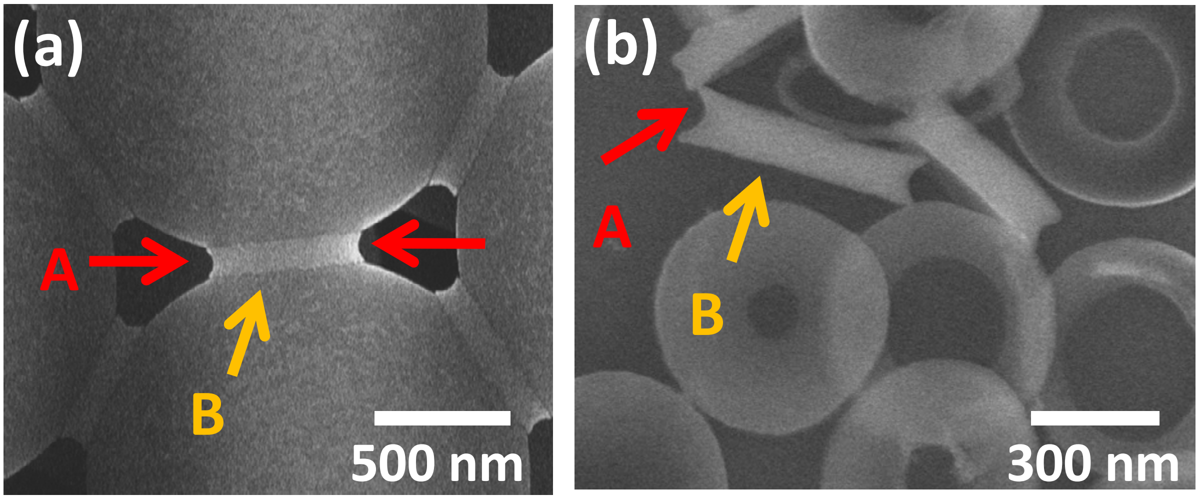

Figure 6.11 SEM images of alumina ring particles before (a) and after (b) release. Before etching away the colloidal template, surface B of the ring particles are projected, allowing chemical decoration only on "A" surface.

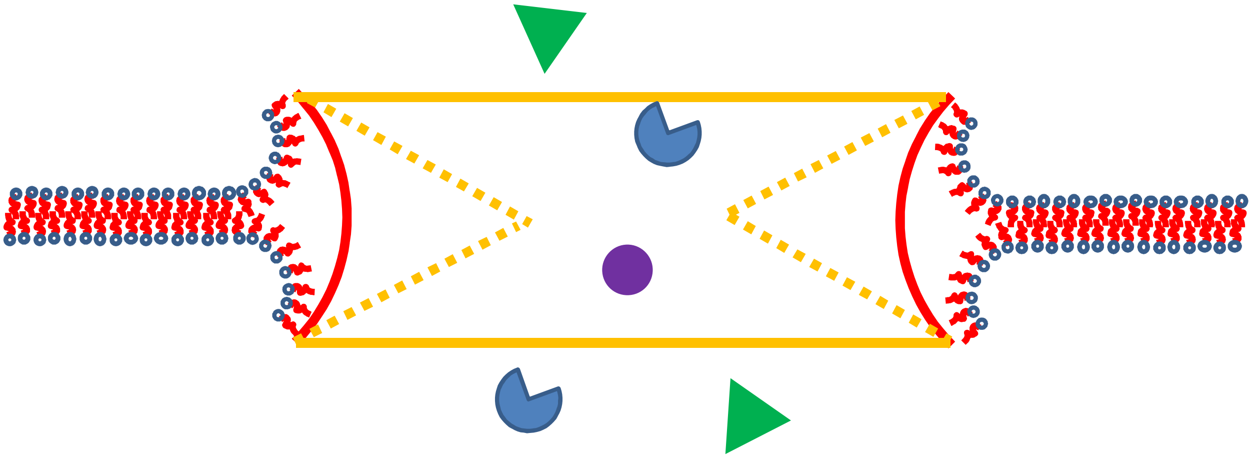

Figure 6.12 The patchy alumina ring particles are designed to allow cell membrane wrap around the hydrophobic rim and allow materials to be transported through the central window.

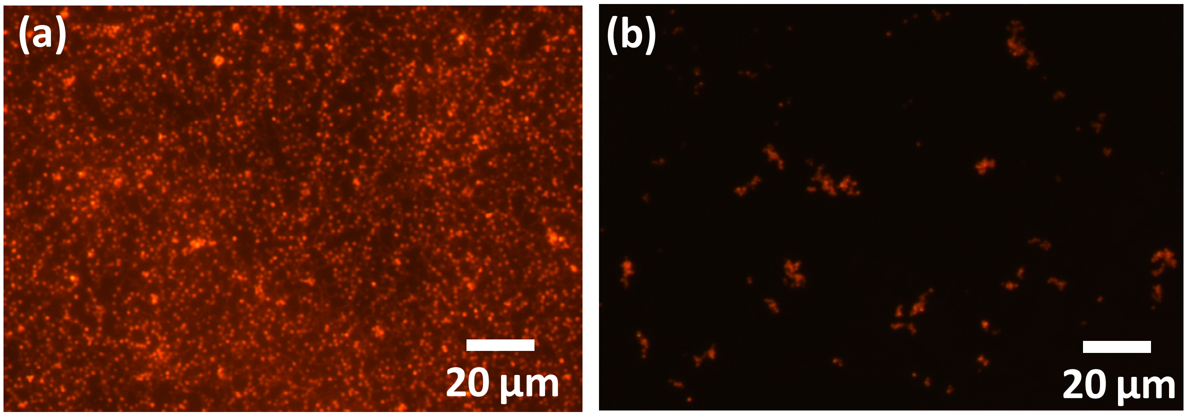

Figure 6.13 Fluorescence microscopy images of patchy alumina ring particles (a) dried on substrate and (b) slightly aggregated in solution.

6.7 Reference

1. Ntziachristos, V.; Schellenberger, E. A.; Ripoll, J.; Yessayan, D.; Graves, E.; Bogdanov, A.; Josephson, L.; Weissleder, R. *Proceedings of the National Academy of Sciences of the United States of America* **2004,** 101, (33), 12294-12299.
2. Couvreur, P.; Vauthier, C. *Pharmaceutical Research* **2006,** 23, (7), 1417-1450.
3. Panyam, J.; Labhasetwar, V. *Advanced Drug Delivery Reviews* **2003,** 55, (3), 329-347.
4. Soppimath, K. S.; Aminabhavi, T. M.; Kulkarni, A. R.; Rudzinski, W. E. *Journal of Controlled Release* **2001,** 70, (1-2), 1-20.
5. Gratton, S. E. A.; Ropp, P. A.; Pohlhaus, P. D.; Luft, J. C.; Madden, V. J.; Napier, M. E.; DeSimone, J. M. *Proceedings of the National Academy of Sciences of the United States of America* **2008,** 105, (33), 11613-11618.
6. Mitragotri, S.; Lahann, J. *Nature Materials* **2009,** 8, (1), 15-23.
7. Champion, J. A.; Mitragotri, S. *Proceedings of the National Academy of Sciences of the United States of America* **2006,** 103, (13), 4930-4934.
8. Mishra, A.; Gordon, V. D.; Yang, L. H.; Coridan, R.; Wong, G. C. L. *Angewandte Chemie-International Edition* **2008,** 47, (16), 2986-2989.
9. Yang, L. H.; Gordon, V. D.; Trinkle, D. R.; Schmidt, N. W.; Davis, M. A.; DeVries, C.; Som, A.; Cronan, J. E.; Tew, G. N.; Wong, G. C. L. *Proceedings of the National Academy of Sciences of the United States of America* **2008,** 105, (52), 20595-20600.
10. Nehl, C. L.; Liao, H. W.; Hafner, J. H. *Nano Letters* **2006,** 6, (4), 683-688.
11. McLellan, J. M.; Li, Z. Y.; Siekkinen, A. R.; Xia, Y. N. *Nano Letters* **2007,** 7, (4), 1013-1017.

CHAPTER 7
CONCLUSION AND FUTURE WORK

Some of the work presented in this chapter is through collaboration with Dr. Peng Wan from Wuhan University, Wuhan China and Dr. Zhentin Dai from Professor William P. King's group in Mechanical Engineering Department.

Combining colloidal template and top down fabrication techniques such as deposition and etching, a variety of structures have been realized as discussed in previous chapters. Some of the structures show interesting optical properties. Some might find their usage in biology. In this chapter, a few interesting attempts will be mentioned and future work along those directions might be fruitful.

7.1 Patterned 3D Metallic Porous Structure

In chapter 2, the fabrication and optical properties of 3D various filling fraction metallic opals are discussed in details. And these fabrication techniques are compatible with typical 2D patterning on substrates. Two different approaches have been tried. In the first approach (Fig 7.1), colloidal crystal is first formed on a conductive substrate by either evaporation deposition or spin coating. Following that, traditional photolithography generates pattern on the film with positive tone photoresist protecting the colloidal crystal in desired regions and leave colloids in other regions exposed, which will be then etched by HF solution. The remaining photoresist goes through another round of photo exposure and is removed by solvent. The final result is that some regions on a conductive substrate are covered with colloidal crystal, the rest not. Metal such as copper would then be electrodeposited into the structure. The colloidal crystals can either be left in or removed. The resulting structures have attracted attention as micro scale electrical fuses (Fig. 7.2). The electrical properties of these structures needs further study.

In the second approach (Fig. 7.3), the conductive substrate is first patterned. Then colloidal crystal is grown on the whole structure followed by electrodeposition. After removing the colloidal template, the final result is 3D porous structure exists only in regions pre-patterned with metal. With this approach, AFM cantilever like 3D porous nickel structures have been prepared (Fig. 7.4). AFM cantilevers like that can be used to study the mechanical property of porous structures. Given the fact that it's relatively easy to generate layered structure using electroplating by this approach, AFM cantilever made of porous gold/nickel bilayer has been made (Fig. 7.5). And the porosity of the two layers is independently tunable. Devices like that have unique thermal mechanical properties with tunable mechanical response. They can function as actuators and sensors. Detailed studies are needed along this direction.

There is one more interesting electrical application for highly porous nickel inverse opal. Varistors are a kind of circuitry protection device which will become conductive under high voltage and remain insulating under low voltage. These devices are commonly used to bypass static charges and protect sensitive electronic systems. One popular way to make them is to use a network of metal/dielectric composite. This can be viewed as a network of back to back Schottkey diode which is only turned on at break down voltages. This network can be formed by percolating nickel particles with surface oxide. However, as electrical devices become increasingly miniaturized, the varistors need to shrink in size as well. That raised the demand for very good control over uniformity of the network and the number of metal/dielectric/metal junctions. The porous nickel structure meets these requirements very well: the 3D interconnected network is highly regular and uniform; the thin interconnects between the thick parts in an inverse opal can be thermally oxidized to form the semiconducting oxide. Oxidation of those nickel structures has been studied by in situ opal measurements at elevated temperature under atmosphere (Fig 7.6). As oxidation progresses, the optical features resulted from the porous metal structure fades away. The drop in reflectivity at long wavelength indicates an increasing penetration of light into the structure. That is also a sign of disconnecting of metallic elements. SEM images of the nickel structure after oxidation clearly show altered surface morphology. By controlling the oxidation condition, a network of metal/oxide/metal junctions can be achieved. The electrical testing of such devices needs further investigation.

Many findings with colloidal crystal templates can be easily transferred to holographic generated structures. Some difficulties associated with the nature of colloidal crystals such as cracks and defects can all be avoided.

7.2 Ring Particle Based Structures

So far discussed in chapter 5, all the ring particles generated are rigid. And people in the field of biological sciences are really interested in getting flexible ring particles with the same kind of geometry, especially, if the particles can be made out of functional molecules such as drug conjugated polymers [1]. Commercial polydimethylsiloxane (PDMS) are generated by reacting water with dichlorodimethylsilane [2]. The resulting chain polymer is viscoelastic in nature. Methyltrichlorosilane can be added to produce cross-linked PDMS which maintains its shape. Reacting silicon tetrachloride with water has been a popular approach for porous SiO_2 chemical vapor deposition (CVD) at room temperature. In such CVD process, two precursors are alternatingly introduced into the reaction chamber. Water first physisorbs onto the reaction surface and forms a thin water layer. Then when silicon tetrachloride is introduced, it reacts with the condensed thin water layer to form SiO_2. CVD of PDMS has been achieved before [3]. However, the reaction requires carefully designed equipment. If in SiO_2 CVD process, silicon tetrachloride is replaced with precursors that contain methyl group, similar reaction results PDMS layer. The possible issue is that PDMS is a lot less hydrophilic than typical CVD substrate surfaces such as oxides. As a result, the CVD layer, instead of forming a continuous film, might phase separate into hydrophobic islands. As one can imagine, more methyltrichlorosilane will lead to higher hydrophilicity and lower flexibility. A sweet spot might exist there. The PDMS rings can be slowly etched in HF solution. So PDMS ring particles should be able to form when proper template is chosen.

Combining PDMS and metallic CVD, followed by two step selective etching, patchy ring particles can be formed (Fig. 7.7). First a thin layer of tungsten is coated in silica sphere template by CVD followed by coating a thin layer of PDMS. Then, sample is slowly etched in HF solution until the tungsten layer under PDMS is exposed. The tungsten layer is then etched by electrochemical etching. Finally silica template is removed by HF and leaves ring particles with PDMS rim (hydrophobic) and tungsten (hydrophilic) sides. Similar approach can be applied to alumina/PDMS rings or PDMS/alumina rings, depending on the requirements.

The conformal growth followed by etching approach has one common problem so far. That is coating and etching usually involves harsh conditions, such as high temperature or strong acid. For some biological application, fairly fragile molecules are involved such as DNAs and proteins. These molecules can be decorated onto ring particles after particle synthesis. The approach obviously increases complexity. One inspiration comes from reference [4], in which during drying process, molecules are trapped at the contact point between colloidal particles. Following this approach, silica colloids and organic drug molecules can be co-deposited and then the template be etched. The drug molecules will stay in the ring shape assuming they are not soluble in water with low concentration of HF.

7.3 Ring Particle and Spherical Particle Co-Assembly

Ring particles, with their unique geometry form “lock and key” pair with spherical particles. So, if rings and spheres with opposite charge are mixed together, they will form a cross-linked network. Following that line of thinking, the relative size of spheres and ring particles can be adjusted. When the diameter of the rings D is larger than $\sqrt{3}$ times that of the spheres d ($D > \sqrt{3}d$), only 2 rings can attach to one sphere. When $\sqrt{3}d > D > \sqrt{2}d$, 3 rings can stay on one spherical particle. With ring particles smaller than that, 4, 5, 6 and more rings can stay on a single sphere. So, by controlling the size and the relative population of each kind of particle, chain cluster (linear polymer) of rings and spherical particles with appropriate length (degree of polymerization) can be formed. Adding a few larger spherical particles allows the formation of branch polymers or even cross-linked polymer. Tungsten ring particles has a negative surface charge, amine terminated spherical polystyrene particles have positive surface charge. These particles are hundreds of nanometer to micrometers in diameter and can be easily resolved under optical microscope in transmission/dark field/fluorescent modes. The resulting structure might help people understand some problems in polymer physical chemistry or at least visualize the dynamics of polymer systems.

7.4 Figures

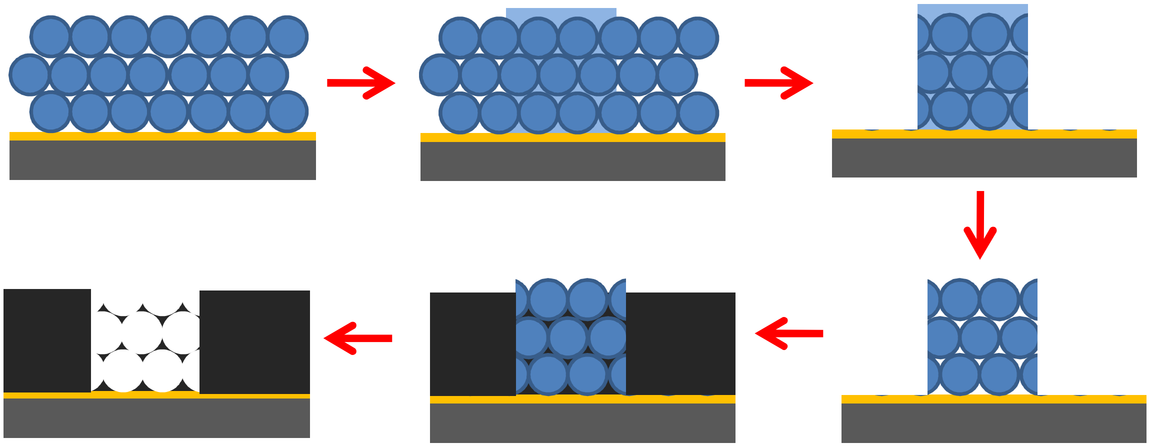

Figure 7.1 First approach of making patterned porous metal film. (See text for details.)

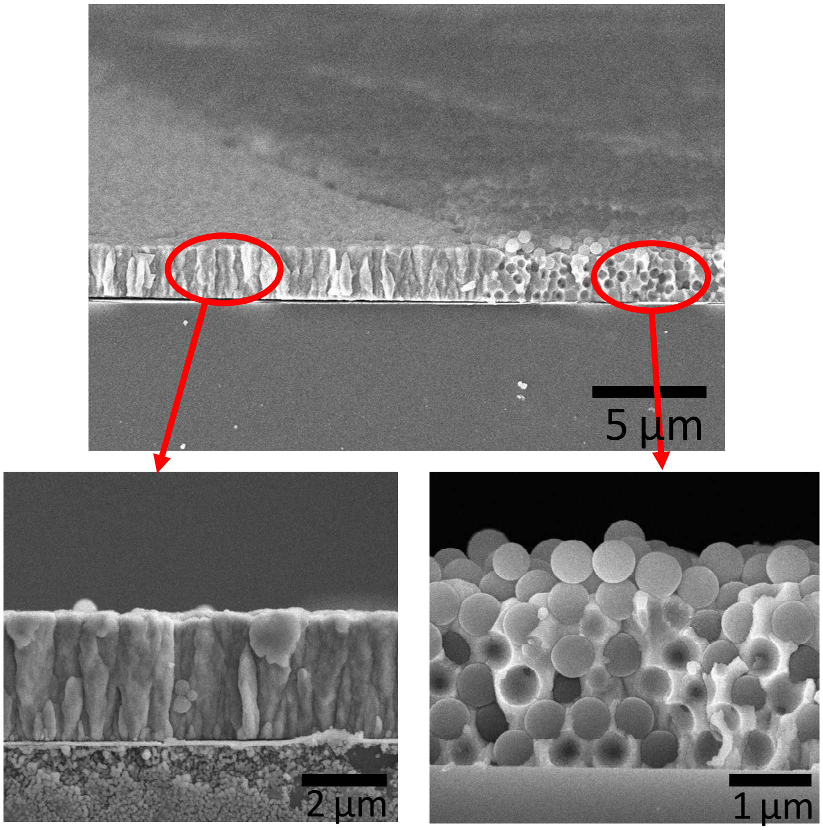

Figure 7.2 Cross-section SEM image of a pattern copper inverse opal at the boundary of porous and solid metal regions.

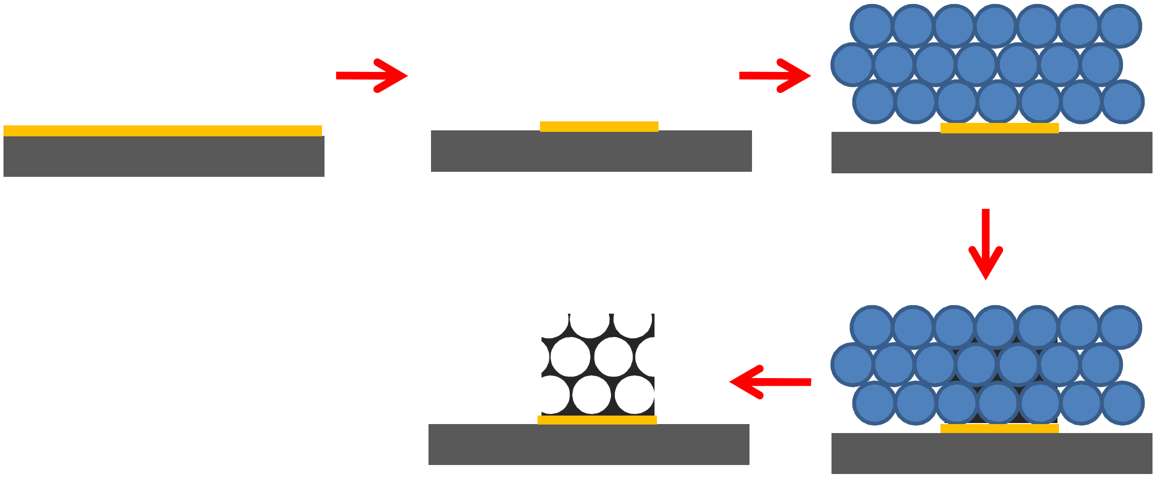

Figure 7.3 The second approach for making patterned porous metal structures. (See text for details.)

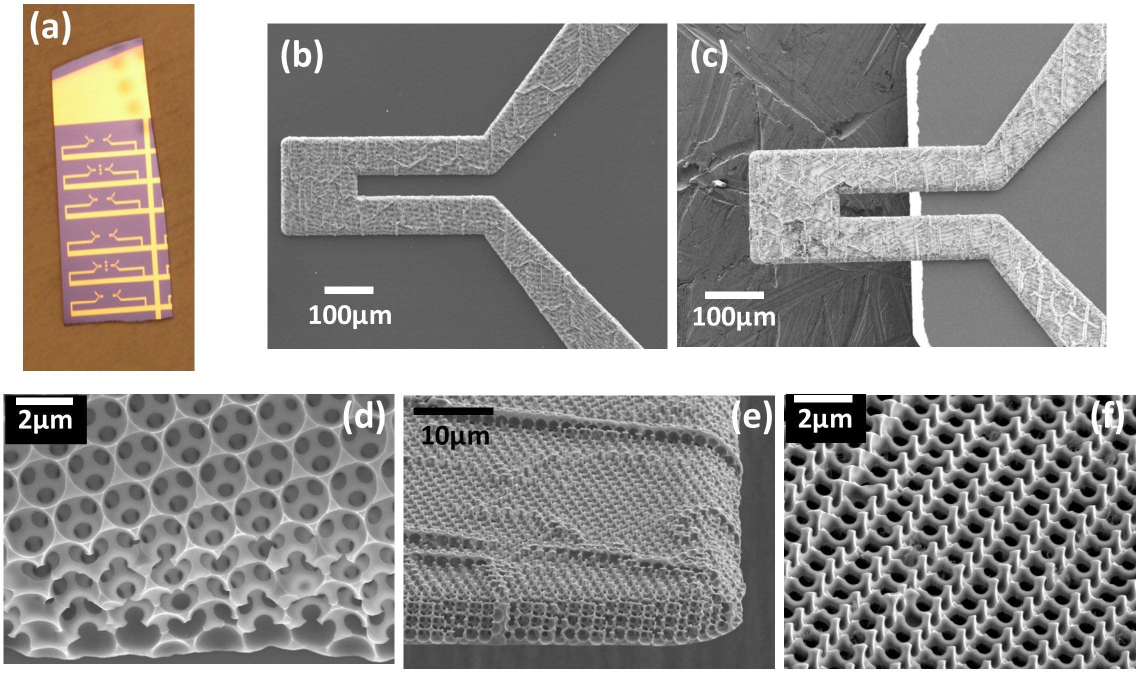

Figure 7.4 Porous nickel AFM cantilever pattern generated by the second approach of forming patterned porous structure. (a) Optical image of the substrate with patterned gold film. (b,c) Porous Ni AFM cantilever before and after release. (d) Top view SEM (e,f) tilted SEM of the cantilever.

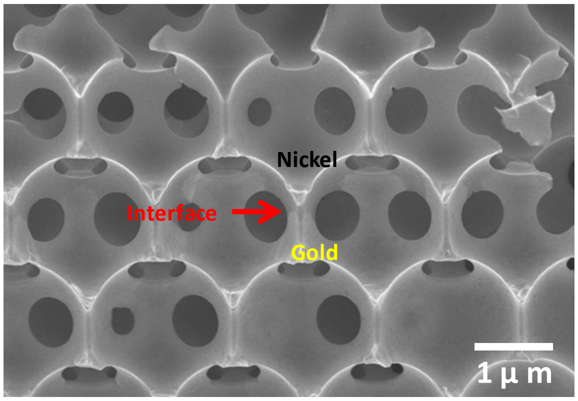

Figure 7.5 Gold/Nickel bilayer fabricated by electroplating of two metals in sequence. A clear interface can be seen.

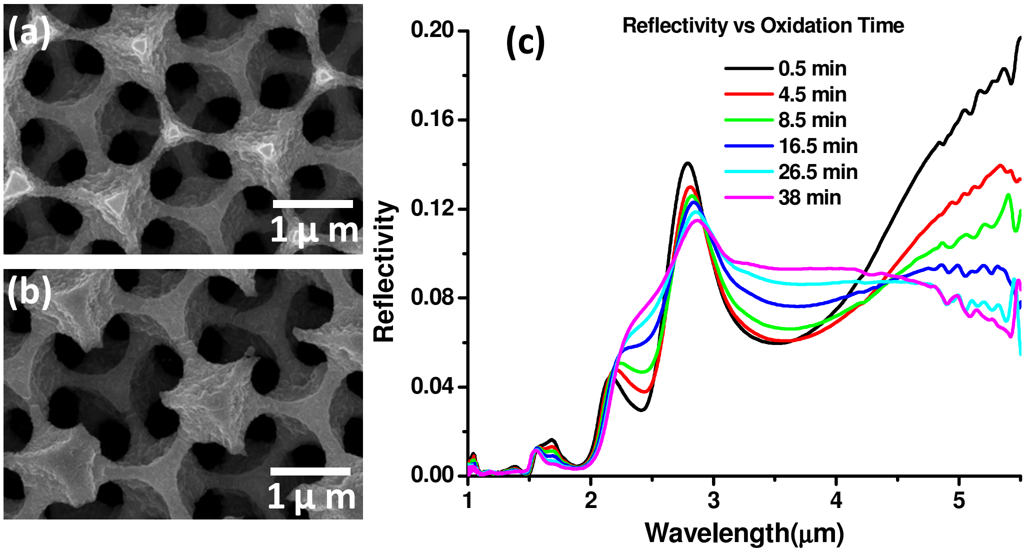

Figure 7.6 (a) and (b) SEM Image of a highly porous nickel inverse opal after thermal oxidation at 300°C for 50mins. (c) Reflective spectrum of the same nickel inverse opal sample as thermal oxidation takes place. The sample is held at 300°C under atmosphere and reflective spectra are taken at different time as oxidation progresses.

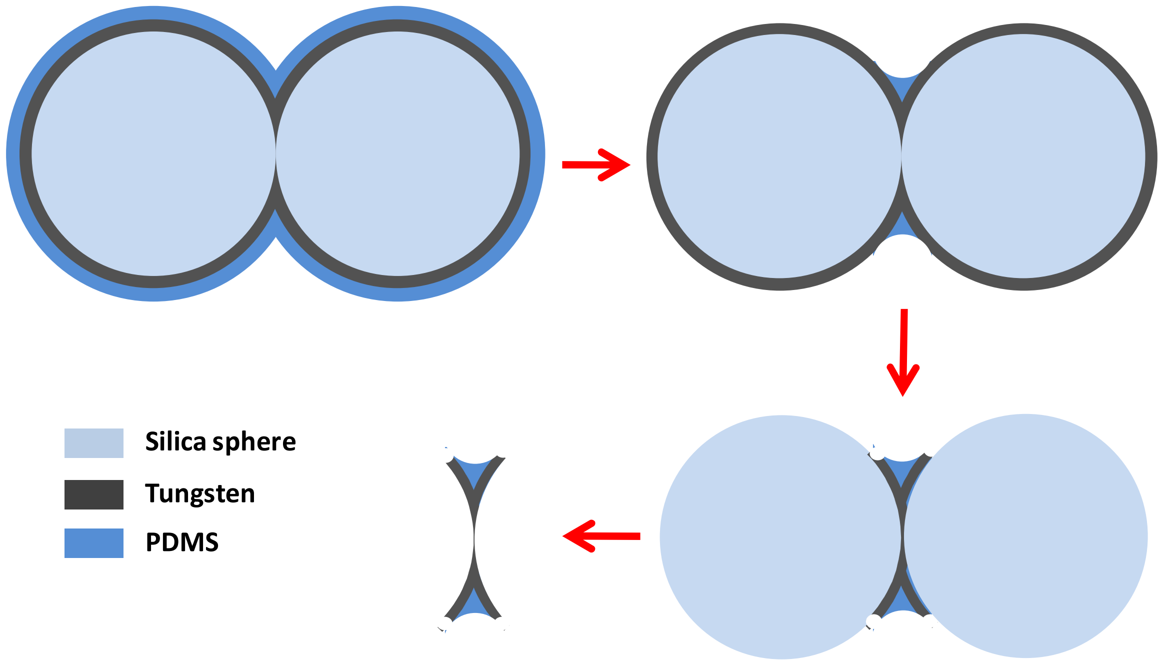

Figure 7.7 Schematics of making patchy ring particles by sequential CVD of tungsten and PDMS followed by slow HF etching and electrochemical etching. See text for details.

7.5 Reference

1. Tong, R.; Cheng, J. J. Angewandte Chemie-International Edition 2008, 47, (26), 4830-4834.
2. Huber, P.; Kaiser, W. Journal of Synthetic Lubrication 1986, 3, (2), 105-120.
3. Lewis, H. G. P.; Casserly, T. B.; Gleason, K. K. Journal of the Electrochemical Society 2001, 148, (12), F212-F220.
4. Yan, F.; Goedel, W. A. Angewandte Chemie-International Edition 2005, 44, (14), 2084-2088.

AUTHOR'S BIOGRAPHY

Xindi Yu was born in Shanghai, China in 1981. He graduated in 2003 from Fudan University in Shanghai with his Bachelor Degree in Science, major in Physics. Then he moved on to the University of Michigan at Ann Arbor and graduated in 2004 with a Master Degree in Science. Since then, he joined the PhD program in the Material Science and Engineering Department at University of Illinois at Urbana Champaign under the instruction of Professor Paul Braun. During the five and half years at Illinois, Xindi's research focused on fabrication and characterization of functional nanostructures. Xindi graduated from the University of Illinois in 2010 with PhD degree and went on to join Core R&D Department of Dow Chemical Company at Midland, Michigan.